ON THE DEVELOPMENT OF MACROSCALE MODELING STRATEGIES FOR AC/DC TRANSPORT-DEFORMATION COUPLING IN SELF-SENSING PIEZORESISTIVE MATERIALS

A Dissertation

Submitted to the Faculty

of

Purdue University

by

Goon Mo Koo

In Partial Fulfillment of the

Requirements for the Degree

of

Doctor of Philosophy

December 2020

Purdue University

West Lafayette, Indiana

THE PURDUE UNIVERSITY GRADUATE SCHOOL
STATEMENT OF DISSERTATION APPROVAL

Dr. Tyler N. Tallman, Chair

School of Aeronautics and Astronautics

Dr. R. Byron Pipes

School of Aeronautics and Astronautics

Dr. Arun Prakash

School of Civil Engineering

Dr. Vikas Tomar

School of Aeronautics and Astronautics

Dr. Wenbin Yu

School of Aeronautics and Astronautics

Approved by:

Dr. Gregory A. Blaisdell

Head of the School Graduate Program

For my wife & daughter

ACKNOWLEDGMENTS

First and foremost, I am deeply grateful to my advisor, Professor Tyler N. Tallman for his support, guidance, and encouragement for my graduate studies in the school of Aeronautics and Astronautics at Purdue University. He enlightened me the way to become a professional researcher. I am truly honored to work with such an outstanding advisor and blessed to be one of his first graduate students.

I would feel grateful to my inspiring committee members, Dr. R. Byron Pipes, Dr. Arun Prakash, Dr. Vikas Tomar, and Dr. Wenbin Yu for showing their enlightening conversations, critical comments, and inspiring advice on my thesis dissertation.

I want to thank Dr. Christopher Gilpin in the department of the Purdue Life Sciences for his help in obtaining the scanning electron microscope (SEM) images to validate microstructure of my test specimens. Thank you, Dr. Gilpin.

I would also express my gratitude to Dr. R. Byron Pipes for allowing me to use lab equipments and learn equipment setup at IMI.

Thank you to my lovely lab mates, Julio A. Hernandez and Hashim Hassan for their daily conversation, help and advice. They encouraged and helped me when I felt emotional and academic difficulties. I would not come to this point if they are not my colleagues. I truly feel blessed to have Julio A. Hernandez and Hashim Hassan.

Lastly, I would like to thank my wife and daughter for supporting and encouraging me. I would not have finished this work without their love and help. Thank Hae Young and Dana for giving me indescribable happiness.

TABLE OF CONTENTS

Page

Page

LIST OF TABLES

LIST OF FIGURES

Figure Page

Figure Page

Figure Page

Figure Page

Figure Page

ABBREVIATIONS

CB	Carbon Black
CNF	Carbon Nanofiber
CNT	Carbone Nanotube
EIS	Electrical Impedance Spectroscopy
EIT	Electrical Impedance Tomography
ERT	Electrical Resistance Tomography
FRC	Fiber Reinforced Composites
GF	Glass Fiber
LVDT	Linear Variable Differential Transformer
MWCNT	Multi-Walled Carbon Nanotube
PDMS	Polydimethylsiloxane
PE	Polyelectrolyte
PMMA	Polymethyl Methacrylate
PS	Polystyrene
RVE	Representative Volume Element
SWCNT	Single-Walled Carbon Nanotube
SEM	Scanning Electron Microscope

ABSTRACT

Koo, Goon Mo Ph.D., Purdue University, December 2020. On the Development of Macroscale Modeling Strategies for AC/DC Transport-Deformation Coupling in Self-Sensing Piezoresistive Materials. Major Professor: Dr. Tyler N. Tallman.

Sensing of mechanical state is critical in diverse fields including biomedical implants, intelligent robotics, consumer technology interfaces, and integrated structural health monitoring among many others. Recently, materials that are *self-sensing* via the piezoresistive effect (i.e. having deformation-dependent electrical conductivity) have received much attention due to their potential to enable intrinsic, material-level strain sensing with lesser dependence on external/ad hoc sensor arrays. In order to effectively use piezoresistive materials for strain-sensing, however, it is necessary to understand the deformation-resistivity change relationship. To that end, many studies have been conducted to model the piezoresistive effect, particularly in nanocomposites which have been modified with high aspect-ratio carbonaceous fillers such as carbon nanotubes or carbon nanofibers. However, prevailing piezoresistivity models have important limitations such as being limited to microscales and therefore being computationally prohibitive for macroscale analyses, considering only simple deformations, and having limited accuracy. These are important issues because small errors or delays due to these challenges can substantially mitigate the effectiveness of strain-sensing via piezoresistivity. Therefore, the first objective of this thesis is to develop a conceptual framework for a piezoresistive tensorial relation that is amenable to arbitrary deformation, macroscale analyses, and a wide range of piezoresistive material systems. This was achieved by postulating a general higher-order resistivity-strain relation and fitting the general model to experimental data for carbon nanofiber-modified epoxy (as a representative piezoresistive material with

non-linear resistivity-strain relations) through the determination of piezoresistive constants. Lastly, the proposed relation was validated experimentally against discrete resistance changes collected over a complex shape and spatially distributed resistivity changes imaged via electrical impedance tomography (EIT) with very good correspondence. Because of the generality of the proposed higher-order tensorial relation, it can be applied to a wide variety of material systems (e.g. piezoresistive polymers, cementitious, and ceramic composites) thereby lending significant potential for broader impacts to this work.

Despite the expansive body of work on direct current (DC) transport, DC-based methods have important limitations which can be overcome via alternating current (AC)-based self-sensing. Unfortunately, comparatively little work has been done on AC transport-deformation modeling in self-sensing materials. Therefore, the second objective of this thesis is to establish a conceptual framework for the macroscale modeling of AC conductivity-strain coupling in piezoresistive materials. For this, the universal dielectric response (UDR) as described by Joncsher's power law for AC conductivity was fit to AC conductivity versus strain data for CNF/epoxy (again serving as a representative self-sensing material). It was found that this power law does indeed accurately describe deformation-dependent AC conductivity and power-law fitting constants are non-linear in both normal and shear strain. Curiously, a piezoresistive switching behavior was also observed during this testing. That is, positive piezoresistivity (i.e. decreasing AC conductivity with increasing tensile strain) was observed at low frequencies and negative piezoresistivity (i.e. increasing AC conductivity with increasing tensile strain) was observed at high frequencies. Consequently, there exists a point of zero piezoresistivity (i.e. frequency at which AC conductivity does not change with deformation) between these behaviors. Via microscale computational modeling, it was discovered that changing inter-filler tunneling resistance acting in parallel with inter-filler capacitance is the physical mechanism of this switching behavior.

1. LITERATURE REVIEW

1.1 Introduction

Strain-sensing is critical to a wide range of technological areas such as robotics, civil and energy infrastructures, aerospace structures, and biomedical engineering in order to keep these structures operating safely, reliably, and in their intended fashion. As a representative example of the importance of strain sensing in a structural application, an airport parking garage at Eindhoven catastrophically failed in 2017 as shown in Figure 1.1 [1]. Later analyses showed that the primary reason for this collapse was that the interfacial shear strength between the precast concrete floor slabs was insufficient. This led to eventual failure. It could be argued that continuously monitoring the strain of this interface could have allowed for repairs to be made before the failure event. As another example, energy infrastructures such as wind turbines are routinely exposed to severe operational loads and therefore require frequent maintenance and rigorous safety measurements [2]. However, due to their height, these maintenance operations are expensive and potentially dangerous to human inspectors. In another example, robots must be able to 'sense' their environment (e.g. grip strength, collisions, etc.) to operate safely (particularly with regard to human interactions). Therefore, intrinsic strain sensing capabilities (e.g. via artificial or 'e-skin' which mimics human skin) can substantially improve the safe operation of robotics. And as a final representative example to motivate the importance of strain sensing, revision surgeries to total joint replacements represent a significant financial burden to the US healthcare system (revision surgeries cost over $8 billion annually in the US) [3]. Cemented implants in which the implant stem is bonded to compact bone via a 'bone cement' – often poly(methyl methacrylate) or PMMA – are commonly used in these procedures. However, the early precursors of failure such

as aseptic loosening (i.e. loss of fixation between the implant and the PMMA) are invisible on traditional imaging modalities such as radiographs until late-stage failure. At this point, non-surgical options are very limited because the interface failure has progressed too far. Monitoring strains via changes in load transfer across the PMMA as a precursor of aseptic loosening could therefore provide important clinical information on the onset of implant failure. In light of the preceding discussion, it can be concluded that there exists a pervasive and high-impact need to know the strain state of in-service structures and components.

Fig. 1.1. The Eindhoven parking garage collapse in 2017 [1].

There are various existing technologies to meet these needs. Strain-sensing approaches can be generally categorized into two ways – i) discrete sensing and ii) full-field imaging. First, discrete sensing approaches disperse point-based strain sensors over the surface of a component or embedded in the component (e.g. within a fiber-reinforced composite [4]). Representative examples of embedded sensors are linear variable differential transformers (LVDT) [5–8], fiber optics [9–12], and tradi-

tional foil-based strain gages [13–16]. These modalities are very briefly summarized below.

- LVDT is an electromechanical sensor that outputs electrical data corresponding to the applied displacements. It is composed of a primary core, two secondary cores, and a rod producing magnetic flux thereby manifesting as a change in voltage output. It is typically utilized in rough environmental conditions such as a bridge exposed to the environment.

- Fiber-optic sensors make use of light inside of optical fiber to find displacements. A common type of fiber-optic sensor is fiber-bragg gratings (FBG). Changes in grating length due to applied displacement affect the refractive index thereby producing wavelength-specific micromirror in the fiber that acts as an indicator of displacements. Fiber optic sensors guarantee high-resolution and accuracy of strain measurements over incredibly long ranges, but they are expensive and fragile.

- A traditional strain gage is a device that measures strain by changing electrical resistance as a consequence of deformation changing the geometry of the sensor. These are generally used as part of a Wheatstone bridge.

These discrete strain sensing elements have the benefit of generally being relatively cost-effective (with the exception of fiber optics) and being easily installed. However, these sensing elements cannot monitor the entire structure due to their discrete nature unless an extensive network of sensors is used. Furthermore, the possibility of stress concentrations exists when these sensors are embedded in a component or structure. Some applications may even outright preclude these sensors being embedded. For example, traditional strain gauges cannot be installed into biomedical implants such as joint replacements because wires cannot be made to penetrate through the patient in a manner that safe and sterile.

Considering the second common form of strain measurements, some full-field imaging approaches have recently gained much interests due to their ease of application and

potential for integration with the so-called fourth industrial revolution by making use of machine learning and image processing. Full-field imaging approaches can be used to localize damages [17–23] and identify surface deformation by analyzing images of the surfaces of structures. Representative full-field strain-sensing approaches include digital image correlation (DIC) [24–28], holographic interferometry (HI) [29–32], and shearography [33–36]. These are briefly described below.

- DIC tracks the in-plane deformation by comparing images in deformed state to reference image taken before deformation. DIC is able to accurately measure two-dimensional displacements, but three-dimensional methods which utilize multiple cameras (i.e. stereo DIC) have recently gained traction. Therefore, utilizing DIC technique can have great benefits in visualizing full-field displacements and strains compared to discrete sensors.

- HI is a interferometry method of using holographic photography. The interferometer using a common optical path creates beam separation by two different exposures and measures the deformations through the difference between the two beams – the reference beam and object beam. HI has considerable advantages over discrete sensors. For example, it is a real-time three-dimensional imaging technology, no sensors need to be installed onto the structure, and it is precise and sensitive to small deformations for complex structures. However, in order to achieve beam separation, a complicated experimental setup is required including multiple divergence lenses and mirrors.

- Shearography is a speckle pattern shearing interferometry similar to HI. It captures consecutive images to identify strains. In contrast to HI which measures displacements and converts to strain, shearography directly measures derivatives of displacement (i.e. strain). Shearography was developed in order to overcome some limitations of HI. For example, it does not require complicated setup because it does not need a reference beam. Additionally, it is less sensitive to ambient vibrations and has a wider range of sensitivity compared to HI.

Despite the great advantages of full-field strain imaging, these methods have a few limitations. First, the hardware can be expensive (this is less applicable to DIC). Second, they cannot visualize sub-surface or internal strains. Third, the hardware for HI and shearography can be very sensitive to external effects and experimental setup. And fourth, these methods are often not practical for in-the-field deployment and are therefore limited to laboratory settings.

1.2 Self-Sensing Materials

As an alternative to the preceding strain-sensing modalities, self-sensing materials have received much attention. The materials are attractive for strain-sensing because they overcome many of the preceding limitations associated with traditional strain-sensing modalities. In this approach, *the material is the sensor* thereby eliminating the need to build-in sensors and naturally allowing for full-field sensing. A common approach to self-sensing is via the *piezoresistive effect*. This refers to a material having deformation-dependent electrical conductivity. Piezoresistivity is achieved by modifying a non-conductive matrix with a conductive filler phase. Beyond a critical concentration of conductive fillers, the material system becomes conductive. This is referred to as the percolation threshold. Deformations that alter the connectedness of this network manifest as conductivity changes. Generally, compressive deformations will force more fillers to be in contact thereby increasing the conductivity whereas tensile deformations will cause fillers to become further apart thereby decreasing the number of fillers in contact and reducing the conductivity of the composite. This is graphically illustrated in Figure 1.2.

The range of piezoresistive materials is vast – this has been studied in structural polymers [37–39], soft polymers [40–43], cementitous materials [44–47], and ceramics [48–50]. Further, for materials which cannot be directly modified by a conductive filler (e.g. metals), 'sensing skins' (i.e. thin films modified by a conductive filler phase) have been explored [51–53]. Electrical percolation is also closely tied to aspect

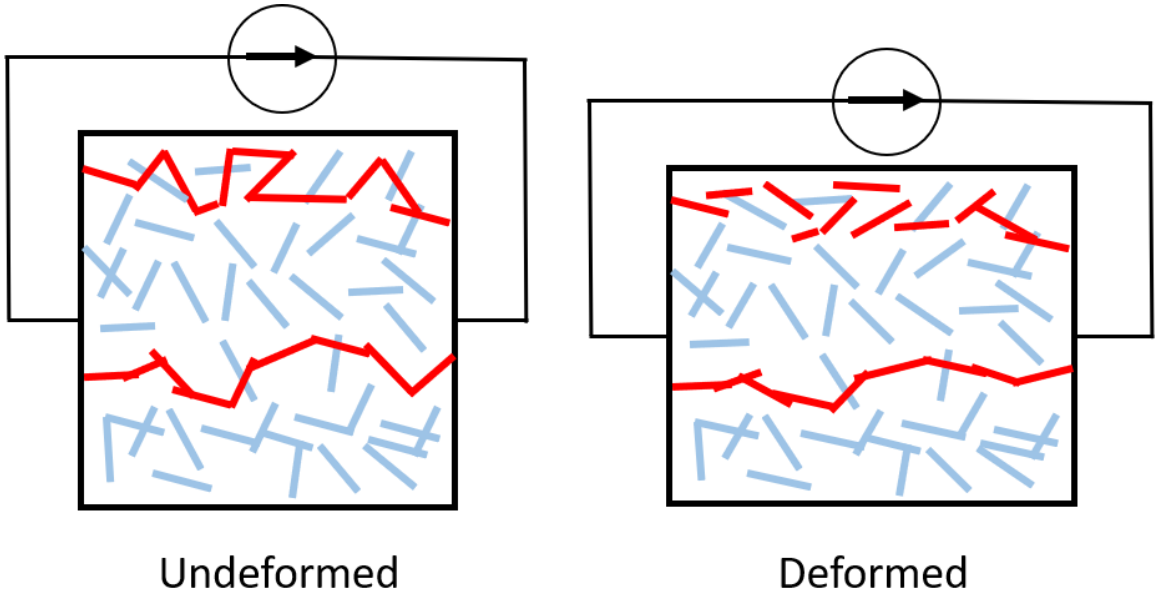

Fig. 1.2. Depiction of nanofiller network in the piezoresistive nanocomposites. Resistivity changes due to applied deformation. Conductive path as shown in red is disconnected due to deformation. Left: undeformed state of nanofiller network. Right: deformed state of nanofiller network which increase the resistivity due to disconnection in conductivity path.

ratio; fillers that are very long and thin percolate at much lower concentrations than other filler shapes. Because of this, carbon nanotubes (CNTs) have received much attention as a filler material [37, 38, 54, 55]. A representative MWCNT network is shown in Figure 1.3. Other common fillers for piezoresistive materials include silver particles [56–59], carbon black (CB) [60–63], graphene nanoplatelets (GNPs) [64–67], and carbon nanofibers (CNFs) [68–71]. More economical (i.e. much lower cost than, for example, CNTs) choices such as fly ash [72, 73] and metallic waste powder [74] have also been studied.

As a few recent representative examples of the diverse applications in self-sensing materials, Sun *et al.* [76] developed flexible tactile sensors to detect three-dimensional force with double-sided rough porous structure of CNTs/polydimethylsiloxane (PDMS)

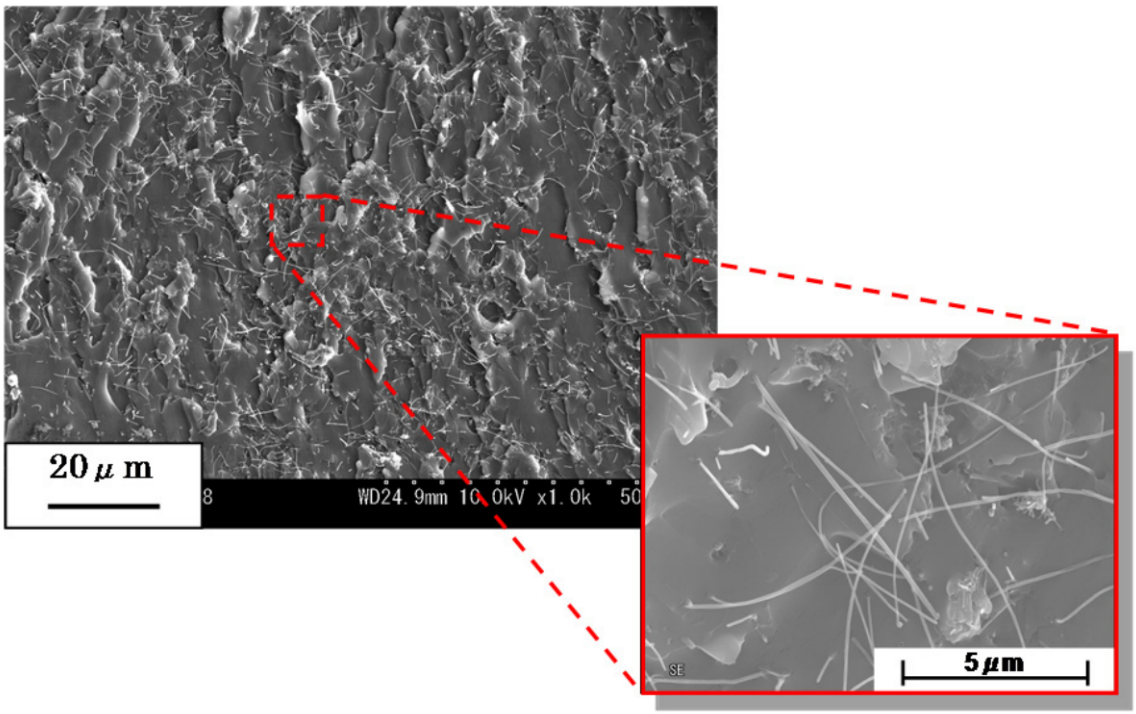

Fig. 1.3. Representative example of nanocomposites (2.0 wt.% MWCNT/epoxy) imaged via scanning electron microscope (SEM). Left: Far-out view of MWCNT/epoxy nanocomposites. Right: Enlarged view. White stick-shaped lines indicate MWCNTs [75].

shown in Figure 1.4(a). They obtained high sensitivity with low cost manufacturing, repeatability, stability, and uniformity. Furthermore, they were able to detect wrist pulse (Figure 1.4(b)) and finger movements (Figure 1.4(c)), and eventually sensors were integrated with robotic arms in such a way that it can grip items in real time. Next, Loh *et al.* [77] manufactured sensing skins using a CNT-modified polymer. Specifically, a layer-by-layer thin film fabrication process was used to build up the sensing layer on a metallic substrate as shown in Figure 1.5. Also, they used electrical impedance tomography (EIT) to spatially localize impact-induced conductivity changes. Additionally, Gao *et al.* [78] built a fiber-reinforced ceramic matrix composite plate. Here, carbon fibers make up a 2.5D woven structure using a stack of

woven textiles. Then, via the piezoresistive effect, damage is detected and localized via electrical resistance tomography (ERT) as shown in Figure 1.6. Furthermore, Gupta *et al.* [79] produced a self-sensing cementitious material. A MWCNT thin film was deposited onto fine aggregates of the cement. Holes in the composite materials were again detected and localized via EIT as shown in Figure 1.7. And as a final representative example, Ghaednia *et al.* [3] modified PMMA bone cement with short-chopped carbon fiber. This was then used to cement a total joint replacement in a surrogate geometry. Load transfer was able to be tracked across the cement interface via EIT in a phantom tank as shown in Figure 1.8.

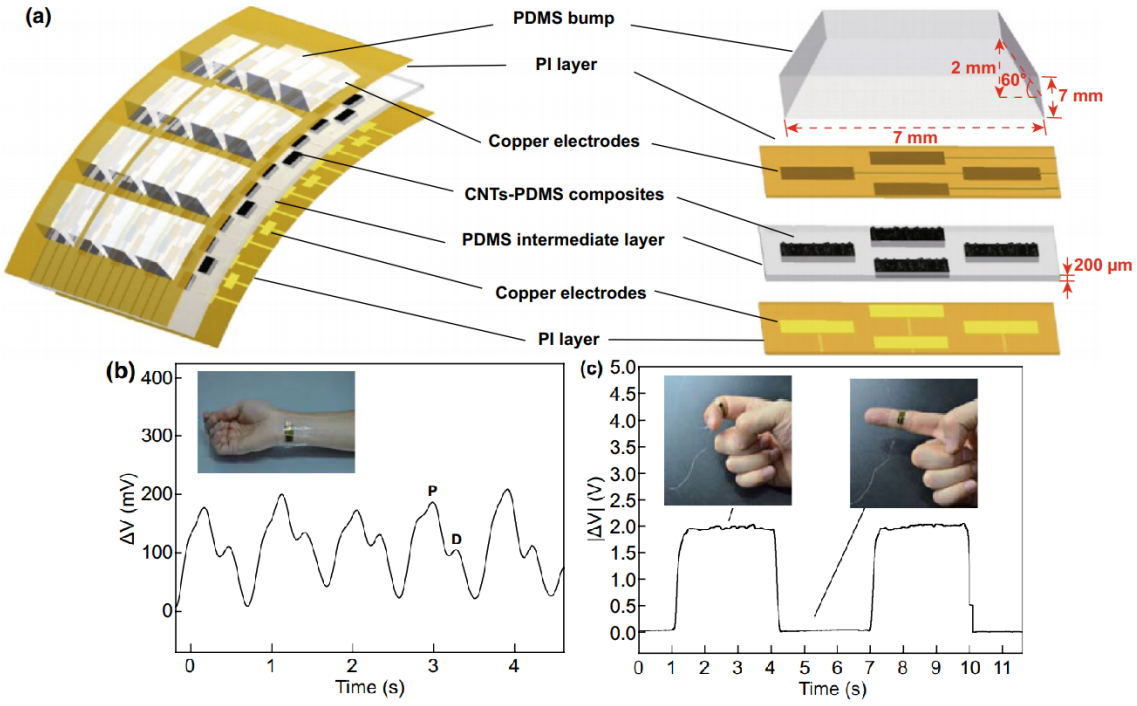

Fig. 1.4. (a) Schematic drawing of the tactile sensor array and one single element. (b) Detection of wrist pulses. (c) Detection of finger bending [76].

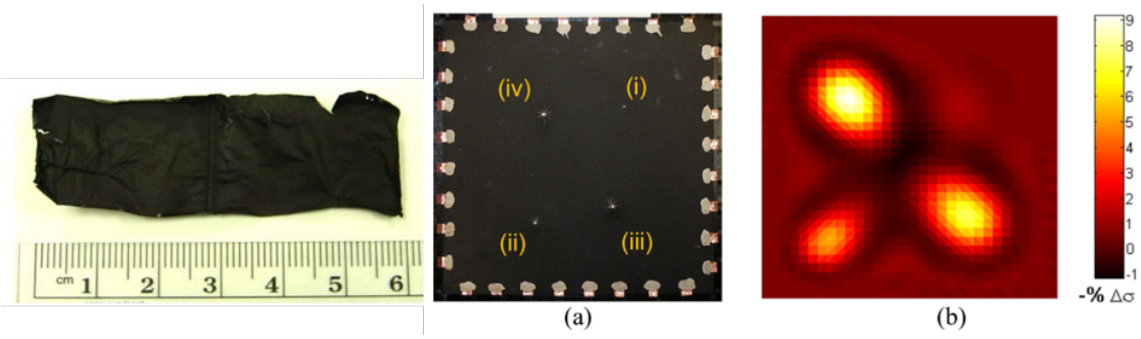

Fig. 1.5. Left: CNT-modified polymer self-sensing skin. Middle: impact damage in a metal plate coated with the sensing skin due to four different energy levels. Right: impact damage detected and localized via EIT [77].

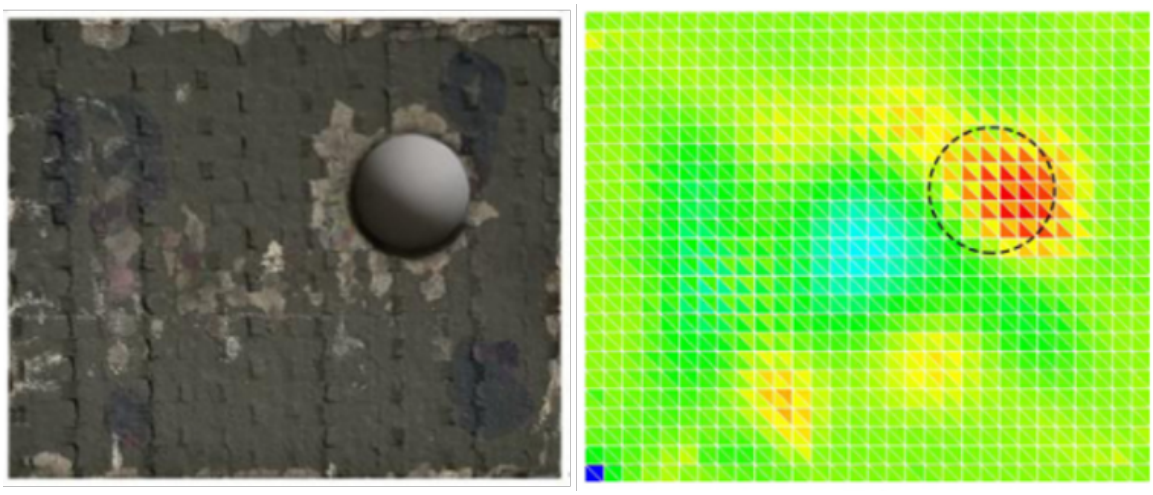

Fig. 1.6. Hole detection via ERT in 2.5D C/SiC composite plate [78]

1.3 Modeling the Piezoresistive Effect

The preceding discussion outlines the motivation to study self-sensing materials. However, to make meaningful predictions from these materials, methods of modeling the resistivity-strain relation are needed. That is, it is necessary to know what resistance or resistivity changes are expected for a given state of strain. Unfortu-

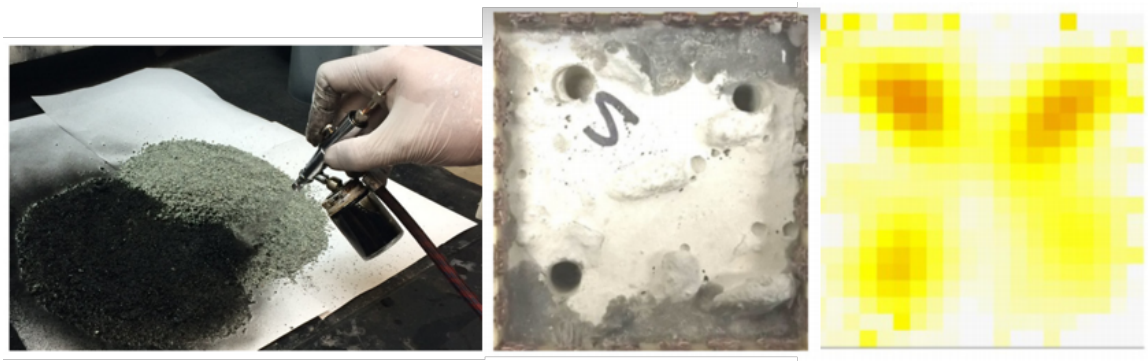

Fig. 1.7. Damage identification in MWCNT/cement composites. Left: MWCNT-latex ink is sprayed over the sand to formulate thin film. Middle: three holes were drilled at three corners. Right: the change in resistivity distribution as imaged via EIT [79]

nately, prevailing piezoresistivity models are inadequate in this regard. Further, the current state of the art focuses overwhelmingly on direct current (DC)-based self-sensing. However, alternating current (AC) methods have important advantages over DC-based methods. Below, these considerations are discussed.

1.3.1 DC-Based Piezoresistivity

In the current state of the art, piezoresistivity models can be generally classified into three types: i) equivalent resistor network models, ii) computational micromechanics-based models, and iii) analytical piezoresistivity models. Equivalent resistor network models [80–91] simulate individual conductive fillers and their electrical interactions within a microscale domain. These efforts have focused overwhelmingly on nanocomposites to-date. In these approaches, individual fillers and the junctions between interacting fillers are discretized into resistor elements as illustrated in Figure 1.9. Deformation is incorporated by calculating how the fillers rotate and translate due to some applied deformation [88]. The post-deformed network is then re-discretized and the net voltage-current relationship is again calculated. Due to

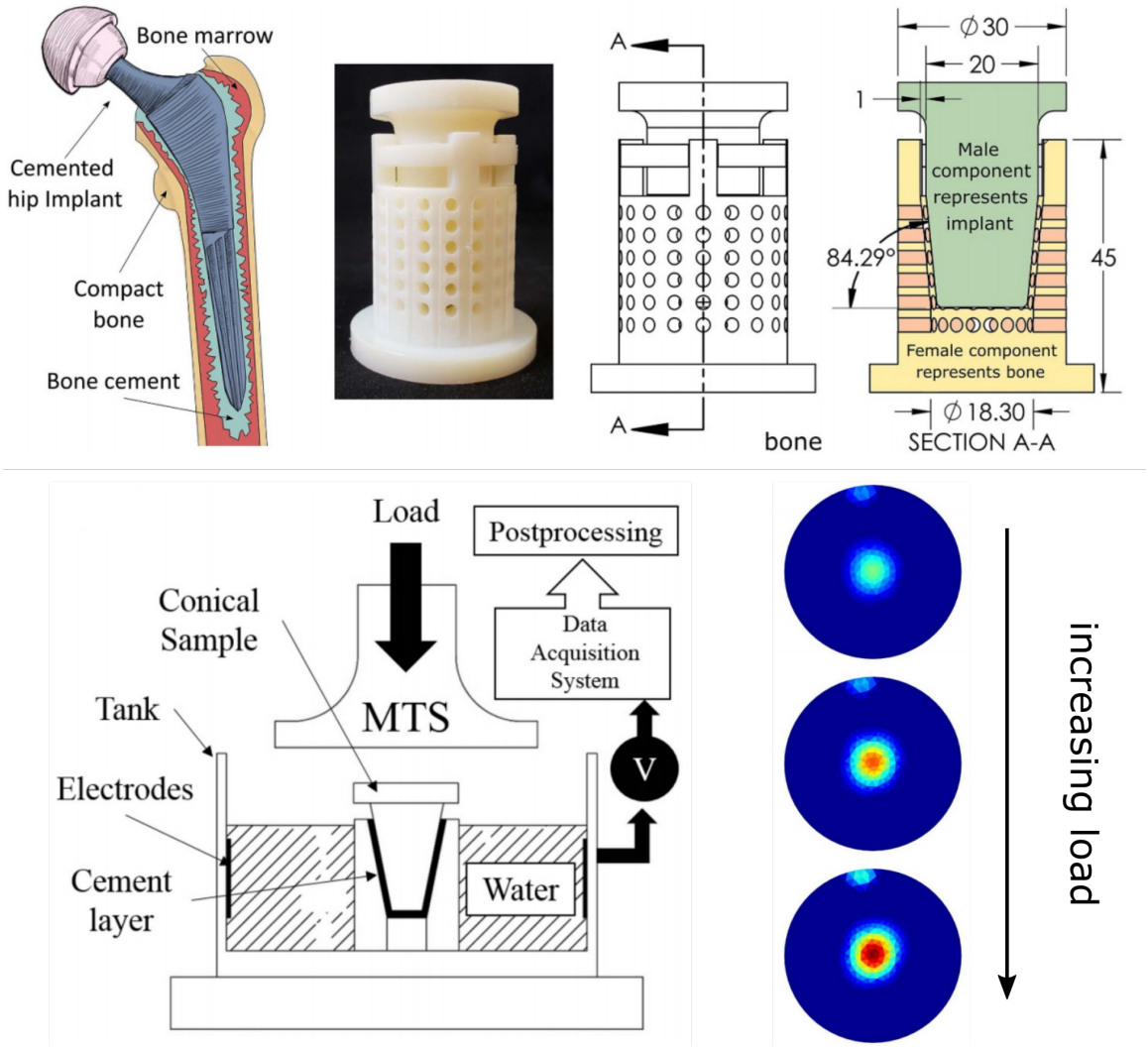

Fig. 1.8. Overview of work to monitor total joint replacement fixation via self-sensing PMMA. Top: Schematic of geometry – the surrogate geometry was designed to replicate the bone-to-implant interface. Bottom-left: Schematic of phantom tank. The surrogate is immersed in water (representing the leg) and compressed from above at physiological loading levels. Bottom-right: The change in conductivity of 1.5 vol.% specimen imaged by EIT. EIT clearly identifies increasing levels of loading (all within physiologically realistic ranges) [3].

simulating individual fillers, this type of models has the benefit of great control over details of the filler network such as extent of agglomeration and filler alignment.

However, there are few limitations. First, these approaches are computationally very expensive because an extreme number of fillers are needed to form a percolated network. In addition, these approaches consider only simple deformations and do not explicitly model the matrix material as shown in Figure 1.10. And lastly, equivalent resistor network models have limited accuracy. For example, Hu *et al.* [92] developed three-dimensional statistical models by incorporating the tunneling effect between adjacent nanofillers and a fiber reorientation model. They compared experimental results in resistance change ratio to numerical predictions derived from their equivalent resistor network model. Significant discrepancies between experimental and numerically simulated results existed for each weight fractions of CNT/polymer nanocomposites as shown in Figure 1.11.

Next, consider computational micromechanics models. In contrast to equivalent resistor network models, computational micromechanics-based models [94–99] consider both the nanofillers and the enveloping matrix simultaneously within a finite element framework. Consequently, micromechanics-based models are well-suited to simulate mechanical effects such as debonding between fillers and matrix material as shown in Figure 1.12. These approaches have revealed that the macroscale piezoresistive response in nanocomposites is majorly dependent on the nanoscale phenomenon of electron hopping, interface separation, and initiation/evolution of interface damage. Chaurasia *et al.* [96] compared the strain-induced effective conductivity changes of nanocomposites including interface separation/damage to that including perfectly bonded interface between fillers and matrix. Figure 1.13 is provided to visualize the effect of interface separation. They observed that the piezoresistive response from interface separation is larger than that from perfectly bonded interface as shown in Figure 1.14. However, because of the fact that they simulated individual nanofillers and the enveloping matrix material in a microscale representative volume element (RVE), they are not without limitations – these models are very computationally expensive and therefore difficult to scale. Furthermore, this type of model is limited

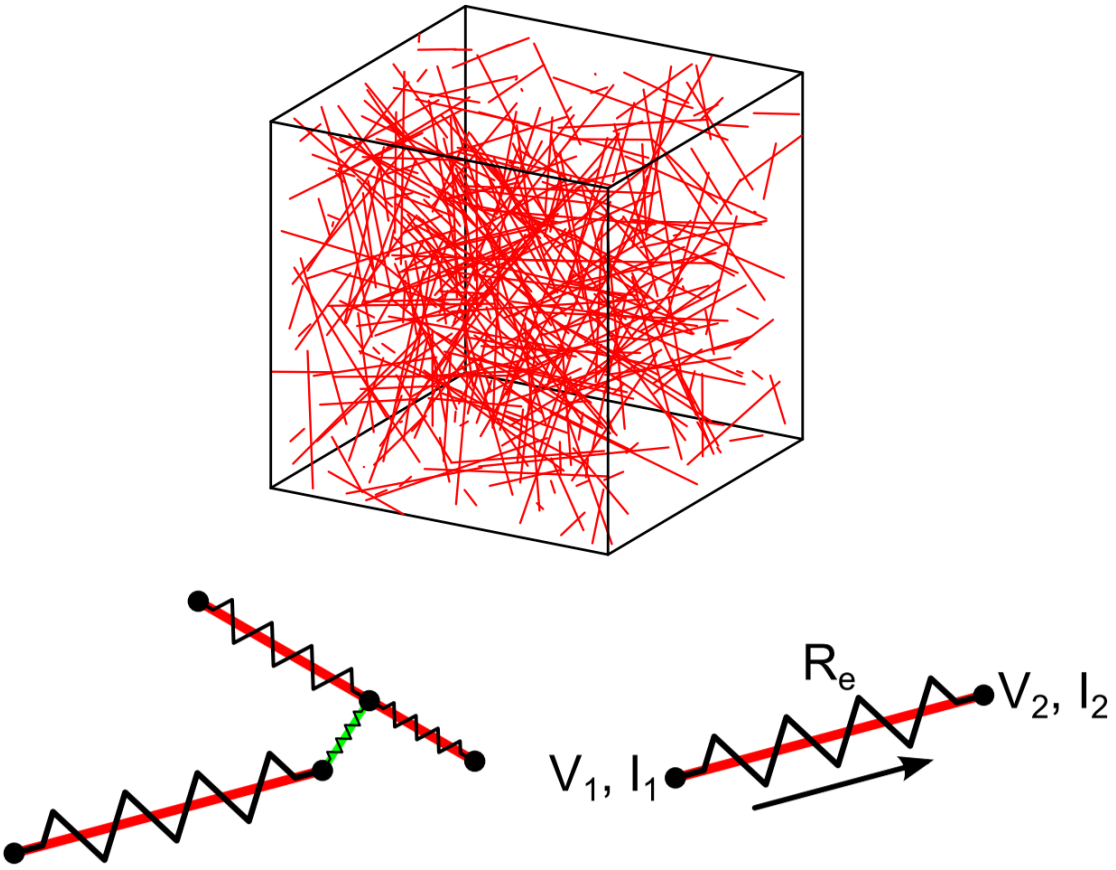

Fig. 1.9. Depiction of conductive paths. Top: randomly distributed conductive nanofillers in a microscale representative volume element (RVE) Bottom left: representative image of quantum tunneling as a resistor element (shown in green) between fillers. Bottom right: illustration of filler discretization into a resistor element. In this approach, electrical transport through the network is tracked in terms of nodal voltages and currents [93].

to nanofiller bundles (i.e. agglomerations) as shown in Figure 1.15 which indicates that it does not account for well-dispersed nanofillers.

Finally, analytical piezoresistivity models [100–104] use closed-form expressions to predict resistivity changes based on manufacturing parameters and strain. These approaches are not nearly as computationally burdensome as equivalent resistor network nor computational micromechanics-based models because individual nanofillers

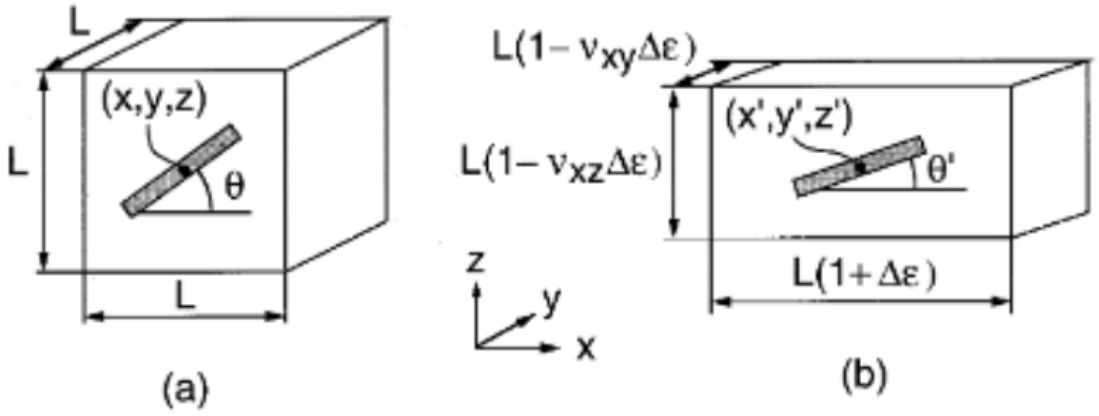

Fig. 1.10. The three-dimensional rigid short fiber reorientation model due to applied strain in x-direction. (a) before deformation. (b) after deformation [88].

are not simulated. Therefore, they are suitable to be implemented for structural-scale analyses. However, there also exist limitations for analytical models. Analytical models must make assumptions regarding average inter-filler distances, orientations of fillers, and other filler properties such as aspect ratio. For this, they need much information on microstructure of the system such as tunneling barrier height, filler dimensions, critical volume fraction, and percolation probability. Tallman and Wang [101] developed an analytical model for CNT composite piezoresistivity by identifying strain-dependent parameters in a conductivity model originally developed by Takeda *el al.* [105]. Conductivity changes were determined by predicting strain-induced changes to filler volume fraction, filler separation, and filler orientation. From this, their model predicted resistance changes that are reasonably well-matched with experimental results as shown in Figure 1.16. However, this model failed to capture the saturation effect in compression. Then, to demonstrate the potential of analytical models to make macroscale predictions, this approach was integrated with finite element methods in order to predict the conductivity change distribution of an I-beam subject to arbitrary deformation as shown in Figure 1.17. Other analyt-

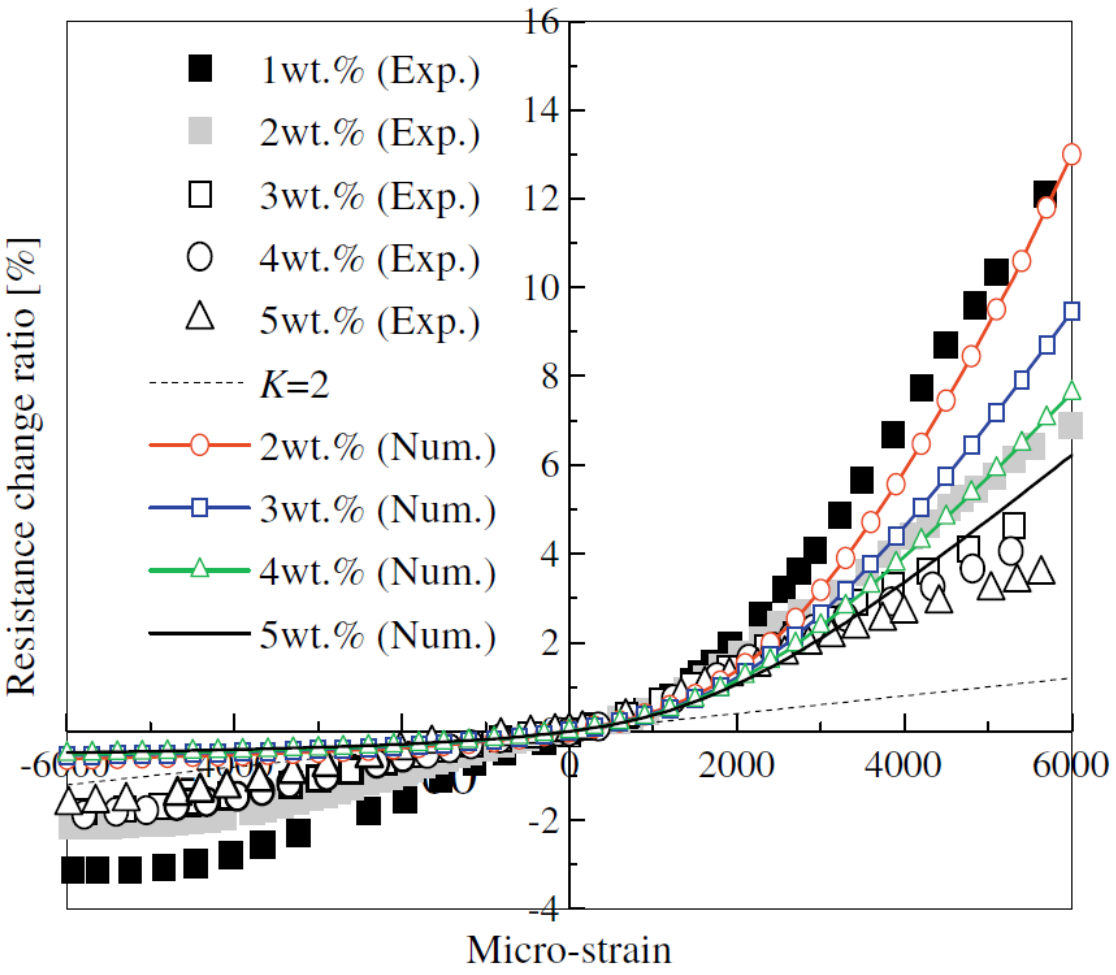

Fig. 1.11. Resistance change ratio with respect to different weight fractions of CNT/polymer nanocomposites as a function of applied strain. Comparison between numerical prediction and experimental data is presented. Relatively large discrepancies are shown for each weight fraction [92].

ical models generally require substantial training or calibration data. For example, Matos *et al.* [103] developed models of multiaxial strain-sensing by utilizing finite element methods in combination with machine learning. As shown in Figure 1.18, their machine learning-predicted resistance change versus applied strain shows good correspondence with other models. Further, they are able to predict stress concentration-

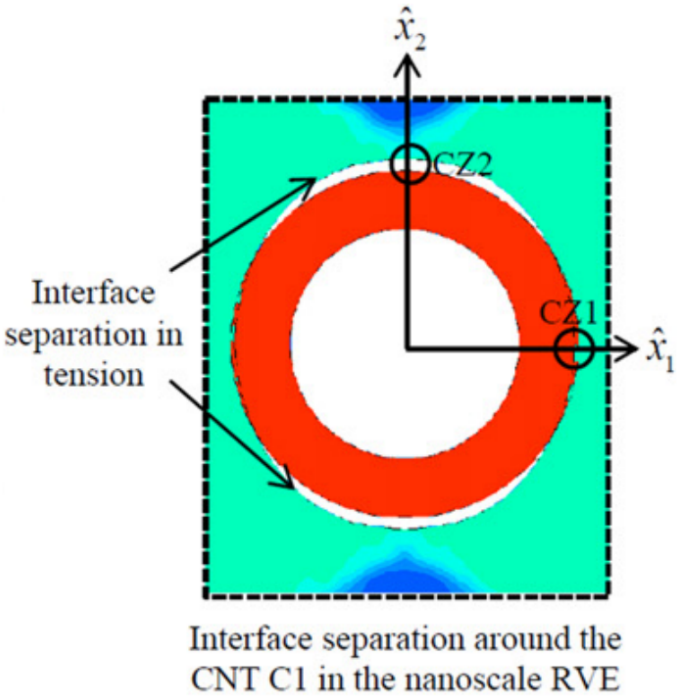

Fig. 1.12. Depiction of interface debonding between a nanofiller and a matrix in the nanoscale RVE [96].

induced conductivity changes in the vicinity of the hole in a plate specimen as shown in Figure 1.19. However, they trained and validated their machine learning approach to other model-generated data – experimental validation is needed for this approach.

To summarize the preceding discussion, prevailing piezoresistivity models have important limitations with regard to making meaningful predictions. That is, they are computationally prohibitive for structural-scale analyses, often of limited accuracy, limited to simple deformations, and/or require extensive knowledge of the material's microstructure, calibration, or training data.

1.3.2 AC-Based Piezoresistivity

To date, work in self-sensing materials has focused overwhelmingly on DC properties. Comparatively little has been done on AC-based methods and on the effect

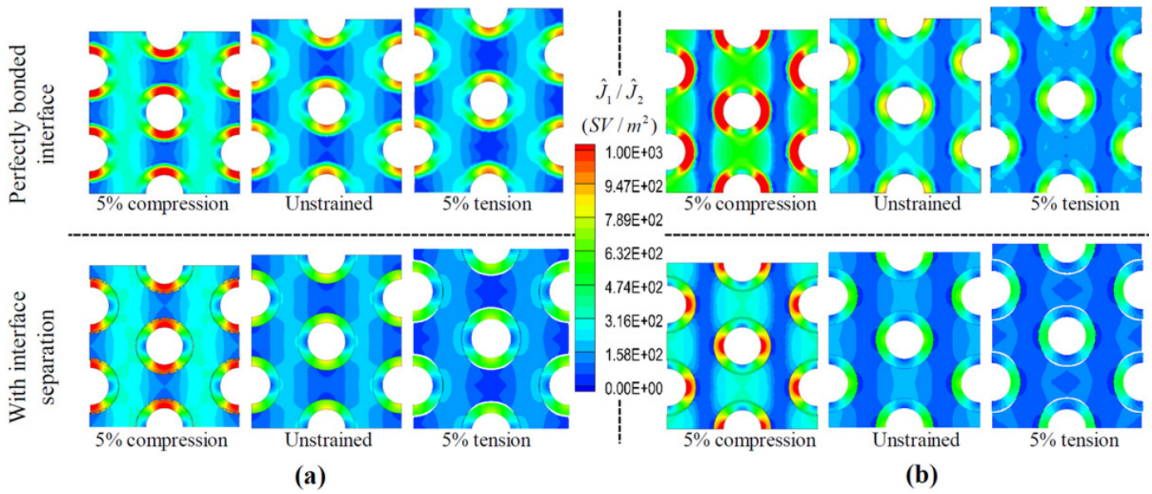

Fig. 1.13. Current density distribution with perfectly bonded interface and with interface separation. (a) Current density in the x_1-direction and (b) current density in the x_2-direction [96].

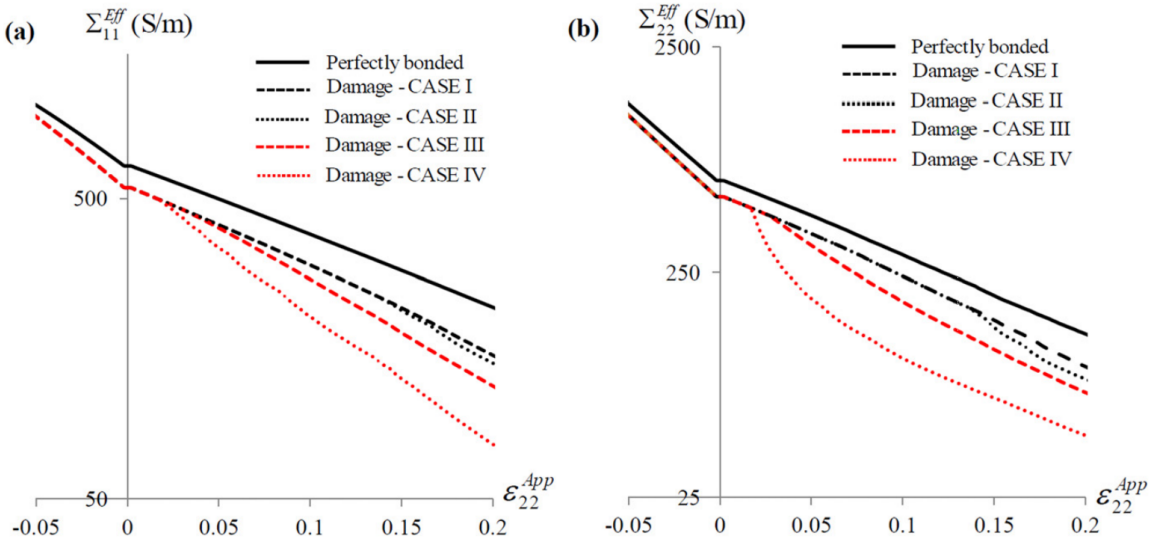

Fig. 1.14. Effective conductivity comparison between perfectly bonded interface and interface separation. (a) Effective conductivity in the x_1-direction and (b) effective conductivity in the x_2-direction [96].

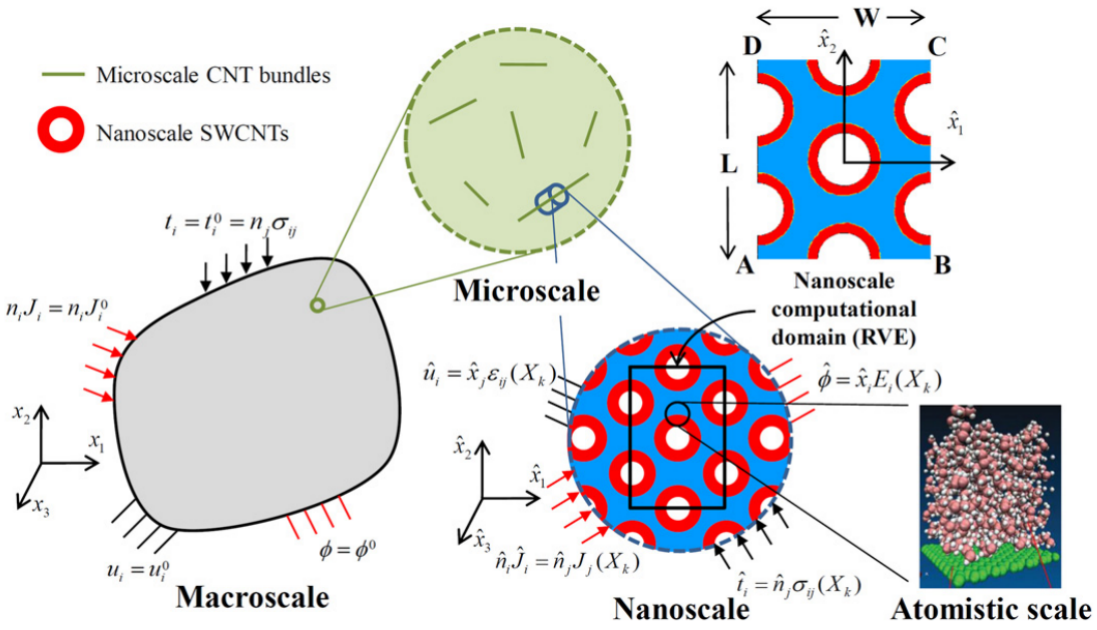

Fig. 1.15. Macroscale to atomistic scale depiction for computational micromechanics-based models. Note that they considers nanofiller bundles rather than well-dispersed nanofillers in multi-directions [96].

of deformation on AC transport. This is noteworthy because AC-based methods have considerable advantages over DC-based methods. First, AC inherently carries more information. That is, both impedance and phase angle data can be utilized to identify and characterize deformations when using AC instead of only resistance for DC-based methods. Second, AC methods have potential to increase sensitivity. For example, it has been experimentally shown that sensitivity to damage can be improved by inducing electrical resonance in a CNF/epoxy specimen by the inclusion of an external inductor [106]. And third, AC conductivity exponentially increases with interrogation frequency (e.g. Figure 1.20). Because piezoresistive materials generally have relatively low conductivity, high-frequency self-sensing can substantially lower power requirements for these materials [107, 108].

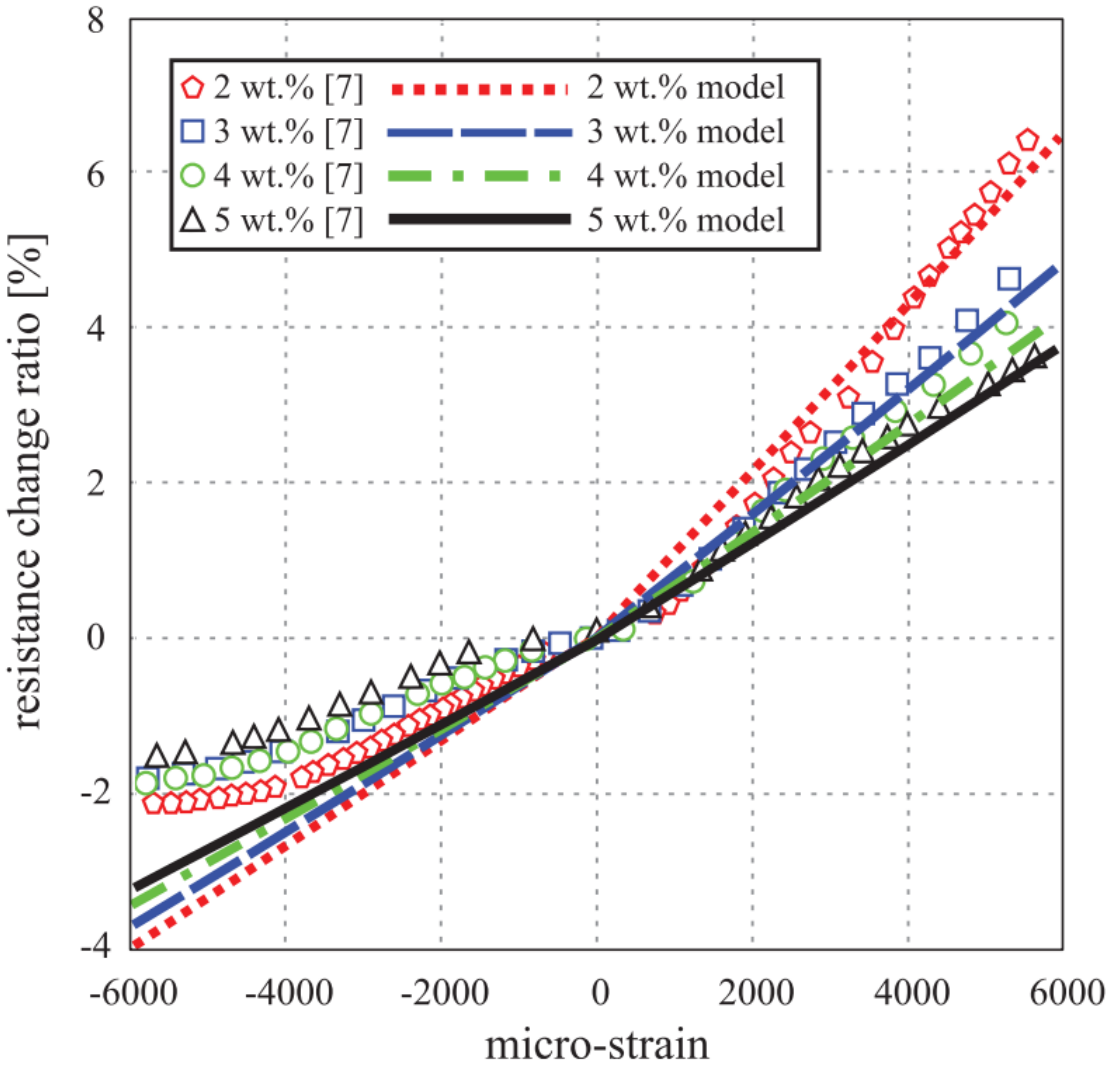

Fig. 1.16. Piezoresistive response predicted by the analytical model are compared to the experimental piezoresistive response. Note that the experimental data flattens or saturates in compression whereas the model fails to predict this [101].

Several representative studies on AC piezoresistivity in the state of the art are next summarized. Mohanraj *et al.* [109] investigated CB-modified styrene-butadiene rubber and reported that AC conductivity increased with compressive pressure. However, their investigation frequency range was limited up to 1 kHz. Wang *et al.* [110]

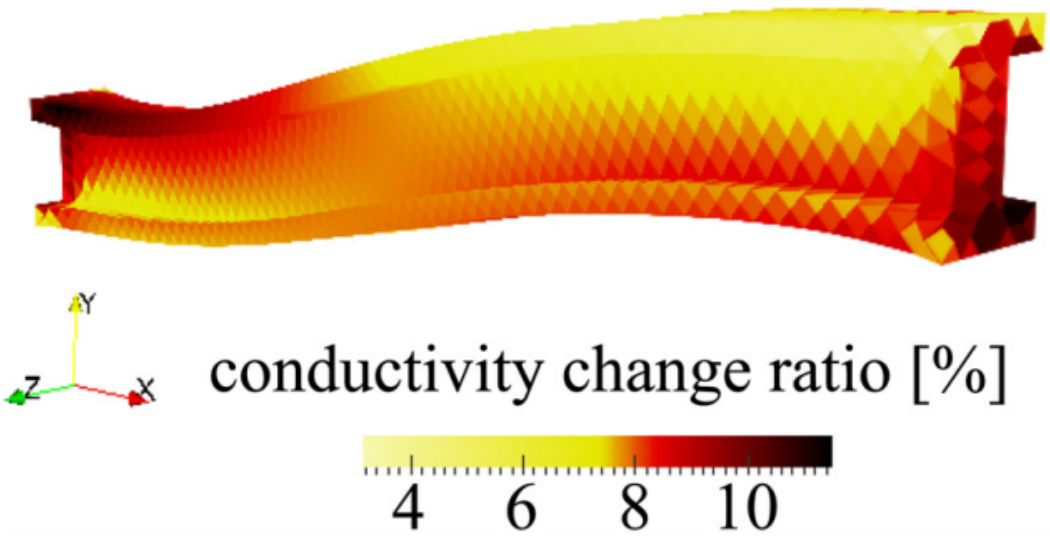

Fig. 1.17. Conductivity change ratio of 1 m length I-beam. Note that I-beam is fixed at one end and 5 mm displacement in x-, y-, and z-direction is applied at the other end [101].

showed that the sensitivity of AC conductivity in CB-modified silicone-rubber due to compressive pressure increases with increasing frequency up to 1 MHz. Loh *et al.* [111] manufactured single-walled (SW)CNT-modifed polyelectrolyte (PE) composite via a layer-by-layer thin film fabrication process and utilized an equivalent circuit model to fit experimental AC data up to 250 kHz as a function of strain. In order to better understand the relations between complex impedance and deformations, they conducted a parametric study for the relationship between each element of their proposed equivalent circuit and deformations as shown in Figure 1.21. Helseth [112] characterized electrical properties of MWCNT-modified polydimethylsiloxane with electrical impedance spectroscopy (EIS) in order to describe electromechanical behavior under compression. Impedance measurements were taken up to 1 MHz as a compressive force was applied from 0 to 50 N. It was observed that EIS curves indeed vary due to compression which can be replicated via equivalent circuit analyses as shown in Figure 1.22. Kang *et al.* [113] developed a CNT/PMMA composite sensor.

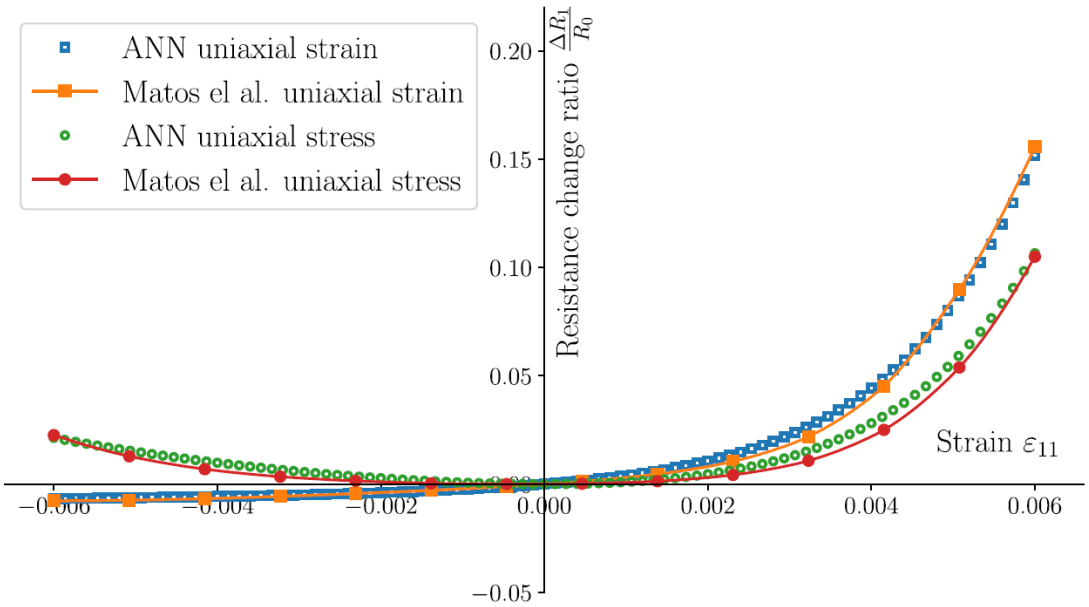

Fig. 1.18. Resistance change ratio as a function of applied strain. Comparison between finite element-based and machine learning-based prediction is presented [103].

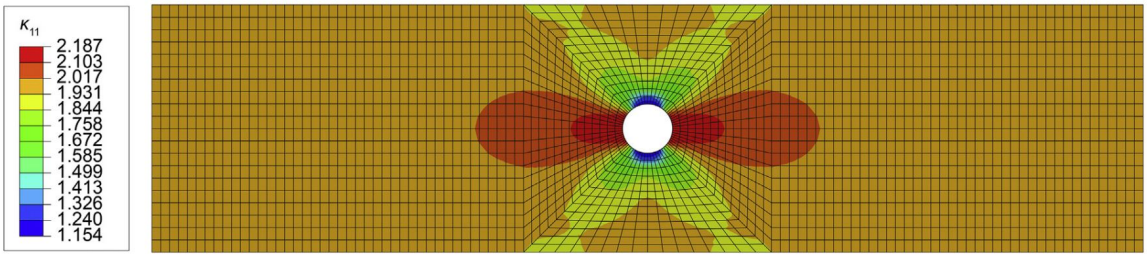

Fig. 1.19. Simulated axial conductivity distribution in a plate with a hole geometry subject to displacement of 0.006 of the total length [103].

They utilized an equivalent circuit model to understand the behavior of resistance and capacitance in equivalent circuit under static and dynamic loading. It was observed that capacitance has a negligible effect in dynamic testing.

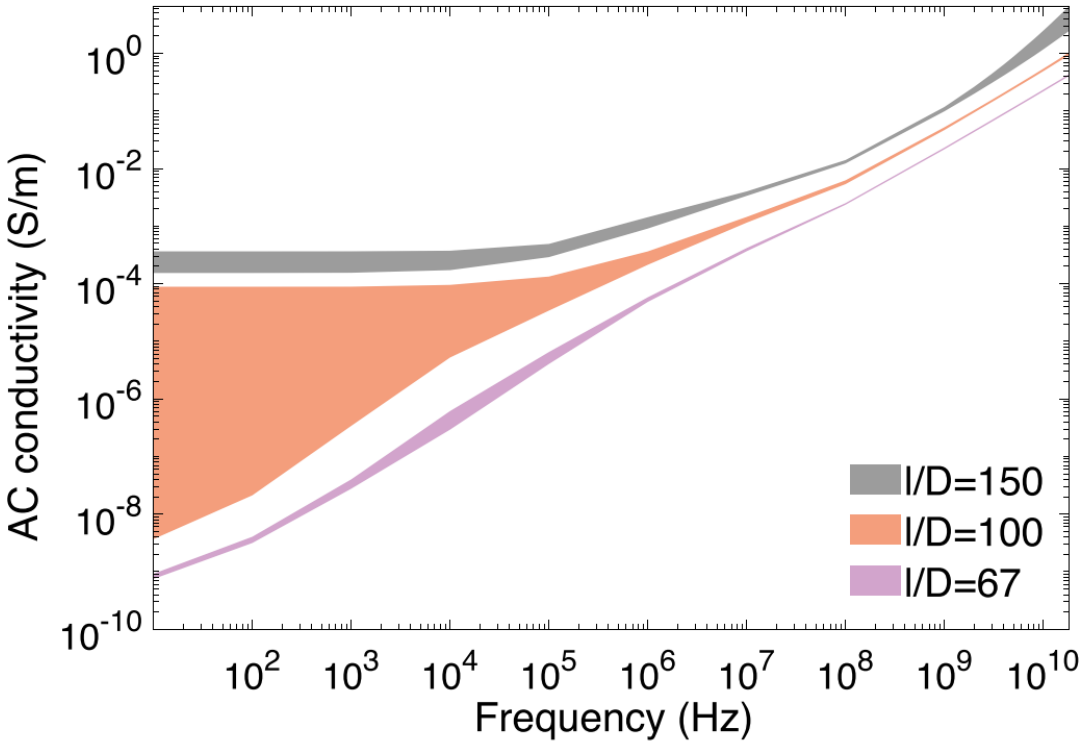

Fig. 1.20. AC conductivity with respect to interrogation frequency. l/D represents CNT aspect ratio. Note that conductivity exponentially increases at high frequencies [107].

It is also noteworthy that virtually no work exists for *material property* modeling with regard to AC piezoresistivity. That is, the three classes of models that exist for DC piezoresistivity – equivalent resistor networks, computational micromechanics-based models, and analytical models – are absent from AC studies. Rather, modeling work that exists for AC piezoresistivity is in terms of equivalent circuit analyses. This means that some circuit is proposed (generally constructed from linear elements – resistors, capacitors, and inductors – and sometimes Warburg elements) which is capable of replicating the net voltage-current response of the material. Circuit parameters are then expressed as a function of strain. But this approach is limiting because it is based on a discrete measurement rather than a material property. This

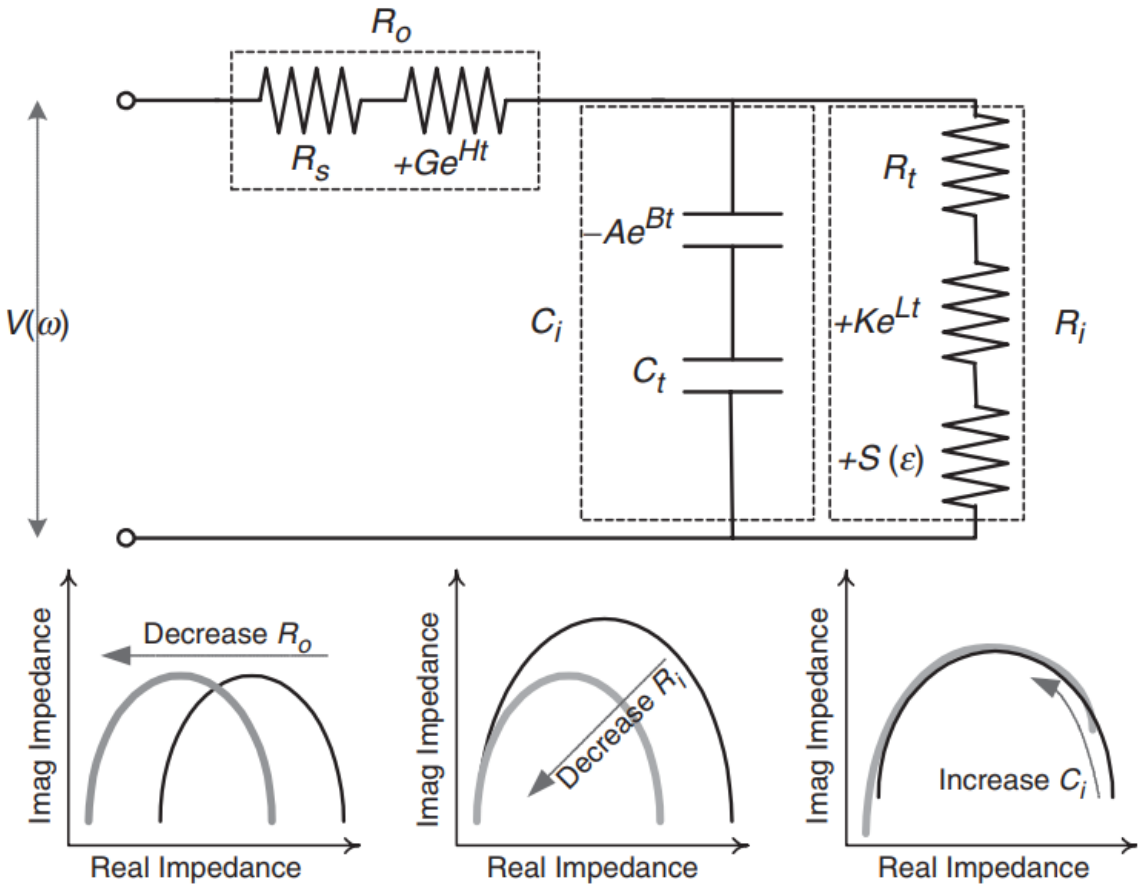

Fig. 1.21. Top: equivalent circuit representing complex impedance in a MWCNT sensing skin. Strain and time-dependent circuit parameters are included. Bottom: representation of how EIS curves vary with respect to changes in the equivalent circuit [111].

is akin to describing mechanical properties in terms of force-displacement relations rather than stress-strain relations. Therefore, in order to proliferate AC-based self-sensing, it is important to describe AC material properties as a function of strain.

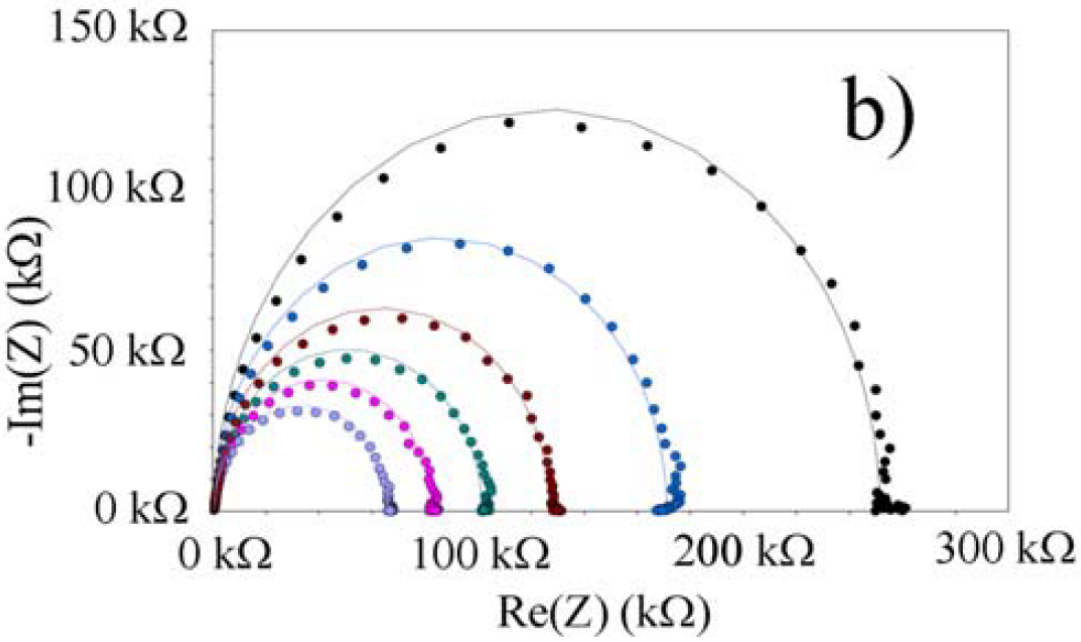

Fig. 1.22. The effect of compressive loading on EIS curves for MWCNT-modified PDMS (black: 2 N, blue: 5N, brown: 10 N, green: 15 N, pink: 20 N, and purple: 30 N) [112].

2. PROBLEM STATEMENTS, RESEARCH GOALS, THESIS CONTRIBUTIONS, AND THESIS ORGANIZATION

Chapter 1 establishes that a pervasive need for strain sensing exists in diverse and far-reaching applications. Materials which are intrinsically self-sensing via the piezoresistive effect have noteworthy advantages over traditional sensing modalities. Further, piezoresistive-based self-sensing has been explored in a wide range of material systems including polymers (hard and soft), ceramics, and cements for use in aerospace composites, civil infrastructure, orthopedic implants, robotics, and human interfacing technology (e.g. touchscreens/track pads). Despite the enormous attention that these fields have attracted, critical gaps remain. As a first example, the current state of the art is currently unable to accurately predict macroscale conductivity changes in a piezoresistive material due to an arbitrary or general deformation. This is a consequence of the state of the art focusing much more on understanding the microscale mechanisms of piezoresistivity (particularly in nanocomposites). And as a second example, AC-based piezoresistivity has received little-to-no attention despite its advantages over DC-based self-sensing. In light of these considerations, the following Problem Statement and Research Goal are formulated resulting in the following Thesis Contributions.

Problem Statement: Piezoresistive self-sensing has much potential to positively impact diverse and far-reaching applications which require knowledge on the strain state of in-use structures and materials. Existent tools for modeling piezoresistivity, however, are inadequate for making meaningful macroscale predictions due to arbitrary deformations. Further, AC piezoresistivity, despite its advantages over DC, is deeply understudied from a modeling perspective.

Research Goal: The goal of this thesis work is to develop conceptual frameworks for modeling the AC/DC transport-deformation relationship in piezoresistive materials at macroscales.

Thesis Contributions: This thesis work makes three important contributions to the state of the art.

- A first-ever higher-order general tensorial resistivity-strain relation is developed for isotropic piezoresistive materials subject to infinitesimal deformations. This relation is formulated in such a way that the piezoresistive response of *any* material can be quantified through the determination of few piezoresistive constants measured via simple experiments (i.e. analogous to the determination of elastic constants for stress-strain modeling). This modeling framework is then experimentally validated with good accuracy.

- A conceptual framework for the macroscale modeling of AC piezoresistivity is developed in the form of the universal dielectric response (UDR) with strain-dependent fitting parameters.

- A novel piezoresistive switching behavior was observed in CNF/epoxy during the course of the second contribution. Microscale modeling revealed the mechanism of this switching behavior to be deformation-dependent electron tunneling acting in parallel with inter-filler capacitive coupling. Thus, basic knowledge on microscale AC transport in these materials is contributed.

The remainder of this document is organized as follows: First, the basic forms of the macroscale DC/AC transport-deformation modeling frameworks are presented. Then, experimental procedures including manufacturing, test specimen preparation, measurement methods, and electrical/mechanical properties are presented. The proposed DC tensorial relation is then fit to experimental data to determine the piezoresistive constants. Next, the predictions of the tensorial relation are experimentally validated. Following this, in order to characterize AC electrical properties with respect to mechanical effects, experimental AC conductivity measurements are fit to

a Jonscher's power law utilizing the UDR for each step of mechanical loading, and fitting parameters are expressed as a function of strain. The novel observation of switching behavior in piezoresistivity is explained and its underlying physical mechanism is described via EIS analyses and a micromodel. Finally, this thesis is closed with a summary, conclusions, and recommendations for future work in this area.

3. PRESENTATION OF GENERAL MACROSCALE FRAMEWORKS FOR DC/AC-STRAIN COUPLING

3.1 Introduction

Considerable effort has been dedicated to modeling piezoresistivity due to the potential for intrinsic self-sensing and in light of the motivation for having a quantitative understanding of the resistivity-strain relationship. However, approaches in the state of the art have noteworthy challenges. Among these challenges, the complexity of predicting the resistivity-strain response of a particular material is especially noteworthy. That is, prevailing approaches necessitate deep knowledge of the underlying microstructure of the material. It is important to note that this work is not claiming that such complexity is intrinsically a detriment. Rather, existing microstructural approaches have resulted in great insights into the basic mechanisms of piezoresistivity in many materials thereby unlocking very fundamental insight into self-sensing materials. However, consider a practicing engineer who wants to utilize the piezoresistive effects to make meaningful predictions. For this, the engineer certainly *could* use complex computational tools and/or micromechanics, but simple laboratory tests are likely much preferred and indeed more pragmatic in such a case. This hypothetical situation can be likened to stress modeling. That is, consider again a practicing engineer who needs to use a new unknown material in a load-bearing component. To do this, the engineer could conduct microscale analyses to elucidate the macroscale mechanical properties of the new material. More realistically, however, the engineer would conduct simple laboratory tests to determine elastic constants such as Young's modulus and Poisson's ratio. The motivation for this chapter is much the same. In order to effectively use the piezoresistive effect, quantification of the resistivity-strain relationship that is amenable to arbitrary strain states is required. For this, simple

tensorial relations which can be fully characterized by a few piezoresistive constants that are easily obtained via macroscale experiments is necessary. Therefore, this chapter makes two important contributions. First the framework for a general tensorial relation for resistivity-strain coupling is presented. Next, a framework for modeling deformation-dependent AC conductivity at the macroscale is described. Later in this thesis, these frameworks are applied to experimental data.

3.2 DC Piezoresistivity

Before presenting the DC piezoresistivity framework developed in this work, it is important to first acknowledge related work. In 1951, Druyvesteyn [114] described the variation of resistivity of some metals due to elastic deformation for the first time. Smith [115] later reported on the piezoresistive response of germanium and silicon due to shear stress. Together, they described tensor-based constitutive relations between the resistivity change and an arbitrary strain states as shown in equation (3.1) where ρ_{ij} is resistivity tensor, κ_{ijkl} is piezoresistive constitutive tensor, and ε_{kl} is the infinitesimal strain tensor. Repeated indices imply summation over the dimension of the problem. Equation (3.1) can be explicitly expanded as equation (3.2) where infinitesimal strain is defined in equation (3.3). Drawing from this, Gruener *et al.* [116] and Zhao *et al.* [117] recently investigated geometry change-induced anisotropic resistivity changes for inkjet-printed carbon nanotube-polymer thin film. Using the thin film, two dimensional anisotropic piezoresistivity was characterized. However, they incompletely identified constitutive terms due to discrepancies between piezoresistive responses in compression and tension as shown in Figure 3.1. Further, they assumed linear relations with strain although the piezoresistive response is non-linear. Therefore, the goal of this section is to derive a higher-order deformation-resistivity tensorial relation that is amenable to arbitrary strain states and simultaneously takes into account non-linear piezoresistive effects.

$$\Delta\rho_{ij} = \kappa_{ijkl}\varepsilon_{kl} \tag{3.1}$$

$$\begin{Bmatrix} \Delta\rho_{11} \\ \Delta\rho_{22} \\ \Delta\rho_{33} \\ \Delta\rho_{23} \\ \Delta\rho_{31} \\ \Delta\rho_{12} \end{Bmatrix} = \begin{bmatrix} \kappa_{1111} & \kappa_{1122} & \kappa_{1133} & \kappa_{1123} & \kappa_{1131} & \kappa_{1112} \\ \kappa_{2211} & \kappa_{2222} & \kappa_{2233} & \kappa_{2223} & \kappa_{2231} & \kappa_{2212} \\ \kappa_{3311} & \kappa_{3322} & \kappa_{3333} & \kappa_{3323} & \kappa_{3331} & \kappa_{3312} \\ \kappa_{2311} & \kappa_{2322} & \kappa_{2333} & \kappa_{2323} & \kappa_{2331} & \kappa_{2312} \\ \kappa_{3111} & \kappa_{3122} & \kappa_{3133} & \kappa_{3123} & \kappa_{3131} & \kappa_{3112} \\ \kappa_{1211} & \kappa_{1222} & \kappa_{1233} & \kappa_{1223} & \kappa_{1231} & \kappa_{1212} \end{bmatrix} \begin{Bmatrix} \varepsilon_{11} \\ \varepsilon_{22} \\ \varepsilon_{33} \\ \varepsilon_{23} \\ \varepsilon_{31} \\ \varepsilon_{12} \end{Bmatrix} \tag{3.2}$$

$$\varepsilon_{ij} = \frac{1}{2}\left(\frac{\partial u_i}{\partial x_j} + \frac{\partial u_j}{\partial x_i}\right) \tag{3.3}$$

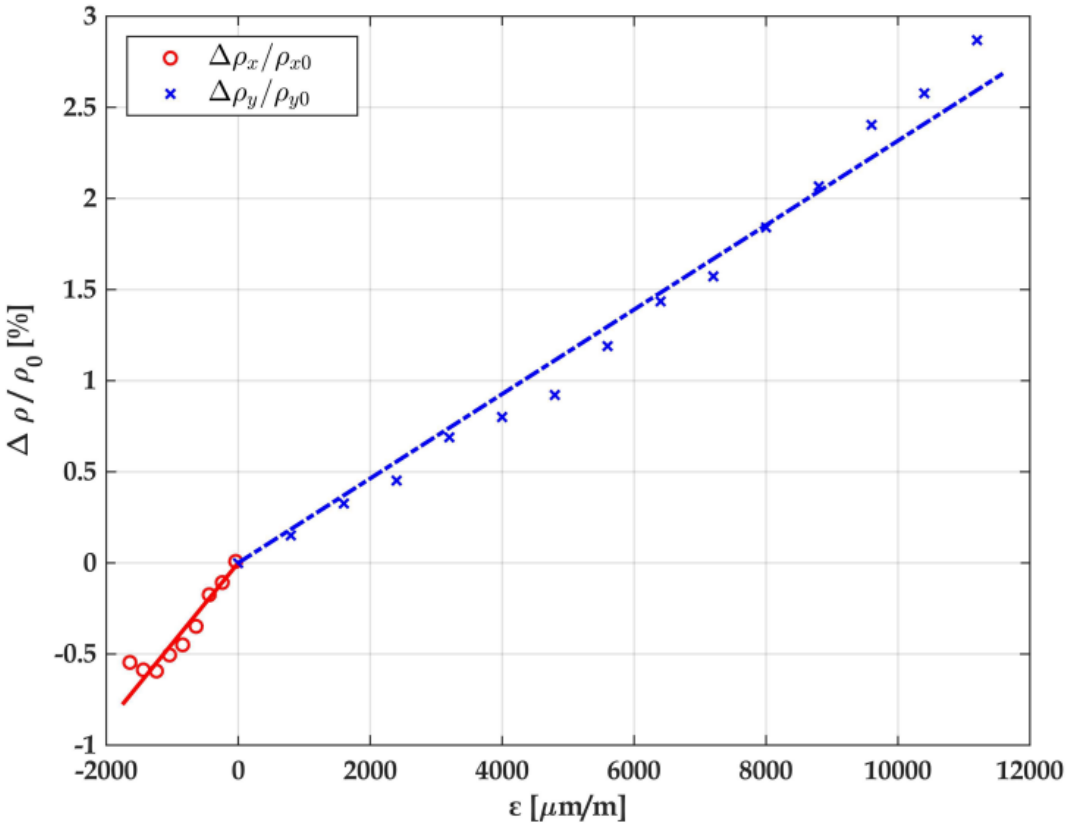

Fig. 3.1. Normalized resistivity change with respect to strain. Note the difference between the slope in tension and compression [116].

3.2.1 General Form of Higher-Order Resistivity-Strain Relations

Herein, a general formulation for a higher-order tensor-based piezoresistive relation is proposed with three assumptions: i) all strains are infinitesimal, ii) resistivity changes are isotropic for infinitesimal strains, and iii) resistivity changes are non-linear for infinitesimal strains. The second assumption implies that some linear-elastic material has been modified with some weight fraction of conductive fillers above the percolation threshold thereby manifesting deformation-dependent electrical resistivity without anisotropy (i.e. no directional preference of resistivity changes). This can be justified in light of the fact that geometry changes are relatively small for small strains such that changes in resistivity are dominated by altering the connectedness of the filler network. While alignment of high aspect-ratio fillers can induce anisotropic conductivity [93] and very large deformations can also induce high aspect-ratio fillers to reorient thereby producing anisotropic changes in resistivity, such large deformations are necessarily outside of the scope of a linear-elastic material subject to infinitesimal strains. Particularly for the material system in this research, fracture would occur before deformations become large enough to induce appreciable alignment. The third assumption is in light of the well-documented fact that the piezoresistive effect in tension is greater than that in compression and decidedly non-linear [118]. Based on these assumptions, the following higher-order tensorial resistivity-strain relation is proposed.

$$\Delta\rho = \kappa_{ij}\varepsilon_{ij} + \Pi_{ijkl}\varepsilon_{ij}\varepsilon_{kl} \tag{3.4}$$

Above, $\Delta\rho$ is the resistivity change, ε_{ij} is the infinitesimal strain tensor, and κ_{ij} and Π_{ijkl} are second and fourth-order tensors relating resistivity changes to strains. Repeated indices imply summation over the dimension of the problem. Before further exploring the tensors, several clarifications should be noted. First, this resistivity-strain relation is not claimed to be an actual constitutive relation since it is not derived from energy arguments and resistivity and strain are not energy complements.

Instead, the goal for this approach is to develop a relation which can accurately predict changes in resistivity due to an arbitrary strain state. Second, $\Delta\rho$ has been utilized rather than absolute resistivity (i.e. ρ) in order to reduce specimen-to-specimen variability by making the left-hand side of equation (3.4) equal to zero for a state of zero strain. And third, unlike the prior work summarized above, the resistivity change is assumed to be a scalar quantity. This can be justified as follows. Although resistivity changes are possibly treated as having some directional dependence, Abascal *et al.* [119] showed that directional dependence in change in resistivity is exceeding small for infinitesimal strains. Therefore, resistivity changes can be well-approximated as a scalar quantity. It is also acknowledged that this second assumption significantly simplifies the model calibration process. This assumption is validated later in Chapter 5.

In light of these clarifications, the second-order tensor, κ_{ij}, and the fourth-order tensor, Π_{ijkl}, in equation (3.4) are next examined in greater detail. Considering the assumption that resistivity changes due to deformation have no directional dependence, the most general isotropic second and fourth-order tensors for κ_{ij} and Π_{ijkl} are selected as shown in equations (3.5) and (3.6), respectively.

$$\kappa_{ij} = \kappa\delta_{ij} \tag{3.5}$$

$$\Pi_{ijkl} = \alpha\delta_{ij}\delta_{kl} + \beta\delta_{ik}\delta_{jl} + \gamma\delta_{il}\delta_{jk} \tag{3.6}$$

Above, δ_{ij} is the Kronecker-delta and κ, α, β, and γ are constants to be determined by fitting equation (3.4) to experimental data. Equation (3.7) is the simplified version of equation (3.4) obtained by plugging equations (3.5) and (3.6) into equation (3.4), expanding, and making use of the replacement property of the Kronecker-delta.

$$\Delta\rho = \kappa\varepsilon_{ii} + \alpha\varepsilon_{ii}\varepsilon_{jj} + (\beta+\gamma)\varepsilon_{ij}\varepsilon_{ij} \tag{3.7}$$

For notational convenience in equation (3.7), α is replaced with Π_1 and the parenthetical term, $(\beta+\gamma)$, is replaced with Π_2. These undetermined constants, κ, Π_1,

and Π_2, are referred to as piezoresistive constants. This also helps delineate terms as being related to the linear contribution, κ, and the non-linear contributions, Π_1 and Π_2. After these replacements, the proposed higher-order tensorial piezoresistive relation can be rewritten as equation (3.8), and equation (3.8) can be explicitly expanded as equation (3.9).

$$\Delta\rho = \kappa\varepsilon_{ii} + \Pi_1\varepsilon_{ii}\varepsilon_{jj} + \Pi_2\varepsilon_{ij}\varepsilon_{ij} \tag{3.8}$$

$$\begin{aligned}\Delta\rho = {} & \kappa(\varepsilon_{11} + \varepsilon_{22} + \varepsilon_{33}) + (\Pi_1 + \Pi_2)(\varepsilon_{11}^2 + \varepsilon_{22}^2 + \varepsilon_{33}^2) \\ & + 2\Pi_1(\varepsilon_{11}\varepsilon_{22} + \varepsilon_{22}\varepsilon_{33} + \varepsilon_{33}\varepsilon_{11}) + 2\Pi_2(\varepsilon_{12}^2 + \varepsilon_{23}^2 + \varepsilon_{31}^2)\end{aligned} \tag{3.9}$$

3.2.2 Isolation of Piezoresistive Constants

In order to utilize the piezoresistive relations shown in equations (3.8) and (3.9), the piezoresistive constants need to be isolated. That is, by applying specific strain states, the general equations can be reduced to simpler forms and can be fit to experimental data by treating κ, Π_1, and Π_2 as fitting parameters. First, consider a case of uniaxial stress applied in the x_1-direction. In such a case, $\varepsilon_{11} \neq 0$ and $\varepsilon_{22} = \varepsilon_{33} = -\nu\varepsilon_{11}$ where ν is Poisson's ratio and all off-diagonal terms of $\varepsilon_{ij} = 0$. For this state of strain, equation (3.9) reduces to equation (3.10).

$$\Delta\rho = \kappa(1 - 2\nu)\varepsilon_{11} + (\Pi_1 + \Pi_2 - 4\Pi_1\nu + (3\Pi_1 + \Pi_2)\nu^2)\varepsilon_{11}^2 \tag{3.10}$$

Next, consider a case of simple shear in which $\varepsilon_{12} \neq 0$ and all other $\varepsilon_{ij} = 0$. Under these conditions, equation (3.9) reduces to equation (3.11).

$$\Delta\rho = 2\Pi_2\varepsilon_{12}^2 \tag{3.11}$$

Therefore, the piezoresistive constants can be determined by experimentally inducing these strain states and fitting the reduced equations to experimental data. This will be shown later in Chapter 5.

3.3 AC Piezoresistivity

Next, we turn our attention to deformation-dependent AC conductivity. As discussed earlier in Chapter 1, AC-based self-sensing has important advantages over DC, but much less work has been done in this area. Therefore, conceptual frameworks such as herein proposed are important for proliferating AC-based self-sensing. Before introducing this framework, however, a brief description of AC conductivity is first provided. General AC electrical properties are described by the electrical admittivity of a material as $\xi = \sigma_{DC} + j\omega\epsilon$ where ξ is admittivity, σ_{DC} is the DC conductivity, ω is the angular frequency, and ϵ is the permittivity. However, permittivity is also a complex-valued property as $\epsilon = \epsilon' - j\epsilon''$. Therefore, admittivity can be rephrased as $\xi = (\sigma_{DC} + \omega\epsilon'') + j\omega\epsilon'$ and the parenthetical term recognized as AC conductivity, σ_{AC}. The product $\omega\epsilon'$ is also referred to as the susceptivity.

With this primer out of the way, we return to establishing a general framework for the effect of deformation on AC conductivity. For this, the UDR is identified as a promising tool to model AC piezoresistivity. The UDR states that the frequency-dependent properties of multi-phase materials exhibit a power law with respect to frequency [120] such that AC conductivity can be described by the following equation.

$$\sigma_{AC} = \sigma_{DC} + K\omega^n \tag{3.12}$$

Above, σ_{DC} is again the DC conductivity, ω is again the angular frequency of the electrical excitation, and K and n are fitting constants. This is also known as Jonscher's power law [121]. This way of expressing AC conductivity is advantageous for modeling AC piezoresistivity because it intrinsically expresses the AC conductivity as a function of frequency. In other words, if the parameters σ_{DC}, K, and n can be expressed as a function of strain, it will be possible to predict the macroscale change in AC conductivity for any given frequency and any given strain. To date, however, the effect of deformation on AC conductivity has been largely unexplored. Therefore, an important contribution of this work will be exploring the basic responsiveness of

these parameters of Jonscher's power law to strain. This will be explored later in Chapter 5.

3.4 Summary and Conclusion

In summary, this chapter has proposed two frameworks for modeling DC and AC piezoresistivity at the macroscale – a general higher-order resistivity-strain tensor-based relation and Jonscher's power law with strain-dependent fitting parameters, respectively. This was motivated by the potential of self-sensing materials for intrinsic self-sensing, the need for quantifying the deformation-resistivity relationship, and limitations associated with prevailing piezoresistivity models. To develop the DC-based piezoresistive relation, several assumptions were made: i) all strains are infinitesimal, ii) the material is isotropic with regard to resistivity changes (i.e. strains produce the same resistivity change in all directions), and iii) resistivity changes due to infinitesimal strain are non-linear. Mindful of these assumptions, a general tensorial form with higher-order strain products has been postulated. After postulating this general form, methods of inducing specific strain states in order to isolate piezoresistive constants to be determined by curve-fitting were identified. Next, the UDR (Jonscher's power law, specifically) was proposed for modeling AC piezoresistivity. This was selected because it intrinsically accounts for frequency dependency in AC conductivity. That is, the frequency-strain-AC conductivity relation can be characterized by expressing parameters, σ_{DC}, K, and n as a function of strain.

In light of the preceding, several conclusions can be made. First, compared to prevailing DC piezoresistivity models, this model is much more accessible for engineers without a deep understanding of computational micromechanics. Indeed, this approach was inspired by the manner in which elastic constants are found (i.e. via simple experiments rather than via computational micromechanics). Second, due to the generality of the formulation, it can be applied to a wide range of piezoresistive materials such as cementitious-based, ceramic-based, or polymeric-based nanocom-

posites. Third, once piezoresistive constants are determined, this approach can readily be integrated with finite element methods for analyzing complex structures.

4. EXPERIMENTAL PROCEDURES

4.1 Introduction

Next, the experimental procedures used in this work are presented. Specifically, this will include how a representative piezoresistive material was manufactured, how test specimens were prepared, how test specimens were mechanically loaded, how electrical measurements were collected, and how DC and AC properties and mechanical properties of test specimens are described. These materials and methods are then applied to the previously described macroscale modeling frameworks.

CNF-modified epoxy is herein used as a representative piezoresistive material. This material was used because it is simple to produce (thereby allowing for greater emphasis on the novel contributions of this work – the development of macroscale modeling procedures), its manufacturing methods are well-documented, and it satisfies our assumptions of being linear-elastic and isotropic (isotropic resistivity changes are verified later). Therefore, even though a specific material type was used in this work, the general macroscale modeling frameworks proposed may be directly applicable to similar classes of piezoresistive materials such as self-sensing cements and ceramics.

4.2 CNF-Modified Epoxy Manufacturing

CNF/epoxy specimens were manufactured with 0.5, 1.0, and 1.5 wt.% Pyrograf III PR 24-XT-HHT CNFs (purchased from Applied Sciences) dispersed in Fibre Glast System 2000 epoxy resin, Fibre Glast 2060 epoxy curing agent, Triton X-100 surfactant, and BYK-A 501 air release agent. These weight fractions of CNFs were selected to be above the percolation threshold for this CNF/epoxy combination and man-

ufacturing method, which is approximately 0.25 wt.%, based on previous work by Tallman and Hassan [122]. According to the manufacturer's description, these CNFs are treated at 3000 °C to achieve high graphitization with very low iron content. The CNFs have an average diameter of 0.1 μm, as-produced lengths ranging from 50 to 200 μm, and a surface area of 41 m^2/g [123].

Dog-bone and v-notched specimens were produced by casting CNF/epoxy in two-part silicone molds produced from Smooth-On Mold Star 20T. Six specimens for each weight fraction were produced – three for uniaxial testing and three for shear testing. Dog-bone specimens (left of Figure 4.1) were chosen for the uniaxial testing in order to induce a state of uniaxial stress in the gauge section. V-notched specimens (right of Figure 4.1) were selected for shear testing to induce uniform shear strain within the test area. Dog-bone specimens were shaped according ASTM-D638 [124] but with a reduced gauge length in order to protect against buckling. Buckling calculations will be explained in section 4.3. Molds for v-notched specimens were produced with dimensions according to ASTM-D7078 [125].

Once the molds were ready, appropriate weights of epoxy resin and CNFs were weighed in a beaker. Then, surfactant and acetone were added. A surfactant-to-CNF weight ratio of 0.76:1 and resin-to-acetone volume ratio of 2:1 were used. Acetone decreases the viscosity of the mixture and surfactant helps to facilitate effective dispersion. The combination of resin, CNFs, surfactant, and acetone was mixed for 5 minutes in a Thinky AR-100 planetary centrifuge and sonicated for four hours in a bath sonicator (Crest Powersonic CP200HT). According to the specification of the manufacturer, the sonicator operates at an average power of 35 W and a frequency of 45 kHz. After sonication, the mixture was stirred on a hot plate stirrer for 24 hours at 600 rpm and 60 °C in order to evaporate the acetone. Acetone weight was tracked to ensure its complete evaporation. After evaporating the acetone, the mixture was cooled down to room temperature to prevent premature curing. Then, an air release agent and curing agent were added. An air release agent-to-epoxy weight ratio of 0.003:1 and a manufacturer-specified hardener-to-resin weight ratio of 27:100

were used. The mixture was gently stirred by hand for five minutes and degassed in a vacuum chamber for 30 minutes at room temperature. While the mixture was degassed, the mold was coated with mold release agent (Fibre Glast 1153) for easy removal of CNF/epoxy specimens. After degassing, the mixture was poured into the mold, placed in an oven, and cured for five hours at 60 °C.

Left over material was imaged via scanning electron microscope (SEM) in order to assess the distribution of CNFs in the polymer matrix. A fracture surface can be seen in Figures 4.2 and 4.3 showing that, at least within the purview of the SEM image, CNFs seem to be reasonably well-dispersed. SEM images were generated by ThermoFisher Teneo System. Fracture surfaces were sputter-coated with a thin layer of platinum prior to imaging.

4.3 Test Specimen Preparation

The shape of the dog-bone specimen is based on ASTM-D638 [124]. For uniaxial testing, a range of axial strains from -6000 $\mu\varepsilon$ to 6000 $\mu\varepsilon$ is desired. The original critical buckling load of a 165 mm-length of dog-bone specimens based on ASTM-D638 [124] is 668.65 N. This load is close to the critical load for a fixed-fixed column of this length according to $P_{cr} = (\pi^2 EI)/(KL)^2$. Here, E, I, K, and L are elastic modulus, moment of inertia, column effective factor, and unsupported length of the column, respectively. Therefore, the length of the specimen was reduced to 125 mm which increases the critical buckling load to 1804.7 N. This modification allows the test to go from -6000 $\mu\varepsilon$ to 6000 $\mu\varepsilon$ without any threat of buckling.

With the dimensions set for uniaxial testing, two electrodes measuring 13 mm $\times$ 13 mm were attached to measure resistance changes through the thickness of the dog-bone specimen as shown in the left of Figure 4.4. Prior to attaching electrodes, the test area was sanded and cleaned with acetone. Then, silver paste (purchased from Ted Pella) was applied and copper tape was attached on top of the dried silver paste to minimize the effect of contact impedance. Once the electrodes were attached,

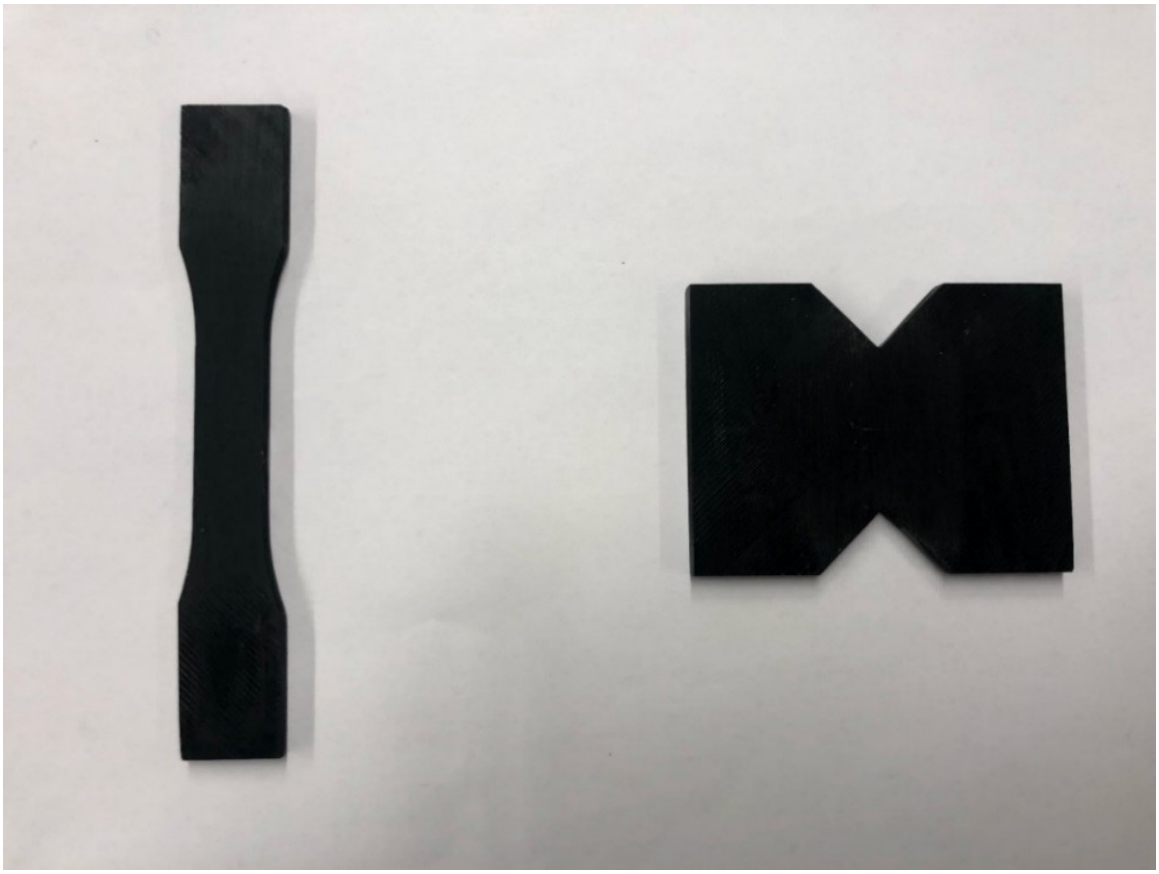

Fig. 4.1. Representative CNF/epoxy specimens. Left: shortened dog-bone specimen for uniaxial testing. Right: v-notched specimen for shear testing

uniaxial strain gages were also attached below the electrodes in the axial and the transverse directions. In order to electrically isolate the test specimens from the load frame, insulating tabs made of fiberglass were attached on the grip sections.

Per ASTM-D7078 [125], a 90° notch angle was chosen for v-notched specimens. To measure electrical properties, electrodes measuring 10 mm × 10 mm were attached near the center of the specimen where shear strains are uniform per the standard referenced previously. After electrodes were attached, a rosette strain gage was also installed on each specimen. Note that negative shear strain cannot be applied in this experiment due to the geometry of the v-notched rail shear fixture. As can be

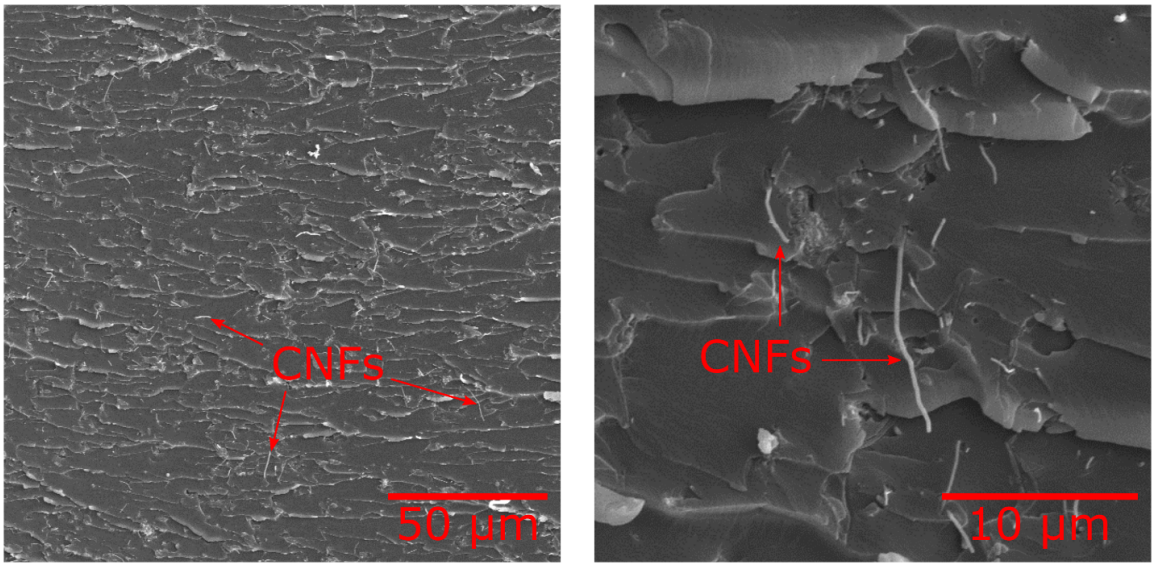

Fig. 4.2. Representative SEM images of 1.5 wt.% CNF/epoxy specimens generated during this work.

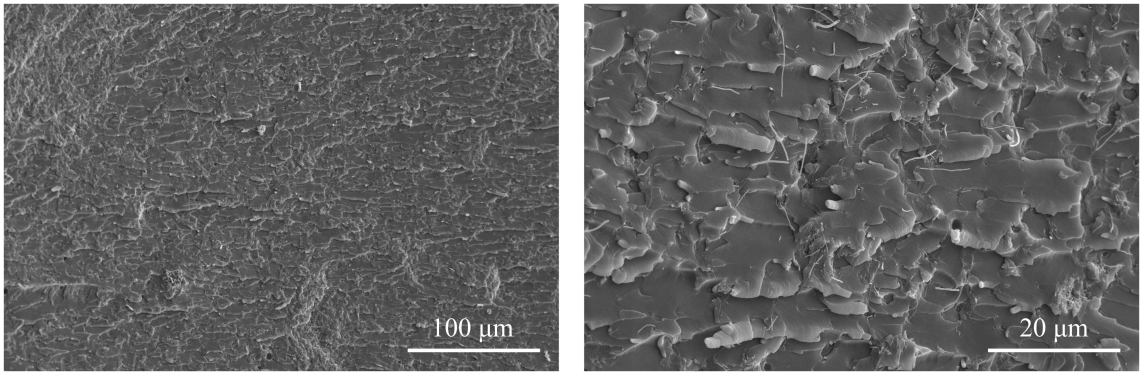

Fig. 4.3. Representative SEM images of 1.0 wt.% CNF/epoxy specimens generated during this work.

seen in the right of Figure 4.4, the fixture would contact itself if displaced downward. Therefore, shear strain was only applied in one direction.

4.4 CNF/Epoxy DC Electrical Properties

After manufacturing, resistance measurements were collected as the specimens were strained. This was done using a current source (Keithley 6221) and a voltage data acquisition (DAQ) card (National Instruments PXIe-6368) by the four-point method. Current magnitudes were selected to keep voltages within the 10 V range of the DAQ. From the voltage-current relationship, resistance was calculated. Traditionally, resistivity is calculated on prismatic specimens via equation (4.1), where ρ is the resistivity, R is the resistance, A is the cross-sectional area perpendicular to the measurement direction, and L is the length along the measurement direction.

$$\rho = \frac{RA}{L} \tag{4.1}$$

However, the specimens herein considered are not prismatic in a way that is amenable to equation (4.1) while also being able to be put in the load frame. This is because electrodes cannot realistically be applied over the entire face of a specimen during loading. Therefore, a method of determining resistivity from resistance measurements is needed. In light of this difficulty, resistivity changes are calculated from resistance changes by comparison to a model. To do this, finite element models of the dog-bone and v-notched geometries were produced. In these models, a uniform resistivity distribution was found to match model-predicted inter-electrode resistances to experimentally measured inter-electrode resistances. Strains were applied to models in the same way as the experiments. The uniform resistivity distribution of the model is then updated at each strain state to again match model-predicted inter-electrode resistances to experimentally measured inter-electrode resistances. It is important to note that no piezoresistivity models were utilized in this process. This approach also has the advantage of accounting for deformation-induced geometric effects. That is, this approach considers electrode shapes changing and inter-electrode distance changing due to the Poisson effect (i.e. becoming closer together or further apart during uniaxial testing).

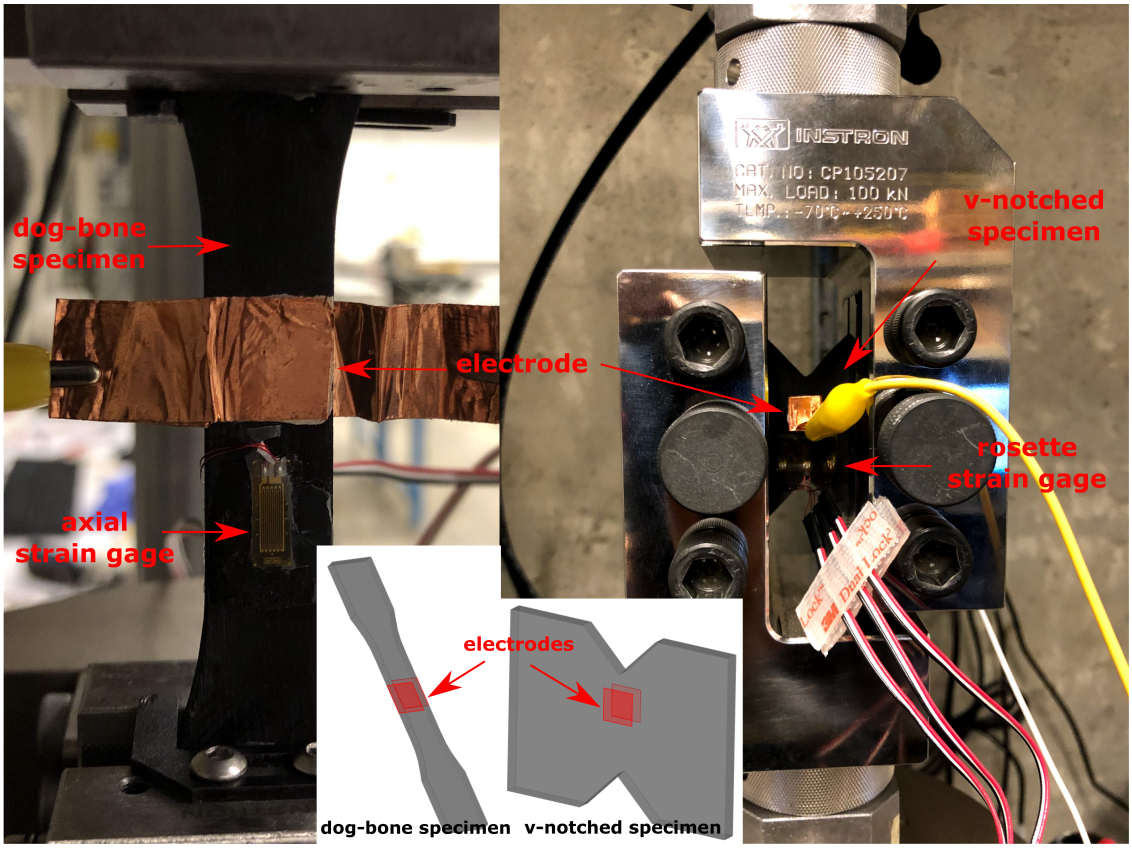

Fig. 4.4. A dog-bone and v-notched specimen loaded in the load frame with electrodes and a strain gage attached. Inset figures describe electrode placement for the dog-bone and the v-notched specimen.

Two sets of finite element simulations were used in this work – an elastic model to simulate the applied deformation and a steady-state electrical diffusion model to simulate the voltage-current relationship between the electrodes subject to the complete electrode model (CEM) boundary conditions. All modeling was done using code developed in-house by the author. Linear elastic finite element methods are very well documented elsewhere so they will not be covered here in any depth. CEM, however, is not nearly as well known. Therefore, a summary of the governing equations is provided below. Additional details on the discretization process are provided

in Appendix A. Steady-state diffusion begins with Laplace's equation as shown in equation (4.2) in the absence of internal sources.

$$\boldsymbol{\nabla} \cdot \frac{1}{\rho} \boldsymbol{\nabla} \phi = 0 \tag{4.2}$$

Above, ρ is the resistivity of the material and ϕ is the domain potential. CEM boundary conditions add an additional degree of freedom corresponding to each electrode, assumes the electrodes are perfect conductors (and hence at a constant voltage), and accounts for contact impedance between the domain and the electrodes. CEM boundary conditions and conservation of charge are enforced on the diffusion equation via equations (4.3) and (4.4), respectively. Equation (4.3) takes into account the contact impedance-induced voltage drop between the electrodes and the domain whereas equation (4.4) stipulates that current-in equals current-out.

$$\phi + z_l \frac{1}{\rho} \boldsymbol{\nabla} \phi \cdot \boldsymbol{n} = V_l \tag{4.3}$$

$$\sum_{l=1}^{L} \int_{E_l} \frac{1}{\rho} \boldsymbol{\nabla} \phi \cdot \boldsymbol{n} \, \mathrm{d}S_l = 0 \tag{4.4}$$

Above, z_l is the contact impedance between the lth electrode and the domain, $\boldsymbol{n}$ is an outward pointing normal vector, V_l is the voltage on the lth electrode, E_l is the area of the lth electrode, and L is the total number of electrodes. These governing equations and boundary conditions can be easily solved by discretization via the finite element method as shown in equation (4.5).

$$\begin{bmatrix} \mathbf{A}_M + \mathbf{A}_Z & \mathbf{A}_W \\ \mathbf{A}_W^T & \mathbf{A}_D \end{bmatrix} \begin{bmatrix} \mathbf{\Phi} \\ \mathbf{V} \end{bmatrix} = \begin{bmatrix} 0 \\ \mathbf{I} \end{bmatrix} \tag{4.5}$$

$$\mathbf{A}^e_{M\,ij} = \int_{\Omega_e} \frac{\partial w_i}{\partial x_k} \rho^{-1}_{kl} \frac{\partial w_j}{\partial x_l} \, \mathrm{d}\Omega_e \tag{4.6}$$

$$\mathbf{A}_{Z\,ij} = \sum_{l=1}^{L} \int_{E_l} \frac{1}{z_l} w_i w_j \, \mathrm{d}S_l \tag{4.7}$$

$$\mathbf{A}_{W\,li} = -\int_{E_l} \frac{1}{z_l} w_i \, \mathrm{d}S_l \tag{4.8}$$

$$\mathbf{A}_D = \mathrm{diag}\left(\frac{E_l}{z_l}\right) \tag{4.9}$$

Above, $\mathbf{\Phi}$ is a vector of domain potentials, $\mathbf{V}$ is a vector of voltages on electrodes, $\mathbf{I}$ is a vector of currents applied to the electrodes (the components of $\mathbf{I}$ must sum to zero), and w_i is the ith finite element weighting function. Linear tetrahedral elements are used in this study. Equation (4.6) describes the local diffusion stiffness matrix of the eth element. $\mathbf{A}_Z$, $\mathbf{A}_W$, and $\mathbf{A}_D$ are defined in equations (4.7) - (4.9) to take into account the additional degree of freedom due to the electrodes and also incorporate the effect of contact impedance. Note also that ρ_{kl}^{-1} is the (potentially) anisotropic resistivity tensor such that $\rho_{kl}^{-1} = \sigma_{kl}$ where σ_{kl} is the conductivity tensor. For the case of isotropic resistivity, this simplifies as $\rho_{kl}^{-1} = \rho^{-1}\delta_{kl}$ where δ_{kl} is the Kronecker-delta and ρ is a scalar resistivity value.

In equation (4.5), it is assumed that voltage at the grounded electrode is zero. This can be enforced via $\sum_{l=1}^{L} V_l = 0$. It is important to note that equation (4.5) is only solvable up to an additive constant (i.e. ground point). However, this does not affect our results because voltage differences are used in our calculations. That is, for a given current injection, finite element simulation computes the inter-electrode voltage change. From this voltage change and knowing the applied current, resistance is calculated. A representative domain potential distribution on a dog-bone and v-notched specimen geometry can be seen in Figure 4.5. Detailed descriptions of finite element discretization of steady-state diffusion under CEM boundary conditions can be found in Appendix A.

And lastly, strain-free resistivity was plotted as a function of CNF weight fraction as shown in Figure 4.6. Nanocomposite resistivity is known to follow an exponential trend with respect to filler content. This exponential trend is clearly seen in Figure 4.6. The model prediction was calculated from the analytical model described in [101,126].

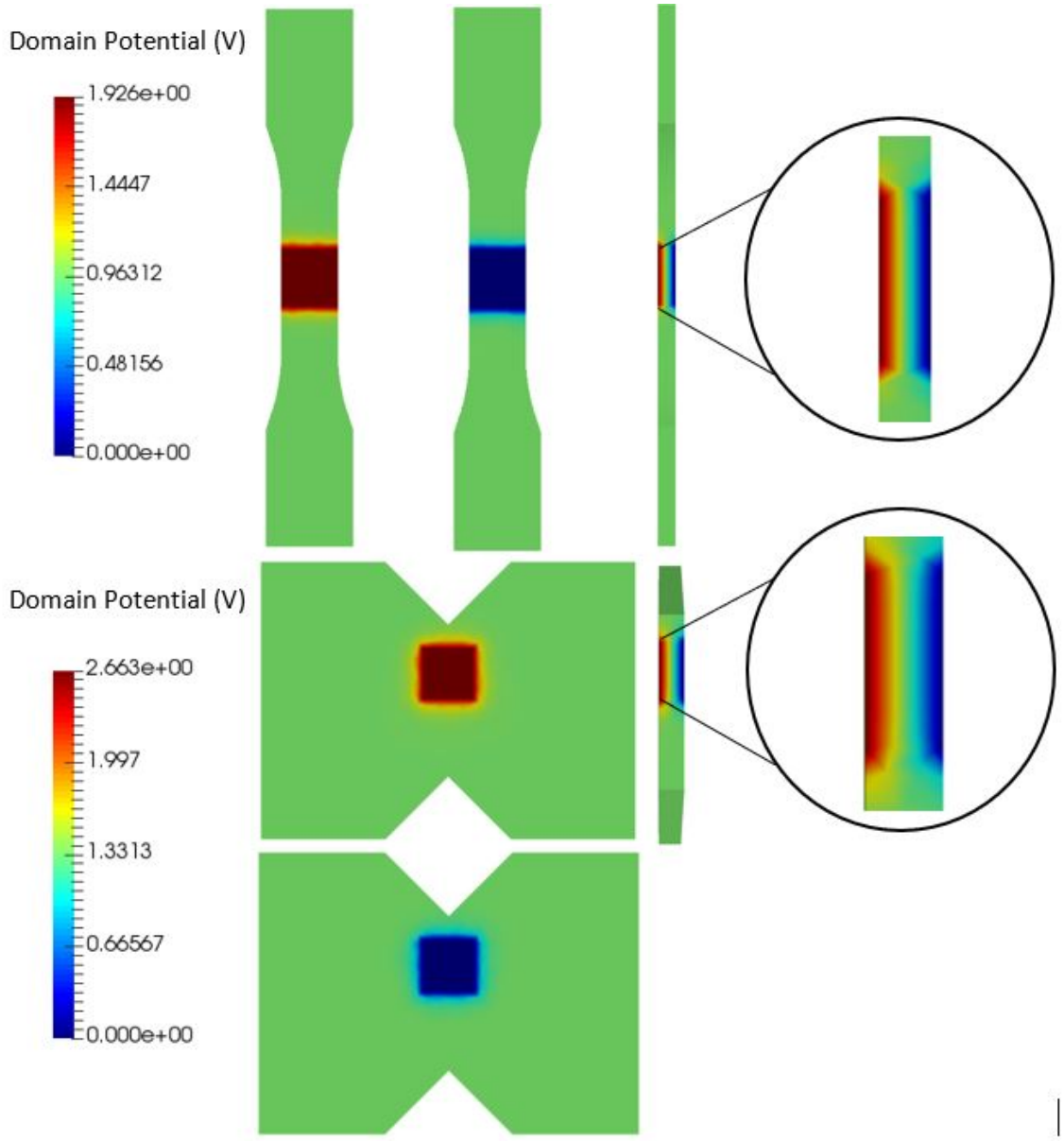

Fig. 4.5. A representative CEM solution on a dog-bone (top) and v-notched (bottom) geometry for 1.5 wt.% CNFs and a current injection magnitude of 10 mA.

4.5 CNF/Epoxy AC Electrical Properties

After DC measurements, AC measurements were collected for the same cases of axial and shear loading. Specifically, impedance magnitude, $|Z|$, and phase angle, θ,

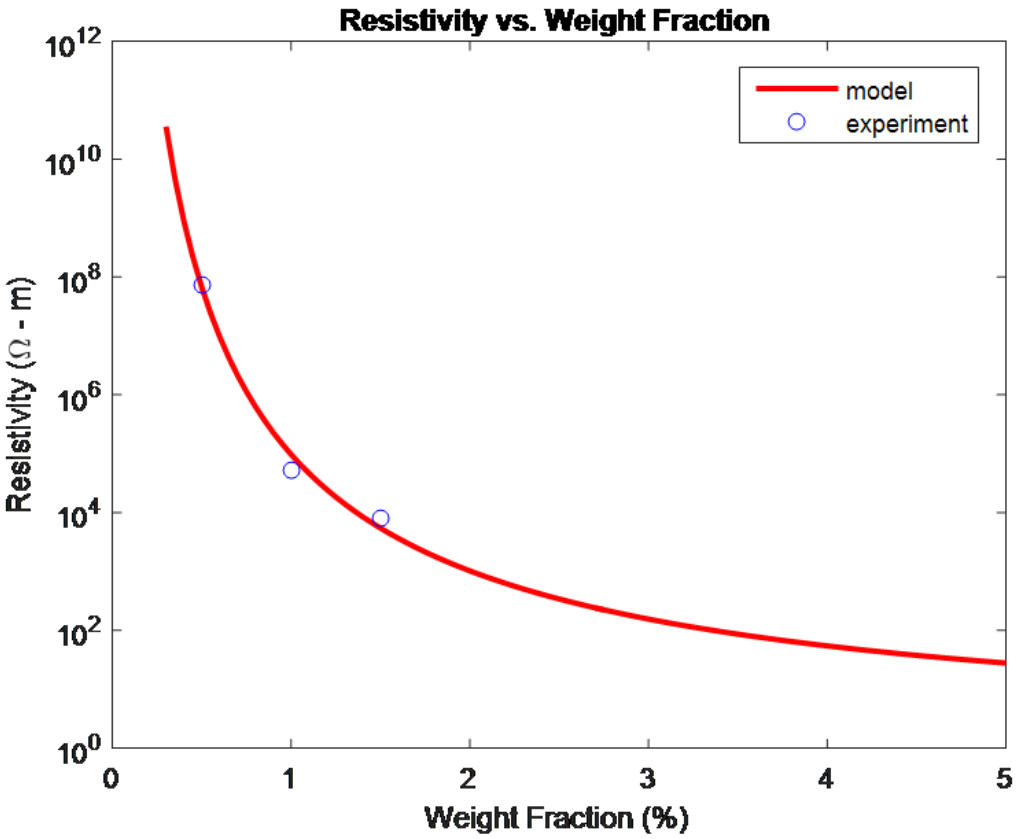

Fig. 4.6. Average experimentally determined resistivity at 0.5, 1.0, and 1.5 wt.%. CNFs and exponential trend line

were measured using a Keysight E4990A impedance analyzer sweeping from 100 Hz to 10 MHz. In order to obtain accurate in-situ electrical measurements, specimens were once again electrically isolated from the load frame by insulating tabs, the load frame was electrically grounded to the chassis ground of the impedance analyzer, and the impedance analyzer was calibrated to open and short conditions while in the load frame and test fixtures. The measured impedance and phase angle were converted to real and imaginary impedances ($Z = Z' + jZ''$ where Z is the complex impedance, Z' is the real impedance, Z'' is the imaginary impedance, and $j = \sqrt{-1}$ is the imaginary unit) via the equations shown below.

$$Z' = |Z| \cos(\theta) \tag{4.10}$$

$$Z'' = |Z| \sin(\theta) \tag{4.11}$$

AC conductivity is typically calculated as $\sigma_{AC} = L/AZ'$, where L is the length of a prismatic specimen along the measurement direction, and A is the face-covering cross-sectional electrode area. However, AC conductivity can be difficult to measure in this way on shapes such as dog-bone or v-notched specimens when they are mounted on a load frame since it is not practical to apply electrodes over the entire surface of a specimen during loading. In light of this, the effective AC conductivity is defined as shown below.

$$\tilde{\sigma}_{AC} = \frac{t}{A_e Z'} \tag{4.12}$$

Above, t is the specimen thickness (i.e. the distance between the electrodes), Z' is again the real part of the measured complex impedance, and A_e is the area of the measurement electrodes. The use of this definition can be justified because the effective AC conductivity defined above exhibits the same trend for AC conductivity versus frequency as measured on a prismatic specimen as shown in Figure 4.7. That is, both AC conductivity of a prismatic specimen and the effective AC conductivity defined in this chapter show two distinct regimes: one is a frequency-independent behavior (i.e. the flat portion of σ_{AC} curve). This region is also called as the DC region. In this regime, electrical transport through the conductive network is dominated by filler and inter-filler resistance, thus resulting in a nearly constant impedance response. Beyond this flat portion, the next regime exhibits frequency-dependent behavior (i.e. the portion of σ_{AC} curve that shows an exponential increase). In this region, AC conductivity increases dramatically with interrogation frequency. This is a consequence of filler and inter-filler AC effects (e.g. inter-filler regions acting as micro-capacitors, interfacial polarization between the conductive fillers and the non-conductive matrix,

etc.) starting to dominate net transport properties. Importantly, the definition of effective AC conductivity herein adopted allows for fitting to UDR relations.

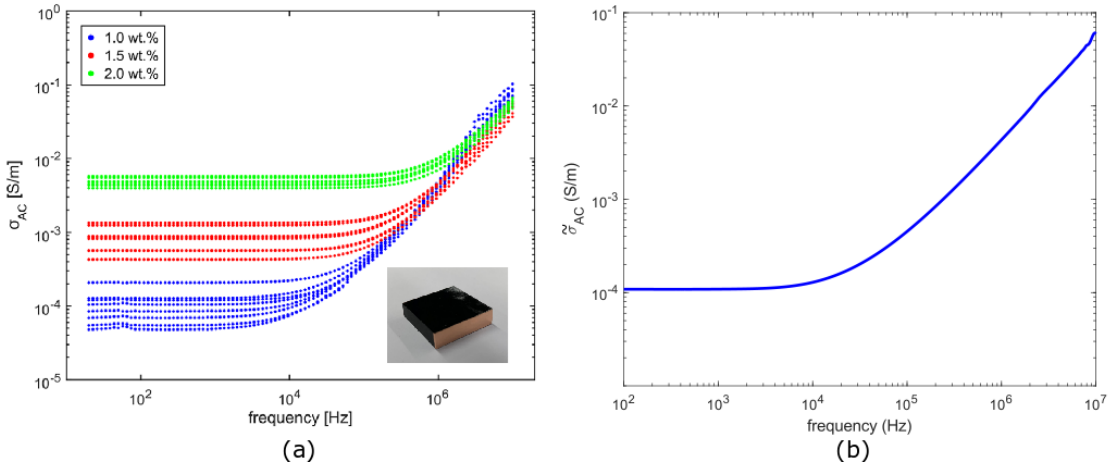

Fig. 4.7. (a) AC conductivity of prismatic specimens for 1.0, 1.5, and 2.0 wt.% CNF/epoxy. Inset figure shows the actual specimen for this measurement. Note that AC conductivity initially has flat portion and then increases exponentially with frequency [127]. (b) The effective AC conductivity measured for 1.5 wt.% CNF/epoxy. Note that the trend of the effective AC conductivity agrees with AC conductivity trend of prismatic specimens

4.6 CNF/Epoxy Mechanical Properties

While taking measurements of electrical properties of CNF/epoxy specimens, mechanical properties were recorded as well. Elastic modulus data is not necessarily needed for the tensor-based relation, but the stress-strain data confirms that the specimens are indeed in the linear-elastic region consistent with our assumptions for the development of a general tensorial model. On the other hand, Poisson's ratio is needed to determine the piezoresistive constants as described in equation (3.10) in Chapter 3 and can be determined by uniaxial testing with strain measurements in the axial and transverse directions.

Figure 4.8 shows the normal stress-normal strain plots for 0.5, 1.0, and 1.5 wt.% CNF/epoxy specimens. Elastic modulus was determined by a linear curve-fit of the data. It was found that elastic modulus increases with CNF weight fraction. Simultaneously, Poisson's ratio was also measured as shown in Figure 4.9. The experimental Poisson's ratio was approximately 0.3511 for all CNF weight fractions. This indicates that Poisson's ratio is not affected much by the addition of nanofillers. The elastic modulus and Poisson's ratio of each weight fraction are tabulated in Table 4.1.

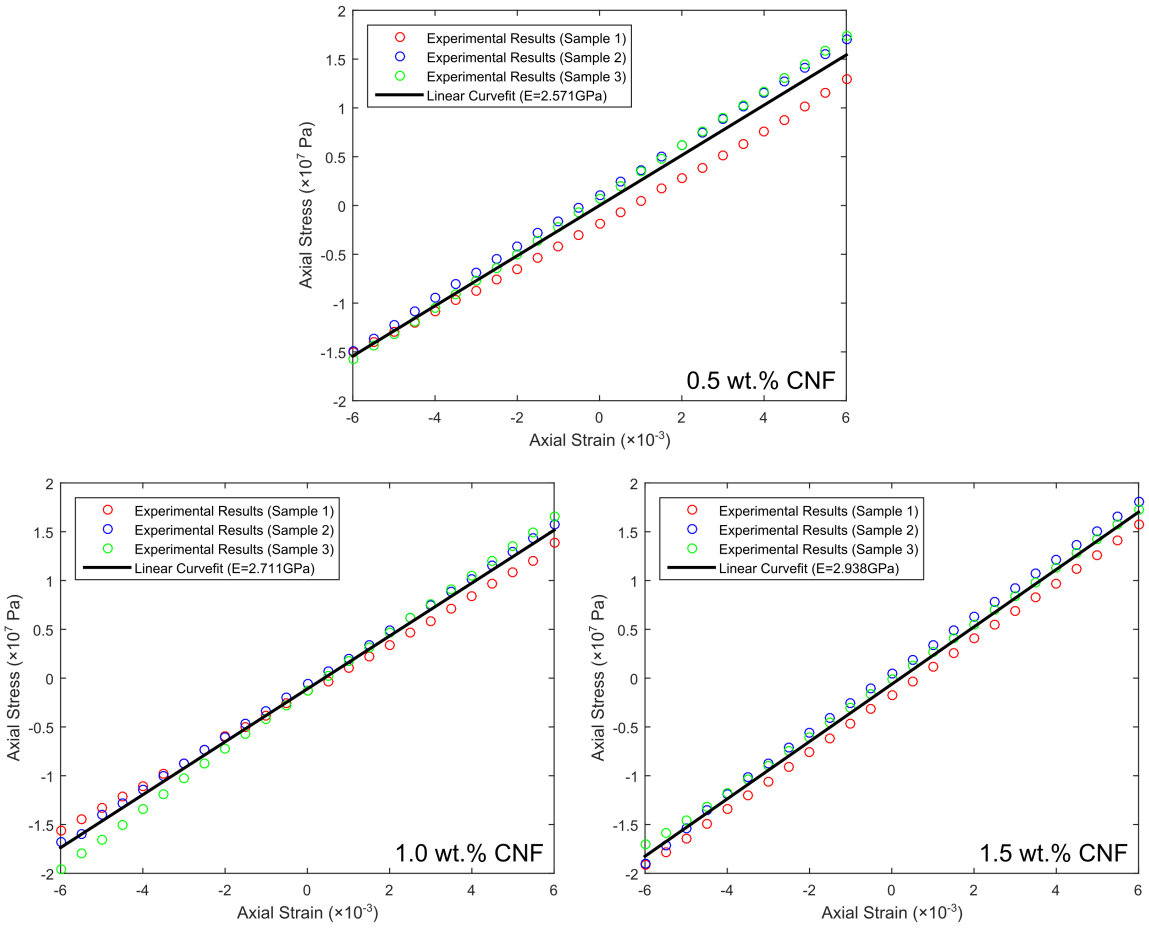

Fig. 4.8. Normal stress versus normal strain for all CNF/epoxy specimens.

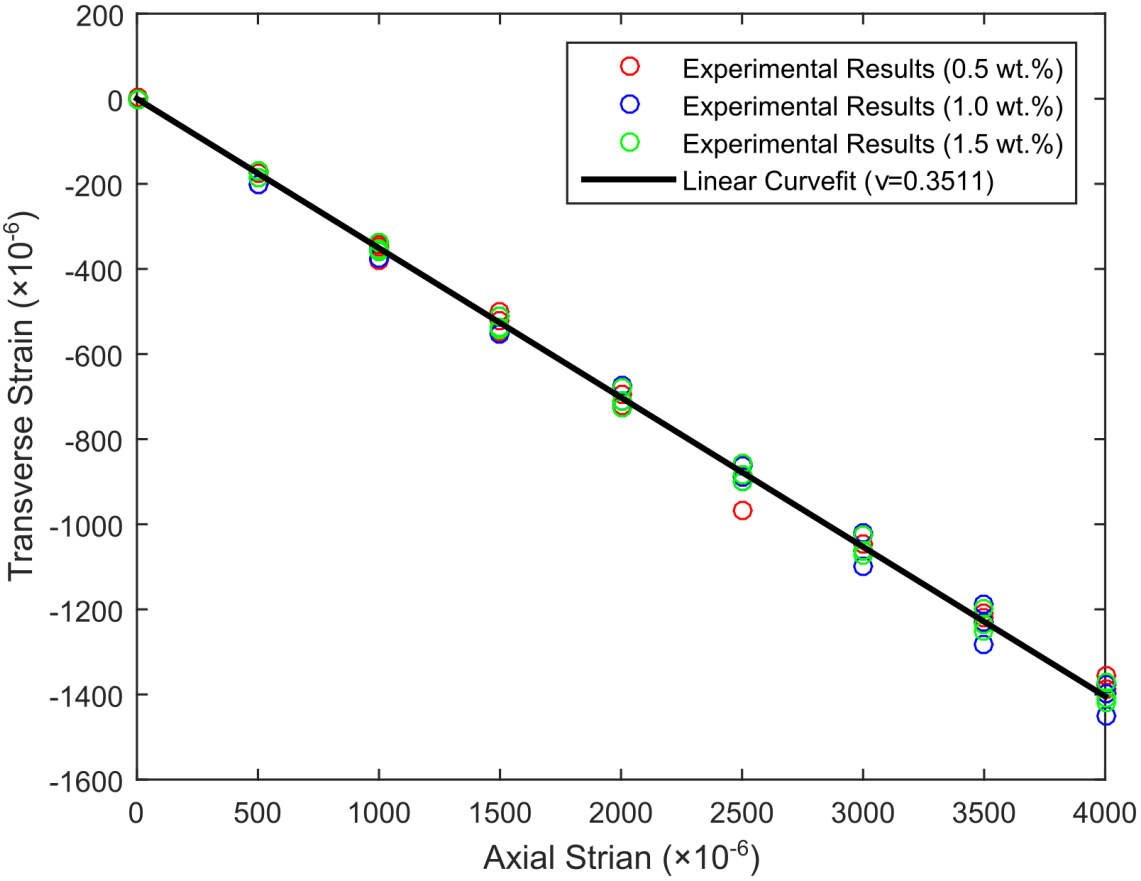

Fig. 4.9. Transverse strain versus axial strain for all CNF/epoxy specimens.

Table 4.1.
Mechanical properties of 0.5, 1.0, and 1.5% CNF/epoxy specimens

CNF wt.%	**E (GPa)**	ν (-)
0.5	2.571	0.3511
1.0	2.711	0.3511
1.5	2.938	0.3511

4.7 Summary and Conclusion

In order to test the previously described macroscale modeling methods, piezoresistive specimens were produced, instrumented, and DC and AC measurements were

taken as a function of normal and shear strain. Mechanical properties, modulus of elasticity and Poisson's ratio, were also measured. CNF-modified epoxy was used as a representative piezoresistive material in order to conform to previously described model assumptions.

Specifically, CNF/epoxy specimens were first manufactured at 0.5, 1.0, and 1.5 wt.% CNFs. Second, uniaxial tests were done according to ASTM D638. However, the gage lengths of specimens were shortened to decrease the likelihood of buckling during compressive testing. Third, v-notched rail shear testing was conducted based on ASTM D7078. This test was conducted to induce uniform shear strain in the test region such that DC and AC measurements could be collected as a function of shear. A four-point probe method was used to determine DC electrical resistance under axial and shear loading. Unlike resistivity measurements which are traditionally taken from a prismatic specimen, resistivity was not able to be directly measured in the load frame. This means that the simple resistivity equation for prismatic specimens cannot be used. For this, an in-house steady-state diffusion finite element simulation subject to CEM boundary conditions was developed in order to determine deformation-induced resistivity changes by equating model-predicted resistance changes to experimentally measured resistance changes. Deformation was also accounted for this model matching process. Fourth, AC electrical measurement methods and general descriptions of AC electrical properties were provided. Along with electrical measurements via DC and AC, mechanical properties of CNF/epoxy, such as elastic modulus and Poisson's ratio, were identified.

Several conclusions can be drawn from the work presented in this chapter. First, an exponential trend between DC resistivity and CNF weight fraction was observed as expected for materials that depend on percolation for electrical transport. Second, due to fixture geometry of v-notched rail shear test, it is impossible to induce negative shear strains. However, prior computational micromodeling has shown that the piezoresistive effect is independent of the sign of shear strain [104]. Therefore, the experimentally determined resistivity-change-versus-shear-strain data will be re-

flected across the zero-strain axis for the purposes of fitting equation (3.11). This will be detailed further later. Third, the effective AC conductivity measured in this chapter shows the same trend as AC conductivity measurements for the prismatic specimens. This suggests that the behavior of AC conductivity can be characterized by the UDR framework proposed earlier. And fourth, it was observed that elastic modulus increases slightly with increasing CNF weight fraction. Poisson's ratio, on the other hand, did not vary with CNF content. Elastic modulus was not necessary for the proposed tensorial relation but it is a guideline that confirms the test specimens are in the linear-elastic region. However, Poisson's ratio is needed in the proposed tensorial relation.

5. EXPERIMENTAL RESULTS AND ANALYSIS

5.1 Introduction

Having described the experimental methods, electrical properties, and mechanical properties, the experimental results and their resulting analyses are next presented. Specifically, this chapter will experimentally validate an important assumption of the proposed resistivity-strain tensorial relation, discuss how the piezoresistive constants were determined, experimentally validate the accuracy of the tensorial resistivity-strain relation for two cases of complex deformations, and explore how UDR fitting constants evolve with strain. Additionally, this chapter will describe the piezoresistive switching behavior (i.e. switching from positive piezoresistivity at low frequencies to negative piezoresistivity at high frequencies) that was observed during AC piezoresistivity testing. This discussion is accompanied by a microscale modeling in order to elucidate the physical mechanism of this switching behavior.

5.2 Experimental Validation of Assumptions for Tensorial Resistivity-Strain Relation

While deriving the proposed tensorial piezoresistive relations, three assumptions were made: i) Materials are limited to infinitesimal strain. ii) Materials exhibit isotropic resistivity changes such that the differences between resistivity measurements in all directions are negligible. And iii), resistivity changes are non-linear in strain. The first and third assumptions are straight-forward; we control the level of applied strain (and choose to keep it in the infinitesimal regime) and nanocomposites are well-documented to exhibit non-linear resistivity-strain relations. The validity of the second assumption, however, needs to be verified. To understand how the second

assumption could be violated, recall that materials with aligned conductive fillers are electrically anisotropic. Even though the manufacturing method herein employed does not purposefully seek to align the CNFs, the act of pouring the CNF-modified liquid epoxy into a mold will induce some in-plane alignment through flow mechanics. Therefore, two simple laboratory tests were performed to validate the second assumption. First, two 1.5 wt.% CNF/epoxy rectangular plates measuring 100 mm $\times$ 100 mm $\times$ 13 mm were manufactured with the same procedure described in Chapter 4 as shown in Figure 5.1(c). Next, these rectangular plates were cut into 36 pieces as shown in Figure 5.1(d). The resistivity of each cuboid was then measured in each direction. That is, resistivity was measured in the x_1-, x_2-, and x_3-directions for each cuboid (note that x_3 is the out-of-plane direction in the figure). The resistivity for each direction is shown in Figure 5.1(a) and (b). Resistivity measurements in all three directions are reasonably consistent for all 36 pieces, but there exists some mild electrical anisotropy. Resistivity measurements in the in-plane directions, x_1- and x_2-directions, have slightly lesser resistivity than the out-of-plane or x_3-direction. This is consistent with the fillers being mildly aligned in-plane due to flow during casting.

Despite the mildly anisotropic resistivity, it is important to recall that the focus of this modeling effort is on the *change* in resistivity (i.e. $\Delta\rho$) rather than the absolute value of resistivity (i.e. ρ). Hence, a second test is conducted to explore whether or not resistivity changes are isotropic. For this, two 1.5 wt.% CNF/epoxy dog-bone specimens were manufactured as previously described with the exception of being made thicker in the out-of-plane direction. To clarify, the dog-bone specimens have a gage section width of 13 mm, and the dog bones made for this validation were produced with an out-of-plane thickness of 13 mm. This was done so that resistance measurements taken in the flow direction (i.e. the x_1-direction) and the pouring direction (i.e. the x_3-direction) could be directly compared without accounting for different specimen dimensions. If the material exhibits isotropic resistivity changes, measurements of resistance change per undeformed resistance in these two directions should be the same as a function of strain. These results are shown in

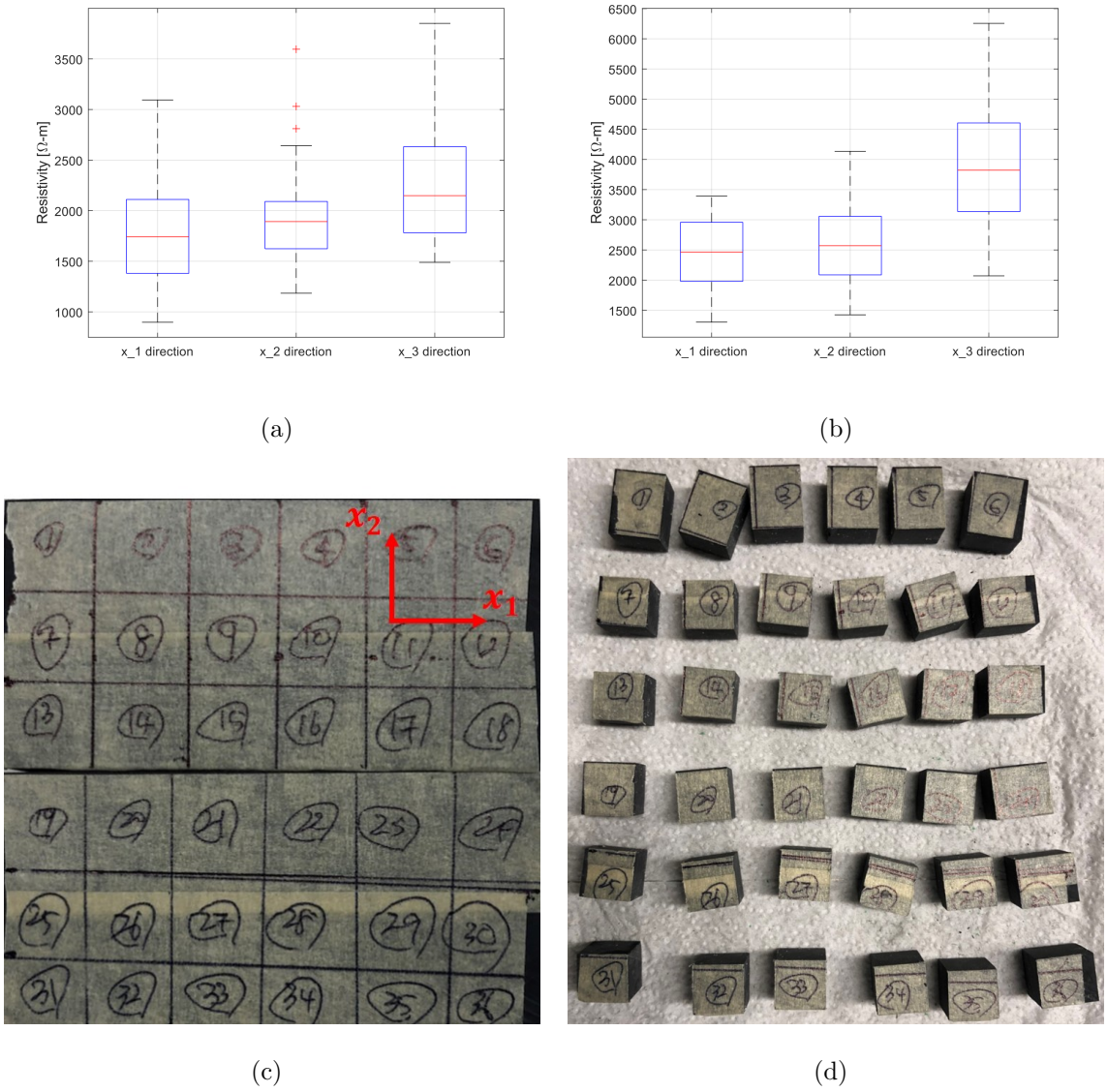

Fig. 5.1. (a) and (b) Resistivity distribution in three orthogonal direction for two samples (1.5wt.% CNF/epoxy). (c) Representative image of thick plate specimen. (d) Representative image of 36 cut specimen for three orthogonal resistivity measurements. As shown on the top right corner of (c), x_1 and x_2 are in-plane and x_3 is the through-thickness direction.

Figure 5.2(a). It can be observed that normalized resistance change is very consistent over two samples and in all directions. This indicates that the resistivity changes of CNF/epoxy nanocomposites are sufficiently similar to be considered as being isotropic

and the second assumption is validated. Interestingly, this assumption is also validated by computational micromodeling work conducted by Garcia-Macias *et al.* [104]. In this work, they manufactured and computationally analyzed the microstructure of MWCNT-reinforced cementious composites by investigating the directional dependence of resistivity changes. They also found that the difference between resistivity changes in longitudinal and transverse direction are negligible as shown in Figure 5.3.

5.3 Determination of DC Piezoresistive Constants

Next, the process by which piezoresistive constants of the higher-order tensorial piezoresistive relation are determined for each CNF weight fraction is described. In short, this is done by fitting equation (3.10) to resistivity change versus tensile strain data and fitting equation (3.11) to resistivity change versus shear strain data. Procedurally, equation (3.11) was fit first because it contains only one unknown parameter, Π_2. After this, equation (3.10) was fit to experimental data by treating $\kappa(1-2\nu)$ as one variable (say, A) and $(\Pi_1+\Pi_2-4\Pi_1\nu+(3\Pi_1+\Pi_2)\nu^2)$ as another variable (say, B). Equation (3.10) is then fit to experimental data to find A and B. From this, κ is recovered from A by knowing the Poisson's ratio of the material, and Π_1 is recovered from B by knowing the Poisson's ratio and Π_2. Fitting was done using the *'cftool'* command in Matlab with the least absolute residuals (LAR) option. This option was used to diminish the effect of outlier data. The results of this fitting process can be seen in Figure 5.4, and the constants are tabulated in Table 5.1. Recall also that negative shear strains cannot be induced because of the v-notched rail shear fixture being unable to reverse direction. As shown in Figure 4.4, 'pushing down' on the fixture would cause it to contact itself. However, as described previously, resistivity changes due to shear strains are independent of shear sign. Therefore, shear data was reflected across the zero-shear axis for fitting.

Several interesting observations can be made from the results presented in Figure 5.4. First, the proposed higher-order tensorial piezoresistive relation fits the

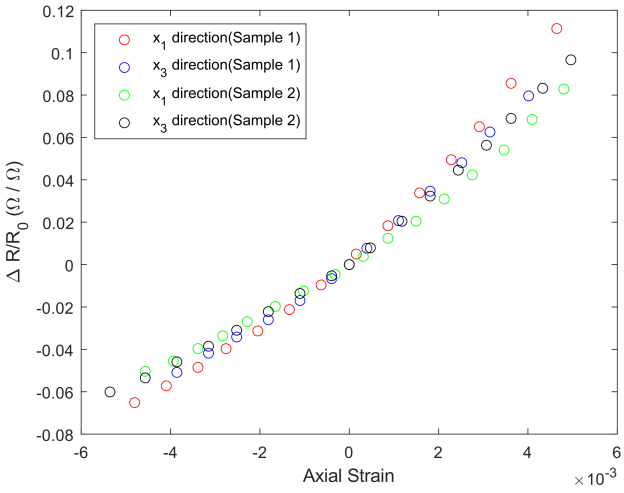

(a)

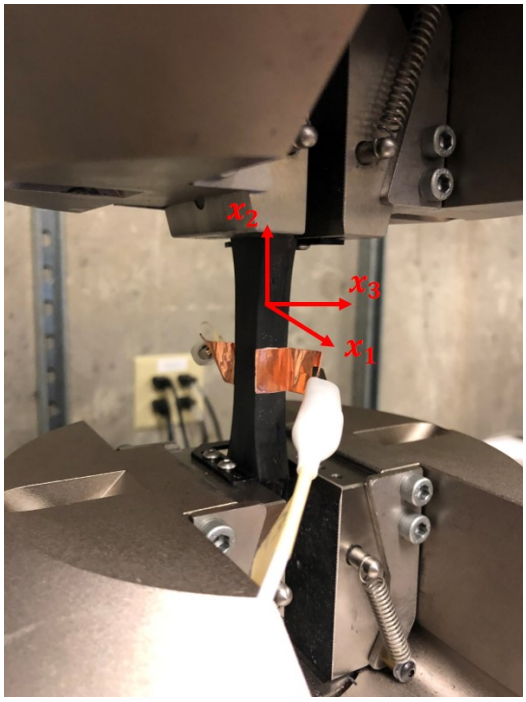

(b)

Fig. 5.2. (a) Normalized resistance change 1.5wt.% CNF/epoxy specimens with respect to applied strain in two samples. It is shown that the change in resistance are independent of measurement directions. (b) Representative measurements in in-plane direction.

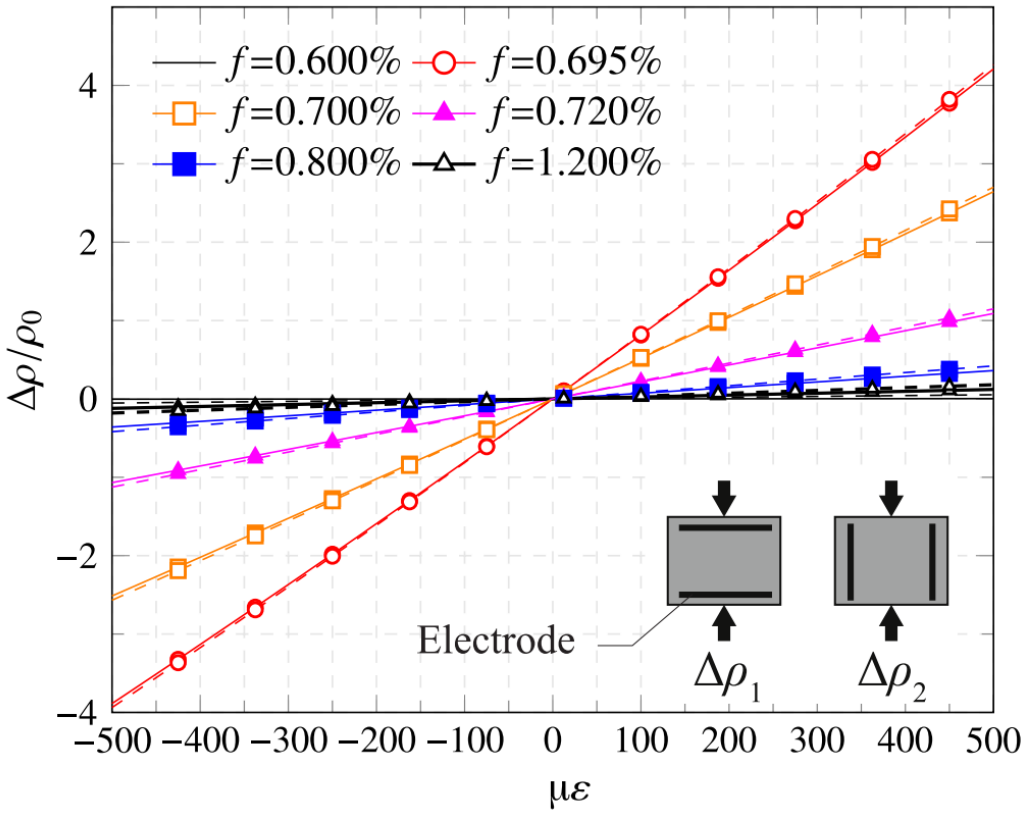

Fig. 5.3. Normalized resistivity change of MWCNT-reinforced cement with respect to different filler concentrations under laterally constrained uni-axial dilation [104]. Note that solid and dashed lines denote longitudinal ($\Delta\rho_1/\rho_0$) and transverse ($\Delta\rho_2/\rho_0 = \Delta\rho_3/\rho_0$) relative changes in resistivity, respectively.

experimental data well. Second, the fitting parameters, or piezoresistive constants, shown in Table 5.1 decrease in magnitude with the increase in CNF weight fraction. This is perhaps to be expected because it is well-known that lower weight fraction nanocomposites have higher sensitivity. Third, it is important to note that Π_1 values are all negative. Because this may seem like a counter-intuitive result, it needs to be reiterated that the general form of the proposed higher-order was selected simply based on the expectation that the piezoresistive response is non-linear and therefore requires higher-order strain products. In other words, there is no physical expectation that the fitting parameters are positive. And fourth, it may be expected that resis-

tance decreases between the measurement electrodes during tension because applied tension causes the electrodes to move closer due to the Poisson effect. However, this is an incomplete rationale. That is, if the material-level resistivity is independent of strain, the reduced inter-electrode distance would indeed cause the inter-electrode resistance to decrease. However, the applied tension also changes the connectedness of the underlying nanofiller network. This latter effect dominates the overall resistance change. This behavior also can be observed in Figure 5.2 where resistance increases in x_3 direction with increasing tension although the distance between the electrodes decreases due to Poisson's effect. Therefore, an increase in resistance with increasing tension (or, conversely, a decrease in resistance with increasing compression) is experimentally observed. Furthermore, it is important to note that the finite element simulations used for converting resistance measurements to resistivity changes (as described in Chapter 4) do also intrinsically account for geometric effects due to deformation.

Table 5.1.
Piezoresistive constants of CNF/epoxy as determined by fitting process. Note that all constants have units of resistivity, Ω-m.

CNF wt.%	$\boldsymbol{\kappa}$	$\boldsymbol{\Pi_1}$	$\boldsymbol{\Pi_2}$
0.5	8.08×10^9	-7.15×10^{11}	2.25×10^{10}
1.0	4.10×10^6	-1.5×10^8	5.15×10^6
1.5	6.22×10^5	-7.13×10^7	4.33×10^5

5.4 Experimental Validation of DC Piezoresistivity Model

Next, the predictive power of the proposed higher-order tensor-based piezoresistivity relation is validated for complex states of strain. This is done in two ways. First, discrete resistance measurements are taken from a complex shape as it is deformed.

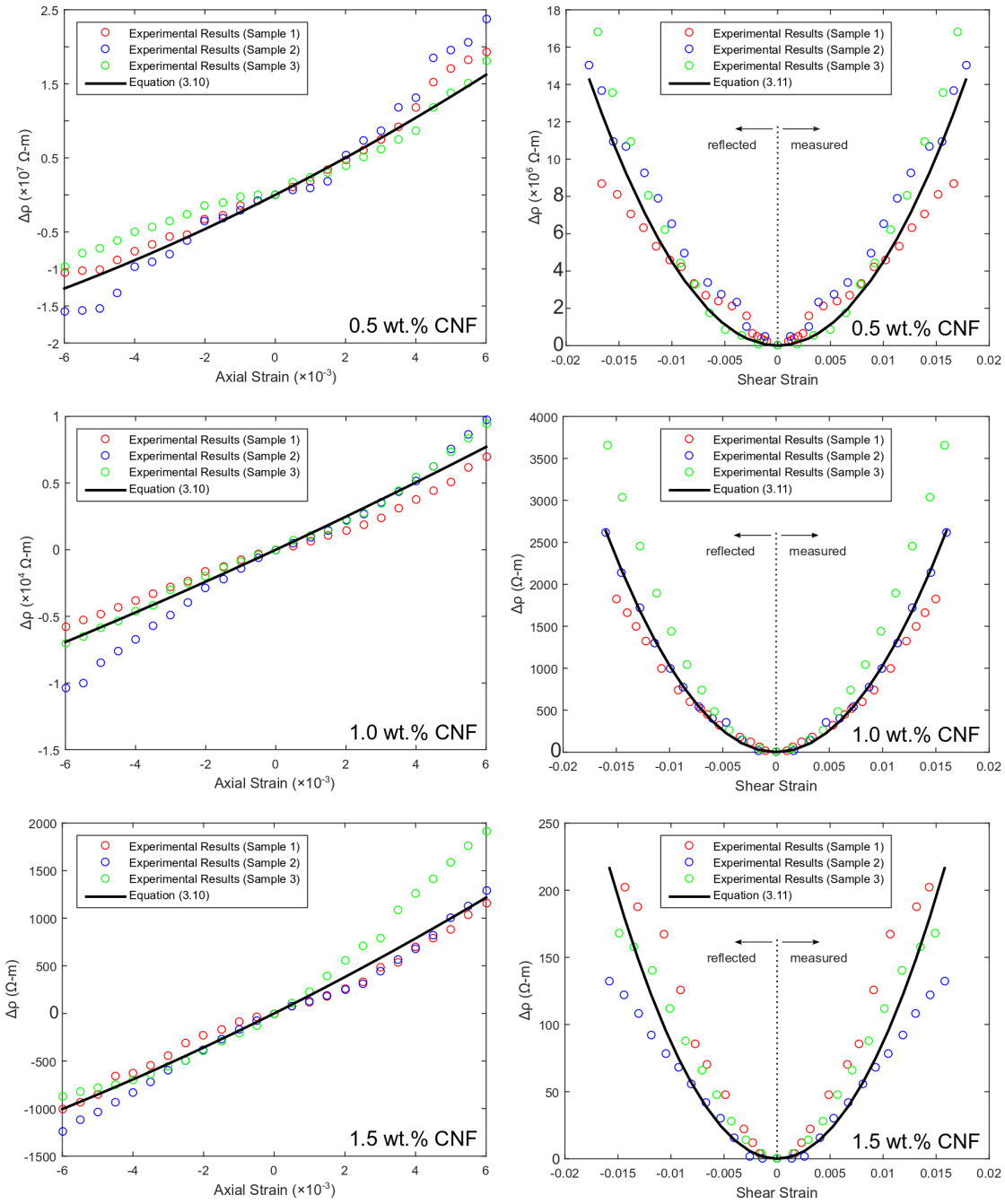

Fig. 5.4. Fitting of reduced piezoresistive relations to experimental data. Left column: fitting to tensile data. Right column: fitting to shear data.

And second, experimental EIT is used to image the spatially varying deformation-induced resistivity change of a plate with a hole.

5.4.1 Comparison of Model Prediction to Discrete Resistance Measurements on a Complex Shape

Three S-shaped specimens were manufactured as described in Chapter 4 with three different weight fractions of CNFs – 0.5, 1.0, and 1.5 wt.%. S-shaped silicone molds were produced as described in Chapter 4 and CNF-modified epoxy was cast into the molds. A representative S-shaped specimen with electrodes and insulating grips attached is shown in the top left corner of Figure 5.5. The gage section of the S-shaped specimens measured 13 cm in length from top-to-bottom, the width of the S-shaped portion was 10 mm, and as-molded thickness was 4.5 mm. These specimens were subject to applied displacements ranging from -1.5 mm to 1.5 mm in an Instron 8801 load frame while inter-electrode voltages were measured such that resistance changes could be calculated for a prescribed current injection. The experimentally measured resistance changes with respect to applied displacements are shown in Figure 5.5. This test was also replicated computationally using the finite element method. Specifically, an elasticity simulation (making use of the previously determined modulus of elasticity and Poisson's ratio for each CNF weight fraction) was used to replicate the deformation of the S-shaped specimens. Resistivity changes were then ascribed to the model element-wise based on the proposed higher-order resistivity-strain relation and utilizing the piezoresistive constants in Table 5.1. To compute resistance changes, steady-state diffusion finite element simulations with CEM boundary conditions were again used to predict the voltage-current relationship for each state of deformation. The simulated resistance changes are shown in Figure 5.5. Model predictions match experimental observations well.

The resistivity changes computed by the tensorial relation are shown in Figure 5.6 for displacements of ± 0.5 mm and ± 1.5 mm. Note that resistivity is treated as element-wise constant in these simulations. Therefore, triangulation effects in Figure 5.6 are expected. Several interesting observations can be made from Figure 5.6. First, the highest magnitude changes in resistivity appear at either the inner or outer

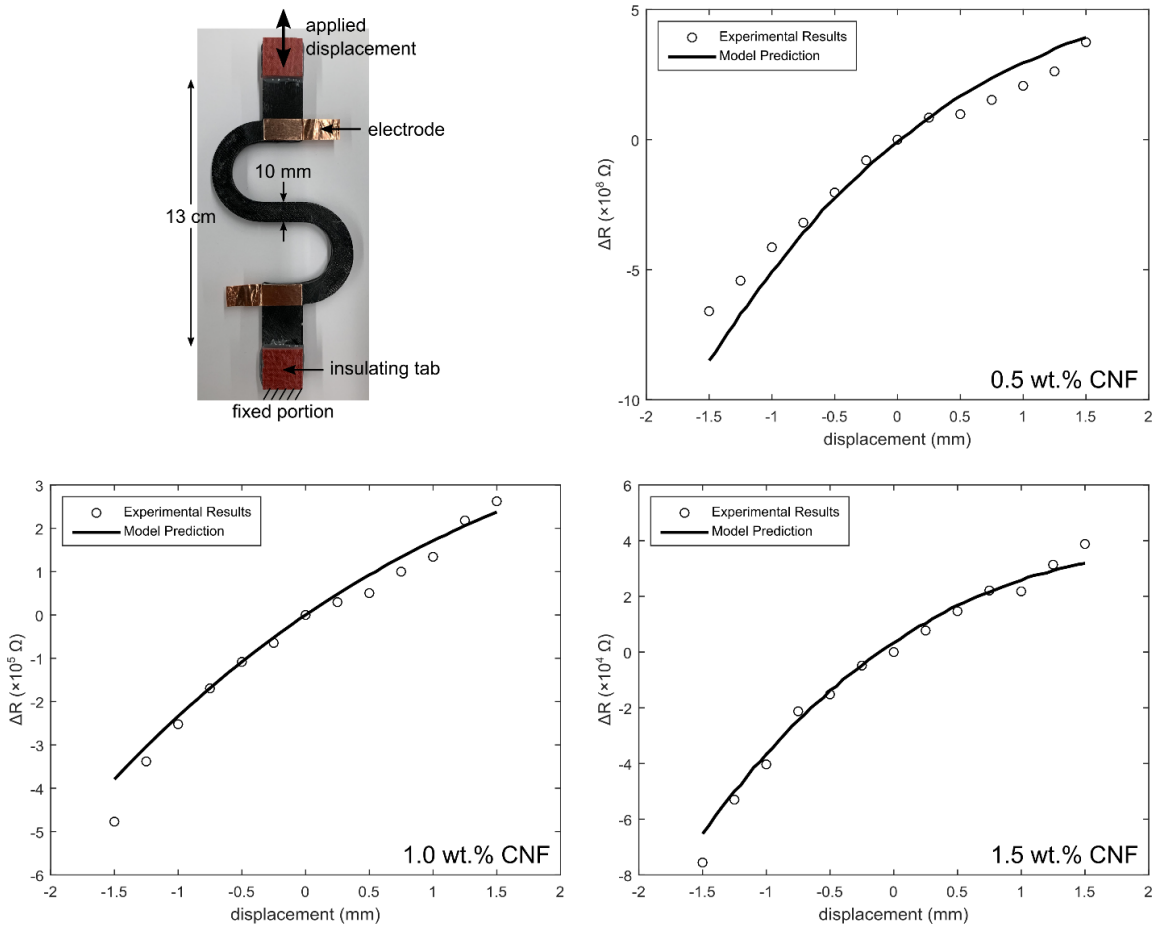

Fig. 5.5. Experimental validation by discrete resistance measurements on a complex shape. The S-shaped specimens were deformed upward and downward in a load frame as resistance measurements were taken between electrodes. Good model-to-experiment agreement is observed.

edges of the curved areas of the S-shaped specimens. This is expected results because applied upward or downward displacements will cause the highest strain at these edges. Second, the sign of the predicted resistivity changes correspond to the sign of the strain. That is, for example, the image in the top-right corner of Figure 5.6 (i.e. 1.5 mm displacements at 0.5 wt.%) shows a resistivity decrease at the outer edge of the curve corresponding to a state of compression and an increase in resistivity at

the inner edge which corresponds to a state of tension. And third, the magnitude in the resistivity change for a given displacement is highest for 0.5 wt.% CNF/epoxy. This again agrees with the expectation that lower weight fractions exhibit higher sensitivity.

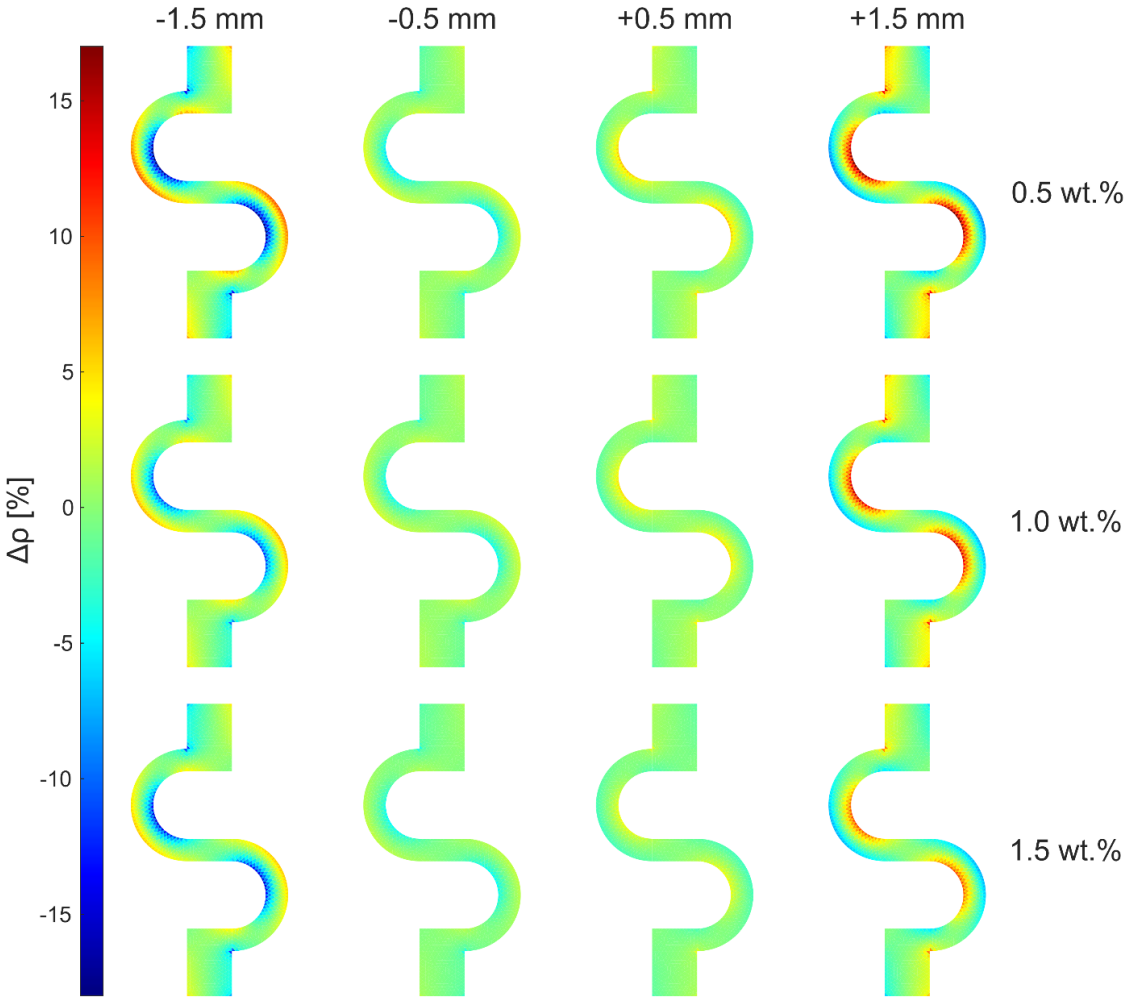

Fig. 5.6. Model-predicted resistivity changes for S-shaped specimens as a function of displacement. These resistivity changes were used to predict the voltage-current relationship between electrodes as a function of displacement.

5.4.2 Comparison of Model Predictions to Experimental EIT-Imaged Resistivity Changes

Next, the model's predictive power for distributed resistivity changes is experimentally validated against EIT-imaged resistivity changes. For this, a 1.0 wt.%. CNF/epoxy thin plate measuring 82 mm $\times$ 46.5 mm with a hole of diameter 12.7 mm in its center was put in tension as shown in the left of Figure 5.7. The bottom of the specimen was completely fixed in all directions and a laterally-constrained upward displacement of 0.25 mm was applied on the top edge of the specimen. Treating this as a plane-stress problem with mechanical properties of 1.0 wt.% CNF/epoxy specimen in Table 4.1, an in-house finite element simulation with linear tetrahedral elements was used to calculate the displacement field and strains. Then, with the experimentally determined piezoresistive constants shown in Table 5.1 and the higher-order tensorial relation, the element-wise resistivity change distribution was calculated. The model-predicted resistivity changes are shown in the left of Figure 5.8. Note that resistivity is again treated as being element-wise constant and triangulation effects in Figure 5.8 are expected.

These model-predicted results are then compared to experimental EIT-imaged resistivity changes for the same strain state. The right of Figure 5.7 shows the specimen used for this test. This specimen measured 196 mm $\times$ 46.5 mm with a 4 mm thickness. The gage section measured 82 mm $\times$ 46.5 mm, the same as the simulated domain. This test specimen was manufactured with 1.0 wt.% CNFs using the procedure described previously. The specimen was loaded to 0.25 mm in positive tension by displacement-controlled settings in an Instron 8801 load frame. The grips on the top and bottom of the load frame and the applied tensile displacement replicate the model boundary conditions and loading conditions. Additional details of the experimental setup are described in [128].

The resistivity change due to this state of deformation was then imaged via EIT. Although an exhaustive description of EIT exceeds the scope of this thesis, a brief

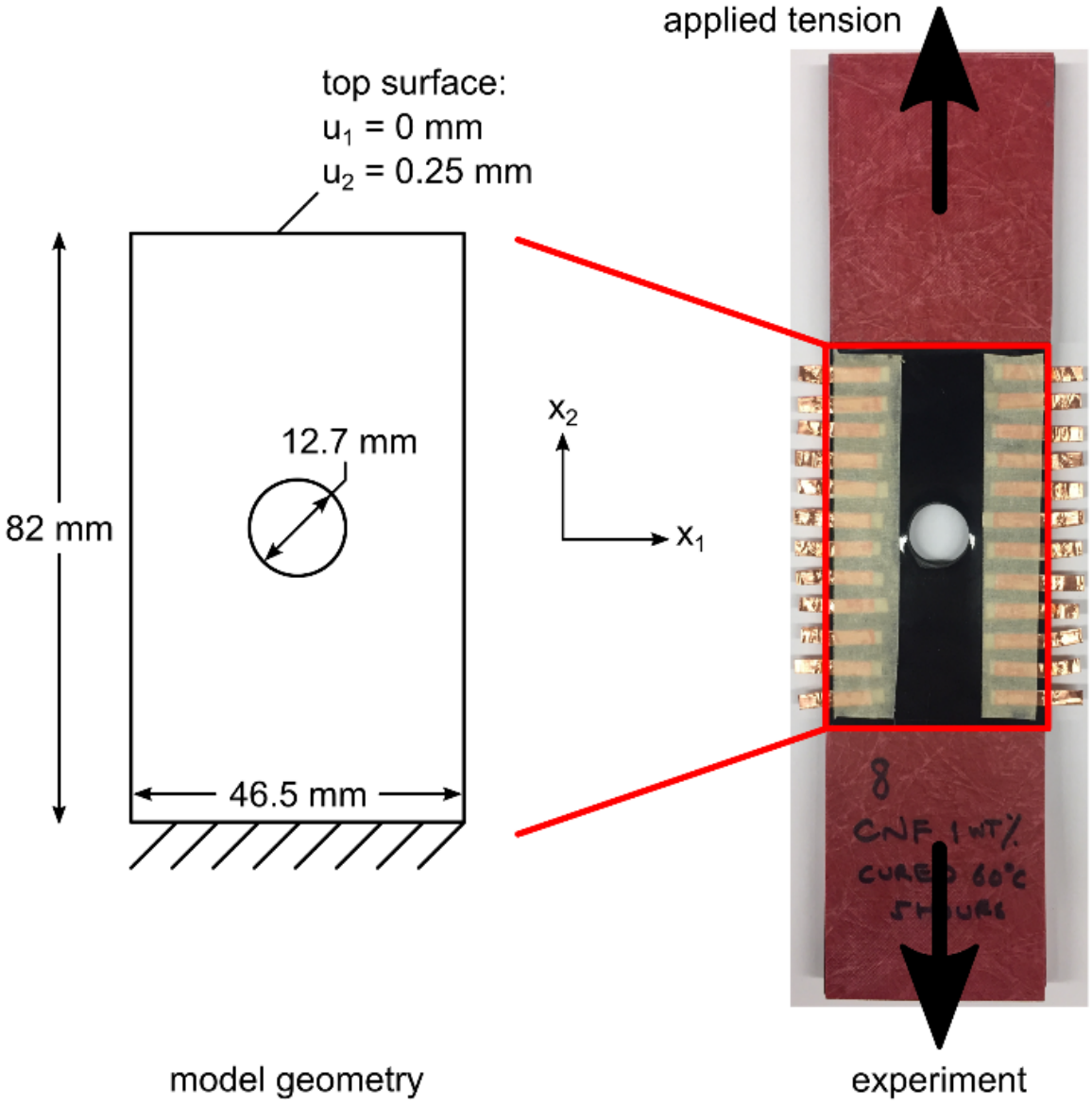

Fig. 5.7. Left: geometry of finite element model with boundary conditions. Right: 1.0 wt.% CNF/epoxy specimen used for experimental validation. Note that the gauge section dimensions match the model dimensions. Strips of copper tape are EIT electrodes.

summary is provided. In short, EIT images the internal resistivity distribution of a domain based on voltage-current relations observed at the domain's boundary. This takes the form of a model-update problem wherein the resistivity distribution of a

model (typically a finite element model with CEM boundary conditions) is updated until the model-predicted voltage-current relationship at the boundary matches the experimentally observed voltage-current relationship at the boundary. This is mathematically formulated as a minimization problem as shown below with an explicit solution for the resistivity change shown next.

$$\rho^* = \arg\min_{\rho} ||\mathbf{F}(\rho) - \mathbf{V}||_2^2 + \alpha||\mathbf{R}(\rho)||_2^2 \tag{5.1}$$

$$\Delta\rho = \left(\mathbf{J}^T\mathbf{J} + \alpha^2\mathbf{R}^T\mathbf{R}\right)^{-1}\mathbf{J}^T\left(\mathbf{F}(\rho_0) - \mathbf{V}\right) \tag{5.2}$$

In the preceding equations, $\mathbf{F}(\rho)$ is a vector of model-predicted boundary voltages for a prescribed current injection, $\mathbf{V}$ is a vector of experimental measurements, ρ^* is a resistivity distribution that satisfies the minimization, ρ_0 is an estimate of the resistivity distribution, and $\mathbf{J} = \partial\mathbf{F}(\rho)/\partial\rho$ is known as the sensitivity matrix. Note also that a regularization term, $\mathbf{R}(\rho)$, has been added to the minimization. This is needed because EIT is a fundamentally ill-posed inverse problem which requires some *a priori* knowledge to achieve a physically meaningful solution. Herein, the discrete Laplace operator (formed by the finite difference method) is used for regularization. This particular regularization is used because it is known to promote spatially smooth solutions. Because resistivity changes are strain-driven and the strain field for this problem is smoothly varying, it is likewise expected that the resistivity distribution will be smoothly varying. α is a scalar hyper-parameter which controls the extent of regularization. For a more fundamental discussion of EIT including minimization techniques, least-squares formulations, and the effect of minimization and regularization norms, interested readers are directed to [129–132]. The EIT-imaged resistivity change distribution in the gauge section is shown in the middle of Figure 5.8.

Several noteworthy observations can be made regarding Figure 5.8. First, a noticeable resistivity increase at the left and right edge of the hole and a pronounced decrease at the top and bottom edge of the hole can be observed. These are due to the well-known strain concentrations for a plate with a hole subject to tension – a tensile

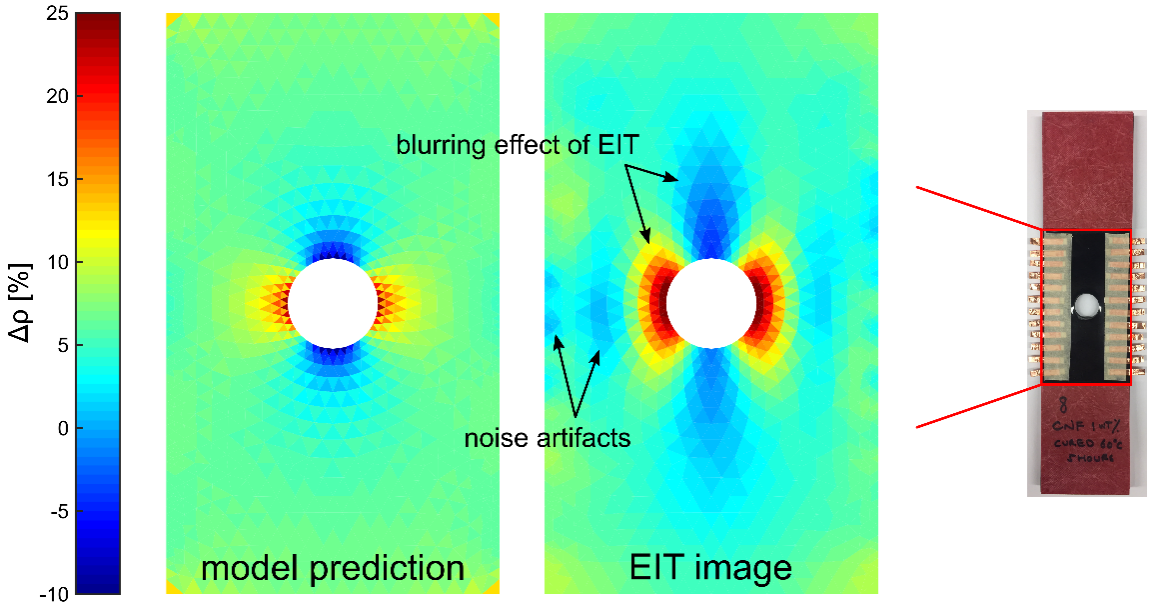

Fig. 5.8. Left: model-predicted resistivity changes for a plate in tension with a hole. Note the large resistivity changes which collocate with strain concentrations. Right: EIT-predicted resistivity change distribution. Despite the EIT-predicted resistivity changes being 'smeared' over larger areas than the model-predicted changes and the presence of noise artifacts in the EIT image, good model-to-experiment agreement is observed.

strain concentration exists at the left and right edge of the hole and a compressive concentration is present at the top and bottom edge of the hole. As shown in Figure 5.4, tensile strain increases resistivity and compression decreases resistivity. The resistivity distribution obtained from this work validates that tensile strain is present at the left and right edge of the hole and compressive strain is present at the top and bottom edge of the hole. Second, the model-predicted resistivity changes agree with the EIT-imaged resistivity changes well in terms of magnitude. Third, the EIT-imaged resistivity changes near the hole are seemingly 'smeared' over a larger area (i.e. are blurry) compared to the tensor-based piezoresistive relation-predicted resistivity changes. This is a consequence of a well-known limitation of EIT. EIT is a diffusive

imaging modality in which electrical current follows a path of least resistance through the material as opposed to straight lines as in radiography. As a result, EIT images tend to be blurry. And fourth, the model-predicted resistivity changes away from the hole are slightly greater than those of the EIT image. This may be a consequence of three factors. i) Experimental EIT necessarily includes noise which causes the background resistivity to vary. Indeed, there are non-negligible fluctuations away from the hole. ii) EIT tends to be less adept at imaging domain-spanning resistivity changes (i.e. global resistivity changes away from the hole) and better at imaging localized artifacts (i.e. concentrations near the hole). And iii), it is well known that considerable specimen-to-specimen variability exists for piezoresistive nanocomposites. Such variability is even evident in our tensile and shear testing shown in Figure 5.4. Therefore, the modest deviations observed between the tensorial relation-predicted and EIT-imaged resistivity change distributions in Figure 5.8 seem reasonable.

5.5 Model Limitations

Like all models, the one herein proposed has limitations (beyond conditions that violate the previously described assumptions). It is therefore important to be cognizant these limitations. A limitation of particular importance is concerned with the fitting process used to determine piezoresistive constants. That is, the determination of piezoresistive constants is essentially a polynomial fit in strain. Polynomial fits can provide good predictions in the range over which they are fit, but there is no guarantee of accuracy if this range is exceeded. This limitation is graphically illustrated in Figure 5.9. That is, the model is reliable within the strain range where the data was fit. However, outside of that range, accuracy is not assured. The model *may* still be accurate just outside of the fitting region because it predicts a 'hardening' effect in tension and a 'softening' effect in compression (which is generally observed in piezoresistive materials loaded in tension [92]). However, in the far-left region,

the model predicts increasing resistivity with increasing compression which is not physically expected.

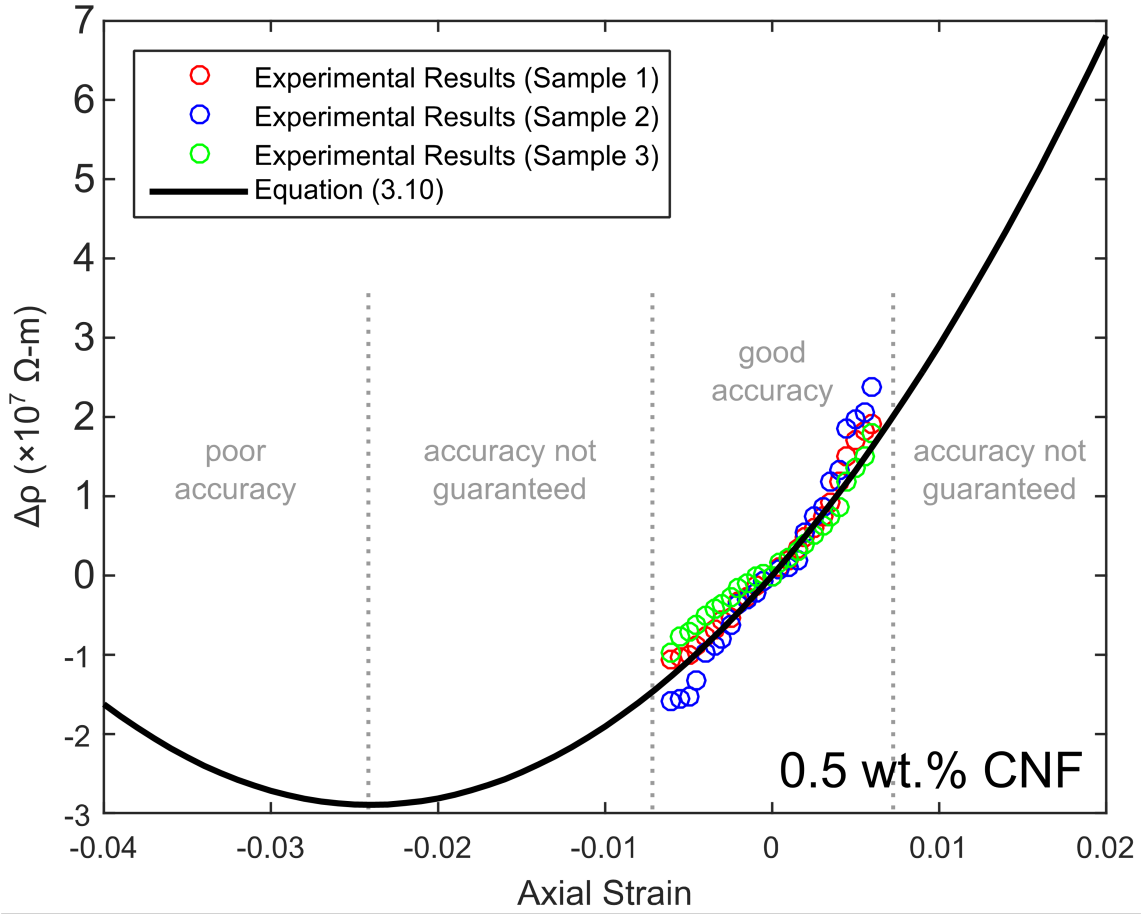

Fig. 5.9. Illustration of model accuracy in terms of strain range. As shown in general polynomial fits, the model is trustworthy within the fitted strain range but gives poor predictions far outside of this range.

5.6 Effective AC conductivity

5.6.1 Raw Impedance and Phase Data

Recall from Chapter 4 that impedance magnitude, $|Z|$, and phase angle, θ, were measured in terms of frequency as dog-bone and v-notched specimens were deformed under normal and shear loading, respectively. Before discussing the effect of deformation on AC conductivity, the raw measured impedance magnitude and phase angle data as directly reported by the impedance analyzer are presented. Although three specimens per each weight fraction have been tested, only one representative result is shown in the main body of this thesis per each weight fraction and test (i.e. uniaxial and shear test) in Figures 5.10 and 5.11. This is because all specimens for each weight fraction and test showed the same response and trend. The rest of the plots of the raw impedance magnitude and phase angle data are included in Appendix B. A few important observations can be made regarding the data in Figures 5.10 and 5.11. First, much noise exists in the impedance magnitude and phase angle data at low frequencies for 0.5 wt.% CNF/epoxy. This has also been observed elsewhere in the state of the art and is attributed to poor AC percolation at low weight fractions [122] [127]. On the other hand, impedance magnitude and phase angle data of 1.0 wt.% and 1.5 wt.% CNF/epoxy showed much less noise and clear trends. And second, as shown in Figures 5.10 and 5.11, 1.0 wt.% and 1.5 wt.% CNF/epoxy show consistent changes in impedance magnitude and phase angle due to applied normal and shear strain. This is noteworthy because it indicates that both impedance magnitude and phase angle can be utilized for strain sensing purposes.

5.6.2 Variation of Effective AC Conductivity with Applied Strain

Effective AC conductivity as a function of normal and shear strain is next presented in Figures 5.12 and 5.13, respectively. As with the raw impedance magnitude and phase angle data, only one representative result is shown per weight fraction and

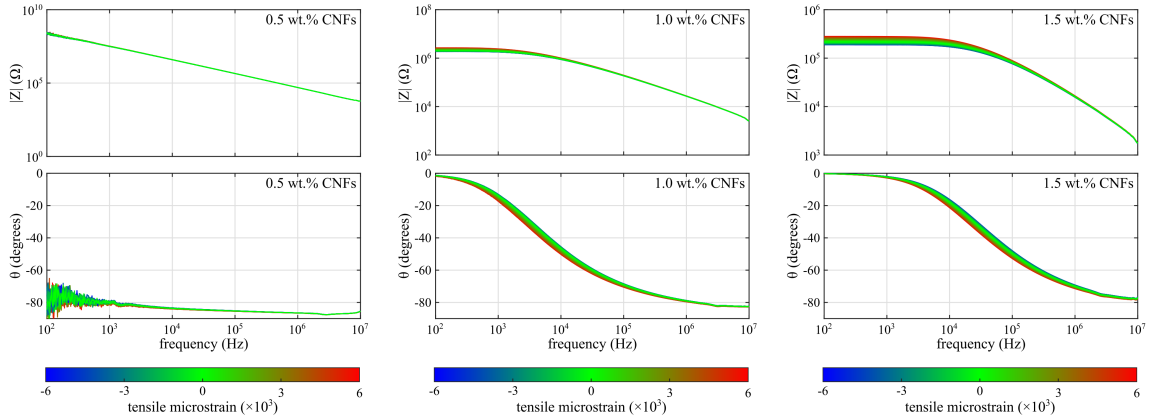

Fig. 5.10. Raw impedance magnitude and phase angle data for specimens under applied normal loading.

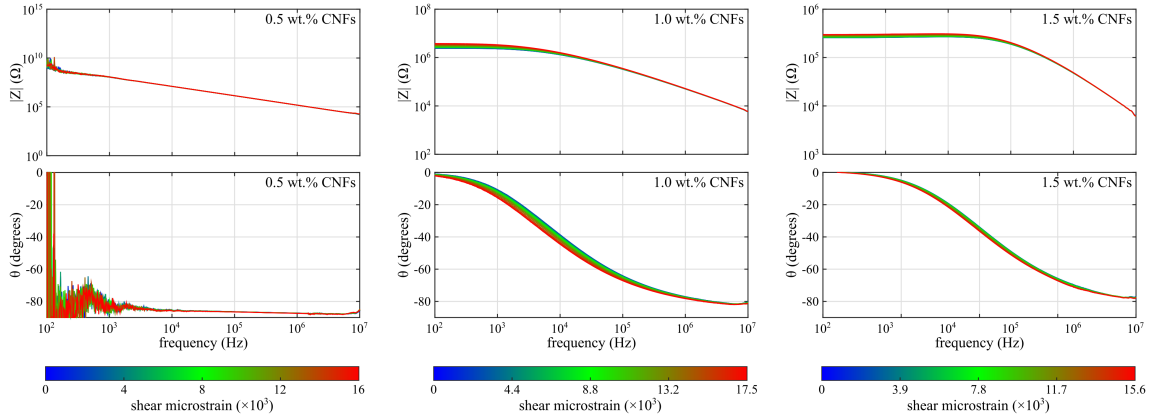

Fig. 5.11. Raw impedance magnitude and phase angle data for specimens under applied shear loading.

test. Again, all specimens showed the same trend. The rest of the experimentally measured effective AC conductivity is provided in Appendix C. Several observations can be made regarding Figures 5.12 and 5.13. First, as expected from the results of impedance magnitude and phase angle data, there exists much noise for 0.5 wt.% CNF/epoxy specimens at low frequencies. Second, the general shape of the effective

AC conductivity-versus-frequency curves are the same as AC conductivity measured from prismatic specimens. That is, the effective AC conductivity is initially constant and then exponentially increases with interrogation frequency. Third, the effective AC conductivity varies systematically with applied normal and shear strains.

An interesting piezoresistive switching behavior can also be observed and deserves special consideration. To clarify, in the low frequency range, a *positive* piezoresistive response can be seen. That is, the magnitude of the effective AC conductivity decreases with increasing tensile and shear strain. This is evident by the red curves (indicating high tensile and shear strain) being shifted downward and blue curves (indicating high compressive strain and low shear strain) being shifted upward. However, a *negative* piezoresistive response can be observed in the high frequency range. That is, the effective AC conductivity behaves opposite compared to the behavior at low frequencies – in the high frequency range, red curves are shifted upward and blue curves are shifted downward. In other words, the magnitude of the effective AC conductivity decreases with increasing compressive strain. Because of the switch from positive to negative piezoresistivity, there must also be a point of *zero* piezoresistivity (i.e. a frequency at which the deformed AC conductivity is equal to undeformed AC conductivity). To the best of the author's knowledge, this switching behavior has not been explored elsewhere. The current state of the art overwhelmingly reports positive DC piezoresistivity (although a few instances of negative DC piezoresistivity have been reported [133–135]). This is a novel observation because it implies that the sensing characteristics of the material can be modulated via frequency. The underlying physical mechanisms of this switching behavior are discussed later in section 5.6.4.

5.6.3 Evolution of Power-Law Fitting Parameters with Applied Strain

In light of the fact that the effective AC conductivity changes in response to strain, it is next desired to cast this relationship in terms of the previously discussed macroscale modeling framework. For this, the experimentally measured effective AC

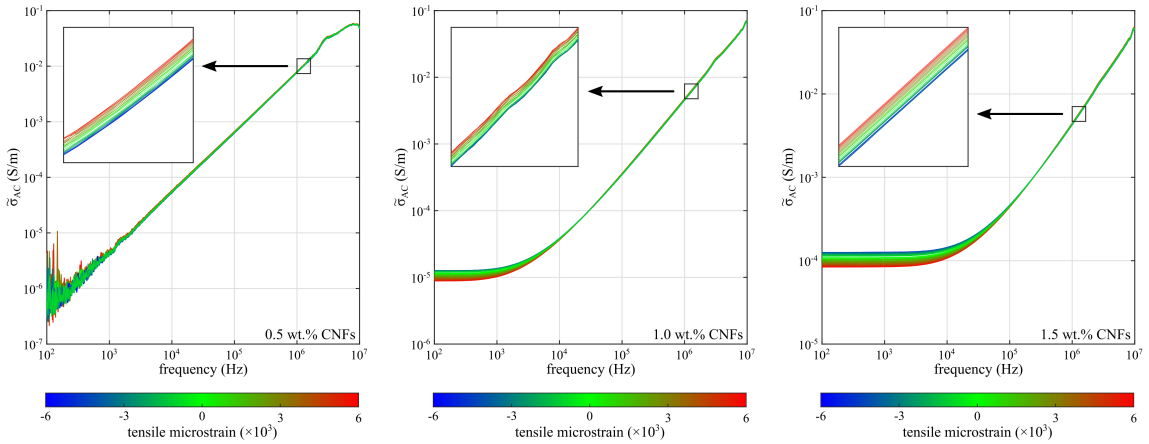

Fig. 5.12. Effective AC conductivity for specimens under applied normal loading. The inset figures show the effective AC conductivity in the range of 1 to 1.25 MHz. Note how the red curve is at the bottom at low frequencies but switches to being on top at high frequencies

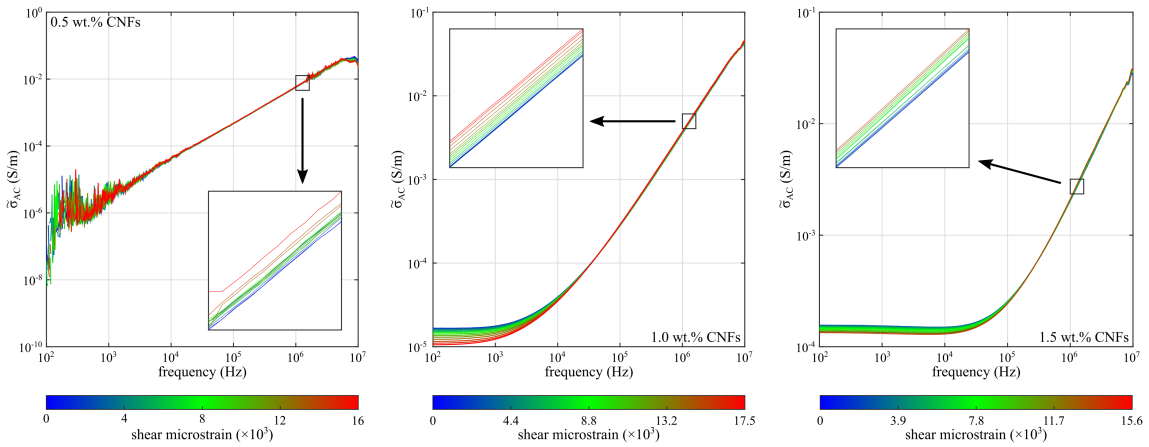

Fig. 5.13. Effective AC conductivity for specimens under applied shear loading. The inset figures show the effective AC conductivity in the range of 1 to 1.25 MHz. Again, switching behavior is seen between low and high frequencies.

conductivity is fit to a power law for the UDR as described by Jonscher [121]. The relationship between fitting constants and applied strain is found by fitting equa-

tion (3.12) to the experimentally measured effective AC conductivity data for each applied strain state. Curve fitting was again done using *'cftool'* in MATLAB. The LAR option was also again used to minimize the effect of outlier data. In order to confirm whether the proposed power law equation fit the experimental data well, representative curve fitting results for dog-bone and v-notched specimens are shown in Figure 5.14. It can be seen that equation (3.12) fits the experimental data quite well. In fact, the coefficient of determination, R^2, exceeded 0.98 for all cases thereby suggesting good fits.

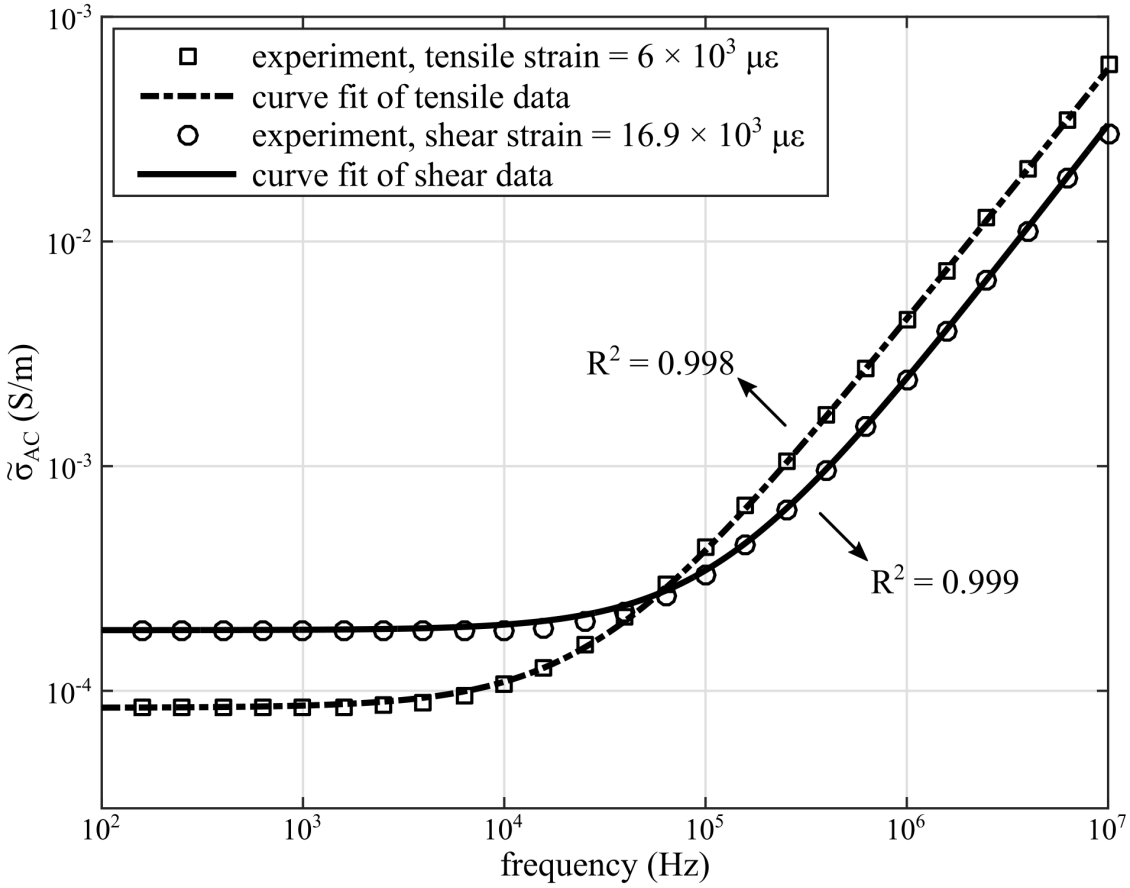

Fig. 5.14. Representative examples of fitting the UDR power law to experimental data in tension and shear. Very good correspondence between curve-fit and experimental results is achieved.

The undeformed effective DC conductivity, $\tilde{\sigma}^0_{DC}$, and undeformed fitting constants, K_0 and n_0 for dog-bone and v-notched specimens are presented in Table 5.2. Changes in the fitting parameters are shown in Figures 5.15 and 5.16 for normal and shear deformation, respectively. Note that $\tilde{\sigma}^0_{DC}$ data for 0.5 wt.% CNF/epoxy specimens is not presented in Table 5.2 nor Figures 5.15 and 5.16 because noise in the low frequency range severely degrades the quality of fitting procedure. Hence, for the fitting process of 0.5 wt.% CNF/epoxy, $\tilde{\sigma}_{DC}$ was dropped from both sides of equation (3.12) and fitting parameters K and n are found by $\sigma_{AC} = K\omega^n$ for frequencies greater than 1 kHz. That is, fitting is done only in the frequency-dependent part of the plot and flat-portion is dropped.

Several interesting observations can be made regarding Figures 5.15 and 5.16. First, changes in the fitting parameters are relatively consistent between specimens. To clarify, it is not claimed that the changes in fitting parameters are identical for each specimen. However, it is well-known that considerable specimen-to-specimen variability exists for piezoresistive nanocomposites even for a single manufacturing method. Instead, it is claimed that the *changes* in fitting parameters for each specimen show similar trends and are all in the same magnitude range. This is noteworthy because it indicates that changes in fitting parameters can be leveraged for characterizing AC piezoresistivity. Second, it appears that changes in fitting parameters due to strain are generally non-linear. Furthermore, there exist an appreciable difference between the effective DC conductivity in tension and compression. This non-linearity is also well-known due to the DC piezoresistive response in tension being greater than in compression. And third, the trends of $\Delta\tilde{\sigma}_{DC}$ and ΔK behave in the opposite fashion. That is, $\Delta\tilde{\sigma}_{DC}$ decreases with the increasing normal and shear strain but ΔK increases with the increasing normal and shear strain. This is noteworthy because these trends can help describe the switching behavior. $\tilde{\sigma}_{DC}$ in equation (3.12) controls the vertical location of the effective AC conductivity at low frequencies in Figures 5.15 and 5.16. On the other hand, K controls the vertical location of the effective AC conductivity at high frequencies. That is, if the specimens are under higher tensile and

Table 5.2.
Fitting constants for unstrained conductivity measurements. Note that the unstrained effective DC conductivity for 0.5 wt.% CNFs is omitted because low-frequency noise prevented a meaningful fit.

			$\tilde{\boldsymbol{\sigma}}^0_{DC}$ (S/m)	$\boldsymbol{K}_0$	$\boldsymbol{n}_0$
tensile testing	0.5 wt.%	specimen 1	-	3.01×10^{-9}	1.07
		specimen 2	-	2.69×10^{-9}	1.08
		specimen 3	-	2.78×10^{-9}	1.08
	1.0 wt.%	specimen 1	1.15×10^{-5}	8.81×10^{-10}	1.12
		specimen 2	1.09×10^{-5}	8.89×10^{-10}	1.12
		specimen 3	2.39×10^{-5}	2.23×10^{-10}	1.17
	1.5 wt.%	specimen 1	1.09×10^{-4}	7.76×10^{-10}	1.12
		specimen 2	9.38×10^{-5}	1.01×10^{-9}	1.11
		specimen 3	9.38×10^{-5}	9.04×10^{-10}	1.12
shear testing	0.5 wt.%	specimen 1	-	2.84×10^{-9}	1.06
		specimen 2	-	1.26×10^{-9}	1.07
		specimen 3	-	1.57×10^{-9}	1.09
	1.0 wt.%	specimen 1	1.66×10^{-5}	6.58×10^{-10}	1.09
		specimen 2	2.03×10^{-5}	6.10×10^{-10}	1.12
		specimen 3	1.6×10^{-5}	6.15×10^{-10}	1.11
	1.5 wt.%	specimen 1	1.55×10^{-4}	1.41×10^{-10}	1.19
		specimen 2	2.30×10^{-4}	2.27×10^{-10}	1.16
		specimen 3	4.40×10^{-4}	6.92×10^{-10}	1.23

shear strain, the effective AC conductivity decreases at low frequencies due to lower $\Delta\tilde{\sigma}_{DC}$, but the effective AC conductivity increases at high frequencies due to higher K (and vice-versa for compression and low shear).

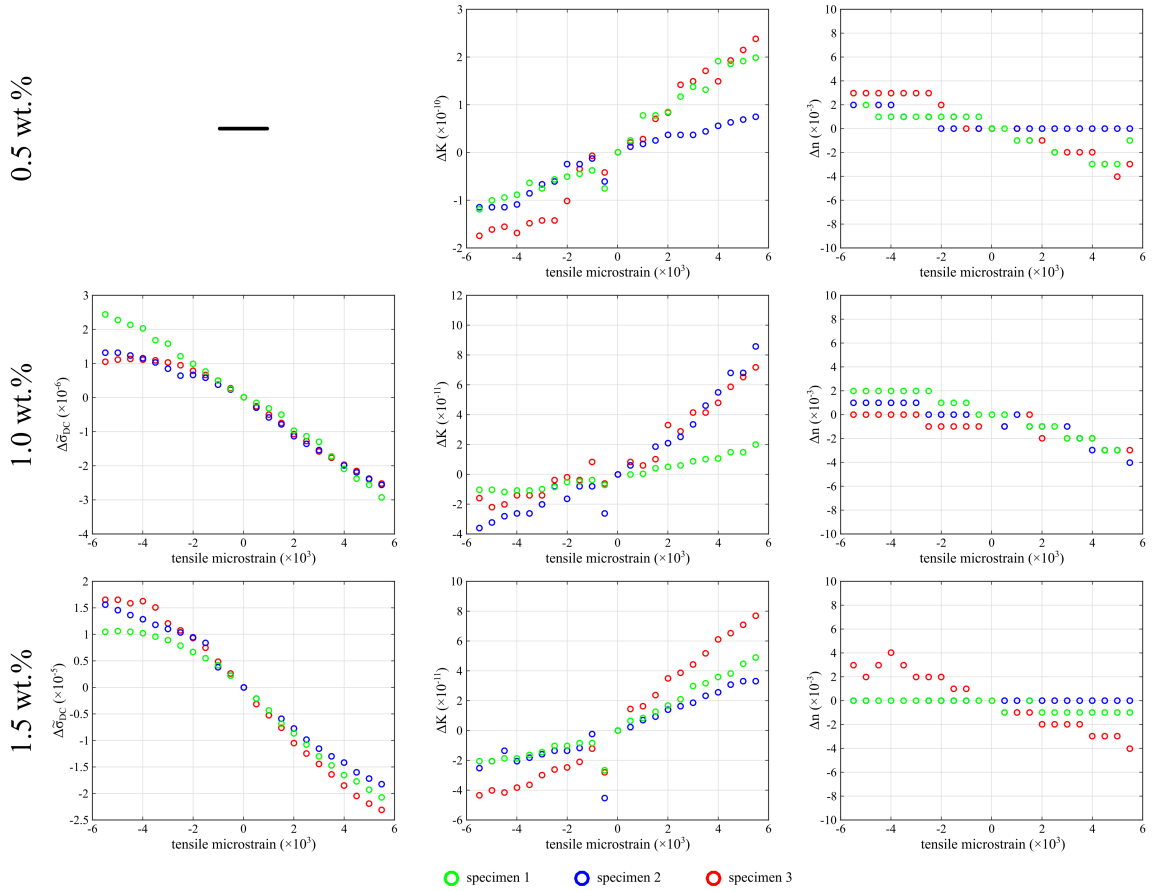

Fig. 5.15. Evolution of changes in UDR fitting parameters with tensile and compressive strain.

5.6.4 Physical Mechanisms of Piezoresistive Switching Behavior

While the preceding paragraph provides some rationale for the observed piezoresistive switching behavior, it is not particularly satisfying from a basic material perspective. Therefore, the underlying mechanism of piezoresistive switching behavior is considered next in greater detail. In order to facilitate this, EIS plots are presented. These plots utilize the experimentally measured impedance magnitude and phase angle data by converting it to real and imaginary portions via equations (4.10) and (4.11), respectively. Again, one representative plot per each weight fraction

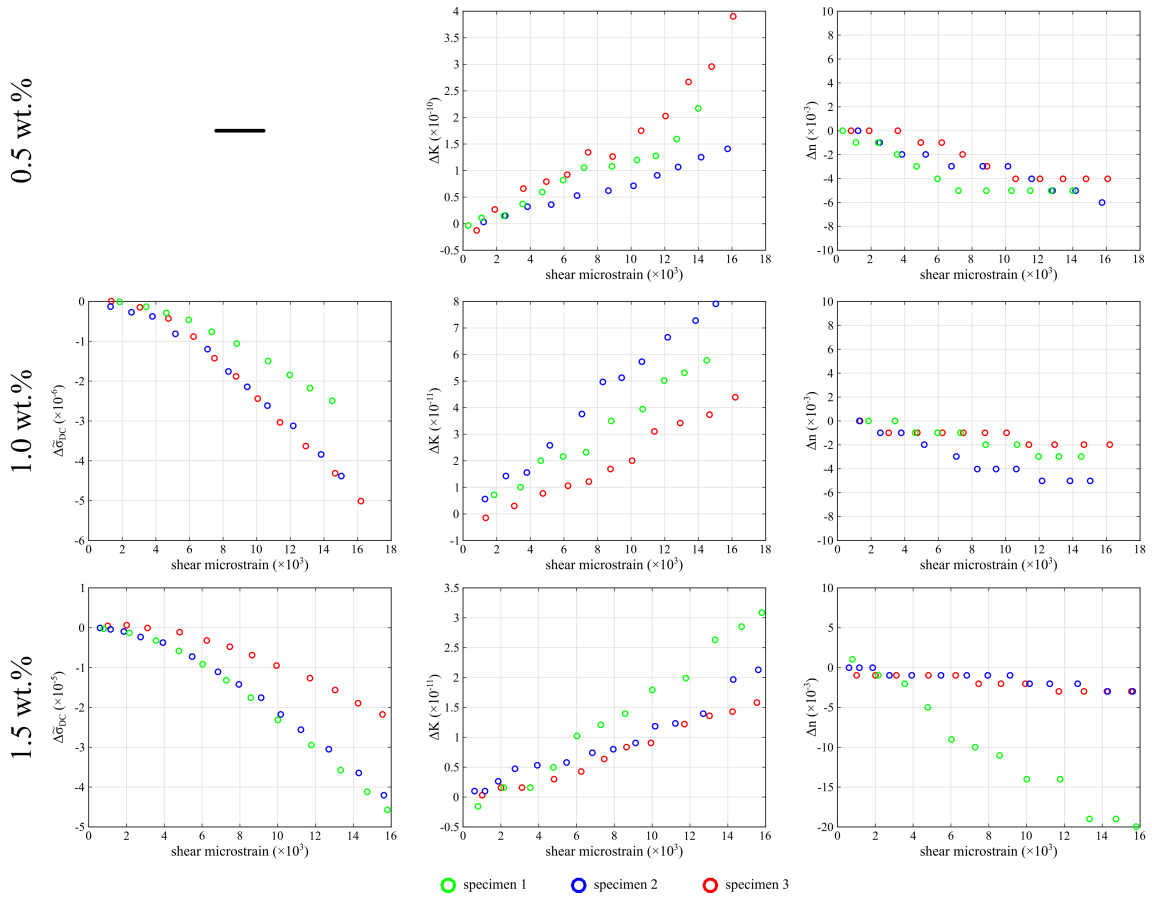

Fig. 5.16. Evolution of changes in UDR fitting parameters with shear strain.

and test is presented because they all showed similar trends and the same range of impedances across specimens. The rest of the experimentally measured EIS plots are shown in Appendix D. These EIS plots are shown in Figures 5.17 and 5.18 for normal and shear deformation, respectively. Recall that the impedance data for 0.5 wt.% at low frequencies is too noisy to draw definitive conclusions. Here, tracking the real part of the complex impedance at each step of strain state is important to understand the relationship between the effective AC conductivity and deformation. For example, consider the 1.0 wt.% EIS plot under normal strain which is shown in the middle of Figure 5.17. As the frequency increases from 100 Hz to 10 MHz, the lines extend in the counter-clockwise direction (i.e. it begins at the bottom-right and ends

at the bottom-left corners as indicated by the arrow in the middle of Figure 5.17). At low frequencies, the red curves (representing impedance in tension) is located to the right of the blue curve (representing impedance data in compression). However, as the frequency increases (i.e. extends in the counter-clockwise direction), a frequency is eventually encountered at which the red curves are to the *left* of the blue curves. That is, at low frequencies, the real portion of complex impedance in tension is greater than the real portion of the complex impedance in compression. Beyond a certain frequency, however, the real portion of the complex impedance in tension becomes lower than that in compression. Because AC conductivity is inversely dependent on Z' as shown in equation (4.12), this causes the piezoresistive response to switch from positive to negative. In light of this observation, there must also exist a frequency corresponding to zero piezoresistivity – a frequency at which the real part of the impedance in tension, compression, and without deformation all have the same value along the horizontal axis.

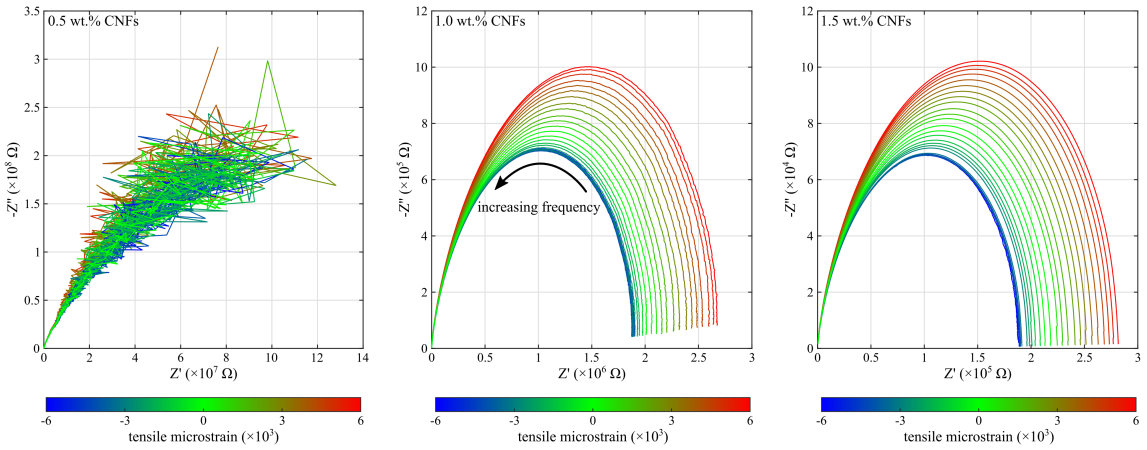

Fig. 5.17. EIS curves as a function of tensile and compressive strain. Note that for the 1.0 and 1.5 wt.% specimens, the curves expand outward with increasing tension and contract inward with increasing compression

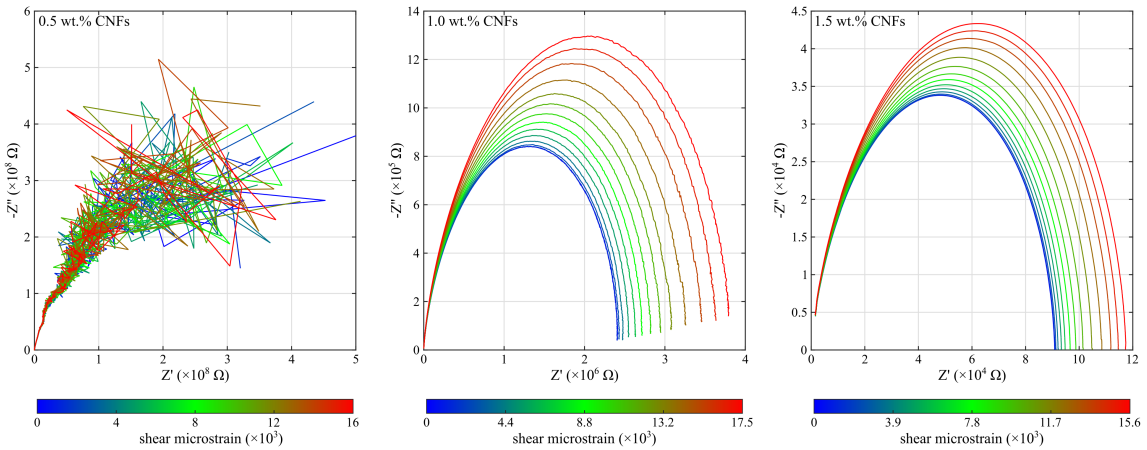

Fig. 5.18. EIS curves as a function of shear strain. Again, the 1.0 and 1.5 wt.% curves show a clear trend of expanding outward with increasing shear strain.

Along with the macroscale mechanism interpretation of piezoresistive switching behavior described in the preceding, the EIS plots also suggest insight into a more fundamental microstructural interpretation of piezoresistive switching. As shown in the EIS plots, the EIS curves have a semi-circular arc shape. Such semi-circular shapes are generally indicative of parallel resistor-capacitor-like behavior. In fact, AC transport in carbon nanofiller modified composites is often modeled via equivalent circuit models such as shown in the left of Figure 5.19 [111, 113, 136–138]. Furthermore, the EIS plots obtained from this work show that the arcs move outward with increasing normal and shear strains and inward with decreasing normal and shear strains. This is a noteworthy observation because elementary circuit analysis reveals that varying the parallel resistance of the circuit shown in the left of Figure 5.19 has the same effect on EIS plots – shifting the EIS curves inward and outward for decreasing and increasing parallel resistance, respectively.

Armed with this insight, it is important to note that prior work has shown that inter-filler junctions behave as a resistor in parallel with a capacitor for AC transport [136]. The resistance arises as a result of inter-filler tunneling while the capacitance

is due to a dielectric (i.e. the non-conductive matrix material) being sandwiched between two conductors (i.e. the carbon nanofillers). In light of this, it is hypothesized that the observed changes in EIS plots due to applied strains are caused by changes in tunneling resistance in the parallel resistor-capacitor junctions.

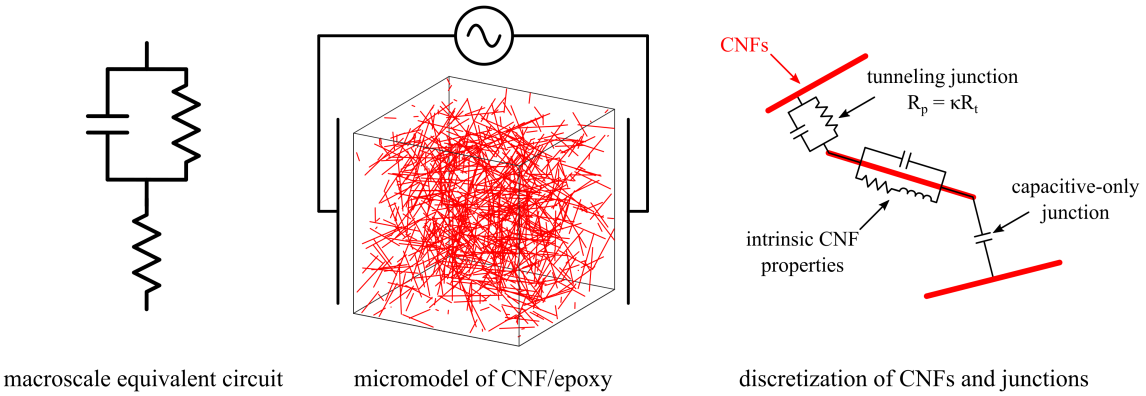

Fig. 5.19. Left: Macroscale equivalent circuit commonly used to describe bulk AC properties of carbon nanocomposites. The series resistor accounts for the DC resistance whereas the parallel resistor-capacitor component accounts for the arc-like behavior seen in EIS plots. Middle: Representation of the micromodel used to explore the mechanisms of piezoresistive switching in this work. Right: Schematic representation of how individual CNFs and inter-CNF junctions are discretized in the micromodel.

In order to test this hypothesis, an AC transport micromodel originally developed by Tallman and Hassan [122,127] was adpoted and modified for this work. The modeling process is briefly recapped here, but interested readers are directed to the original works for more detailed treatment. In this model, individual CNFs are simulated within a microscale domain. The fillers are treated as one-dimensional sticks and are randomly dispersed in the microdomain (i.e. the sticks are not pre-disposed to align in any direction). A representative image of the microdomain is shown in the middle of Figure 5.19. Once the fillers are generated, they are discretized into AC circuit elements. Junctions between fillers are also discretized into AC circuit elements. CNFs

are discretized into a capacitor in parallel with a series resistor-inductor arrangement as shown to the right in Figure 5.19. The resistor is due to the intrinsic conductivity of the CNF, the capacitor is due to interfacial capacitance between the highly conductive CNF and the insulating polymer matrix, and the inductor is due to the kinetic inductance of the filler. Further discussion on these mechanisms can be found in [139]. For inter-filler electrical connectivity, two cases are considered: i) nanofillers that are within the electron tunneling range and ii) nanofillers that are outside of the tunneling range but within a capacitive coupling range. During the original work by Tallman and Hassan [122], it was found that the model could only be fit to experimental data by the inclusion of this single inter-CNF capacitor thereby suggesting that inter-filler capacitance may act over a larger distance than electron tunneling. Electron tunneling resistance was calculated via Simmon's equation as shown below in equation (5.3) [140]. Inter-CNF capacitance was calculated by treating capacitive junctions as parallel-plate capacitors as shown in equation (5.4) below.

$$R_t = \frac{h^2 t}{Ae^2\sqrt{2m\lambda}} \exp\left(\frac{4\pi t}{h}\sqrt{2m\lambda}\right) \tag{5.3}$$

$$C = (\alpha \text{ or } \gamma)\,\frac{\epsilon_0 \epsilon_r A}{t} \tag{5.4}$$

In the preceding equations, h is Planck's constant, λ is the tunneling barrier height (2.07 eV here), m is the mass of an electron, e is the charge of an electron, A is the area overlap between interacting fillers (assumed to be equal to the cross-sectional area of the CNFs), t is the distance between a particular CNF pair, α and γ are fitting parameters, ϵ_0 is the vacuum permittivity, and ϵ_r is the relative permittivity of the matrix. In these micromodels, fitting parameters α and γ are included due to an absence of experimental data on inter-filler capacitance magnitude. These were found by using a Monte Carlo procedure to fit model predictions of normalized EIS data to experimentally measured EIS data for 1.0, 1.5, and 2.0 wt.% CNFs in epoxy produced as previously described. The predictive power of this microscale simulation is shown in Figure 5.20.

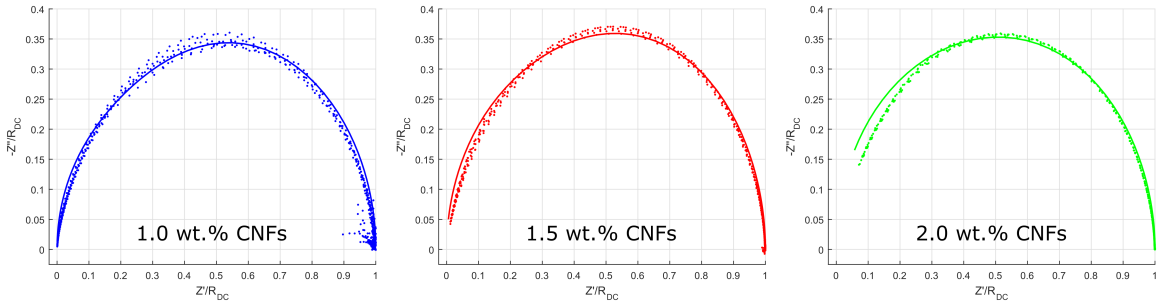

Fig. 5.20. Validation of micromodel on CNF/epoxy at several weight fractions. Dots represent experimental data whereas are lines are model predictions [122].

After discretizing the CNFs and their inter-filler junctions, the complex impedance of each circuit element is expressed via standard series or parallel combination methods of the following basic elements shown below where R is some resistance, L is some inductance, and C is some capacitance.

$$Z_R = R \tag{5.5}$$

$$Z_L = j\omega L \tag{5.6}$$

$$Z_C = \frac{1}{j\omega C} \tag{5.7}$$

For a prescribed boundary voltage, the current through the microdomain can be determined by solving a system of equations as $\mathbf{KV} = \mathbf{I}$ where $\mathbf{K}$ is a complex-valued impedance system matrix, $\mathbf{V}$ is an applied boundary voltage vector, and $\mathbf{I}$ is a current vector. $\mathbf{K}$ is formed by assembling elemental-level impedance matrices (i.e. the impedance of each particular CNF or junction) shown in equation (5.8) where Z_e is the impedance of the eth circuit element by enforcing Kirchhoff's current law and Kirchhoff's voltage law. With the current-voltage relation, the bulk complex impedance of the network for a particular interrogation frequency can be solved by

$Z_{bulk} = V_{BC}/I_{total}$ where V_{BC} is the applied boundary voltage and I_{total} is the total current flow over the microscale domain.

$$\mathbf{K}_e = \frac{1}{Z_e}\begin{bmatrix} 1 & -1 \\ -1 & 1 \end{bmatrix} \tag{5.8}$$

To explore the hypothesis on the mechanism of piezoresistive switching with the micromodel, the parallel inter-filler resistance needs to be further investigated. To this end, the inter-filler parallel resistance is varied by multiples of the baseline tunneling resistance as $R_p = \kappa R_t$ where R_p is the parallel resistance used in this simulation between a particular CNF pair, κ is a multiplicative factor, and R_t is the baseline tunneling resistance as determined by equation (5.3). The EIS plots with respect to varying inter-filler parallel resistance multiplicative factors are shown in Figure 5.21. Note that these EIS curves are normalized by strain-free DC resistance of the network, R_0, for ease of visualization.

An important observation can be made regarding Figure 5.21 – the micromodel-predicted results show the same trend as the experimental results seen in Figures 5.17 and 5.18. That is, EIS curves shift outward and inward with respect to increasing and decreasing the multiplicative factors, respectively. This shifting behavior is important because it provides a basic mechanism for explaining the piezoresistive switching. In other words, the nanofillers move closer together when subject to compressive strain thereby resulting in a tunneling resistance decrease. This is akin to the micromodel simulation with $\kappa < 1$. On the other hand, when subject to tensile strain, the tunneling resistance increases due to increased distance between nanofillers. This is akin to the micromodel simulation with $\kappa > 1$. Therefore, in combination with the preceding discussion on piezoresistive switching manifesting due to strained real impedance being less than or greater than unstrained real impedance as a function of frequency, it is reasonable to conclude that variations in the inter-filler tunneling resistance acting in parallel inter-filler capacitance are likely the underlying physical mechanism of the observed piezoresistive switching behavior.

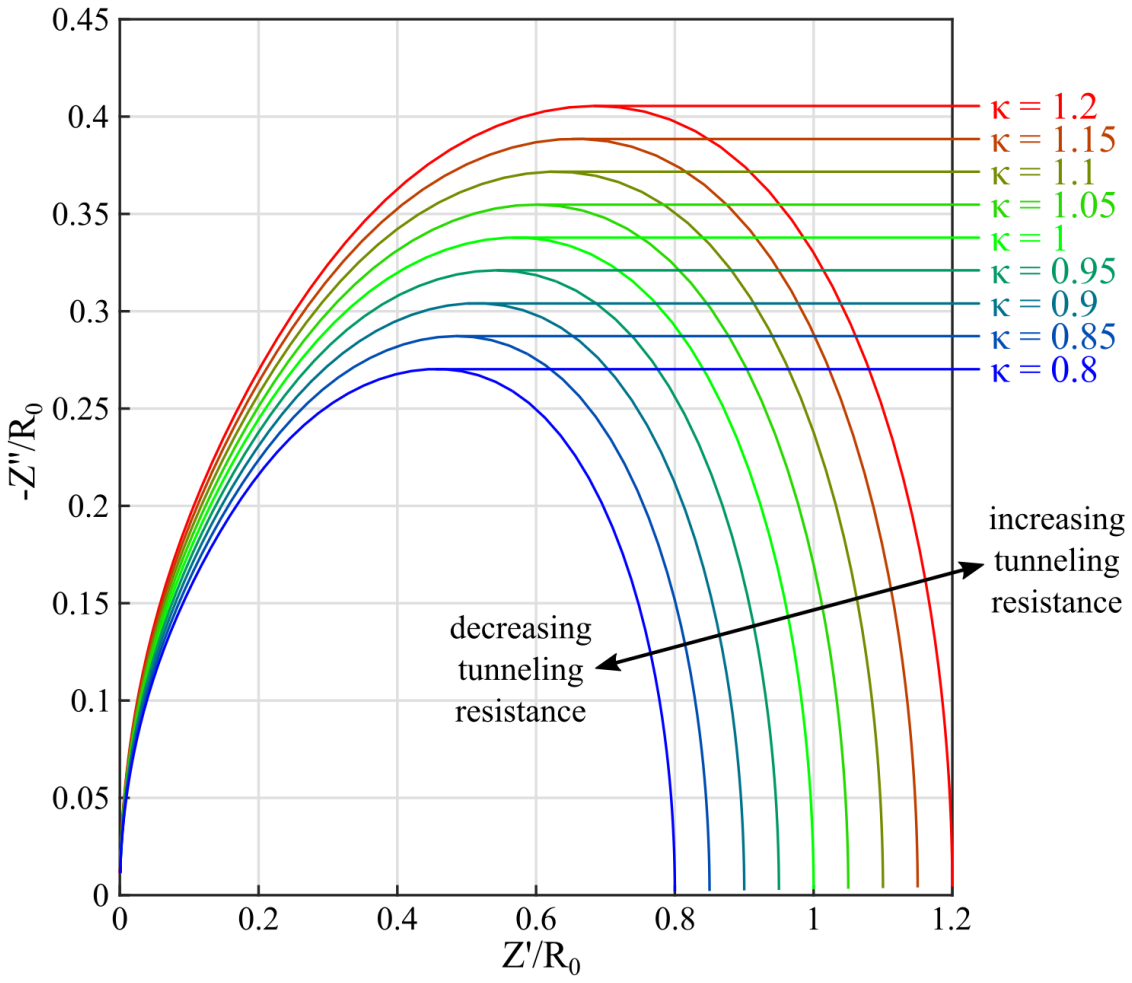

Fig. 5.21. Effect of modulating the inter-CNF parallel resistance on EIS curves. Increasing κ shifts the curves outward whereas decreasing κ shifts the curves inward. This is consistent with experimental observations for tension and compression, respectively.

5.7 Summary and Conclusion

In summary, this chapter has presented three important results: i) the population and validation of a tensor-based resistivity-strain relation, ii) the suitability of the UDR to model AC piezoresistivity and the evolution of fitting parameters as a function

of normal and shear strain, and iii) the underlying mechanism of the frequency-dependent piezoresistive switching which was experimentally observed in CNF/epoxy.

The DC general higher-order resistivity-strain relation was predicated on three assumptions – materials are limited to infinitesimal strains, materials exhibit isotropic piezoresistivity (i.e. no directional dependence in resistivity changes), and resistivity changes are non-linear. The first assumption was satisfied by the strain limits selected for testing, and, regarding the third assumption, a non-linear resistivity-strain relation was observed in the experimental data. The second assumption, however, had to be validated. For this, three-dimensional resistivity measurements were collected from CNF/epoxy plates and resistance changes of thick dog-bone specimens were measured in the pour and flow directions. It was observed that the material exhibited slight electrical anisotropy (being more conductive in the in-plane or flow direction and less conductive in the out-of-plane or pour direction). However, both directions exhibited the same normalized resistance change thereby confirming the second assumption. CNF-modified epoxy specimens manufactured at 0.5, 1.0, and 1.5 wt.% CNFs were then tested for the proposed tensorial relation. Three dog-bone and v-notched specimens per each weight fraction were loaded in normal and shear direction as the DC resistance was measured. A model-matching approach was used to determine the resistivity change of the specimens as a function of strain. The proposed tensor model was fit to this data in order to find the piezoresistive constants. After determining the piezoresistive constants, two types of experimental validation test were conducted — discrete resistance measurements as a function of displacement for S-shaped specimens and spatially varying resistivity changes in the vicinity of a stress concentration via EIT. In both validation cases, the proposed tensorial relation was able to accurately match the experimental observations.

Next, deformation-dependent AC conductivity was studied in CNF-modified epoxy. These materials were again loaded in normal and shear as impedance magnitude and phase angle were measured from 100 Hz up to 10 MHz. Raw impedance magnitude and phase angle showed clear deformation dependency. Next, these raw electrical

measurements were converted to a herein-defined effective AC conductivity which was then fit to the UDR power law. It was observed that the fitting parameters are also showed clear trends with respect to deformation. Further, changes in these fitting parameters as a function of strain were fairly consistent. This suggests that these deformation-dependent fitting parameters can be utilized in order to predict AC piezoresistive response thereby providing a new framework by which macroscale AC piezoresistivity can be quantified. It was also observed that the relationship between the fitting parameters and strain is generally non-linear.

While studying the AC piezoresistivity of CNF/epoxy, a novel piezoresistive switching behavior was also observed. At low frequencies, the material showed positive piezoresistivity. However, material exhibited negative piezoresistivity at high frequencies. Consequently, there exists a frequency of zero piezoresistivity between the positive and negative responses. EIS plots were utilized in order to understand the underlying physical mechanism of this switching behavior. It was observed that, for a given tensile strain, the real part of the impedance, which is used in calculating AC conductivity, can transition from being greater than the unstrained real impedance to being less than the unstrained real impedance beyond a certain frequency (and vice-versa for compressive deformations). From a macroscopic perspective, this explains the piezoresistive switching behavior. Furthermore, a micromodel was utilized to more fundamentally explore the switching behavior. From this micromodel, it is likely that the shift in EIS curves is due to applied strain affecting the inter-filler tunneling resistance which acts in the parallel with inter-filler capacitance. By modulating this resistance, the micromodel is able to replicate the experimental observations of EIS curves under deformation. Therefore, it is speculated that the underlying physical mechanism of the piezoresistive switching behavior is due to deformations varying the inter-filler resistance.

6. SUMMARY OF SCHOLARLY CONTRIBUTIONS AND BROADER IMPACTS

In this chapter, a summary of the scholarly contributions is provided. Additionally, the context in which these contributions may have positive broader impacts is summarized.

6.1 DC Piezoresistivity

A primary goal of this work was to develop a resistivity-strain relation that is amenable to general states of deformation, accurately captures the non-linear response of piezoresistive materials, and can be fully characterized without extensive knowledge of the material's microstructure. This goal was motivated by the potential of piezoresistive-based self-sensing in broad and far-reaching applications, a lack of work to-date in the area of quantifying resistivity-strain relationship for general macroscale deformations, and limitations of existent work such as microstructural complexity, computational cost, and limited accuracy. To this end, a general higher-order resistivity-strain relation was proposed, calibrated to a representative piezoresistive material, and validated on CNF-modified epoxy with good accuracy. Thus, the scholarly contribution of this aspect of this thesis work is the development and validation of a new modeling framework for piezoresistive materials.

This contribution has numerous broader impacts. First, because of the pervasive potential applications of piezoresistive-based self-sensing (e.g. biomedical implants, civil infrastructure, robotic sensing, composite structures, etc.), this contribution has potential to affect diverse, far-reaching branches of engineering which positively impact human health and safety. Second, it is important to note that although the herein proposed resistivity-strain relation considered a simple class of materials (i.e.

mechanically isotropic, infinitesimal strains, and isotropic resistivity changes), it is nonetheless still directly applicable to a wide class of materials such as piezoresistive cements, ceramics, and hard polymers without reinforcing fiber. Further, because the formulation is microstructure agnostic, it can even be applied to other classes of piezoresistive material systems which do not depend on percolation-based transport. Such materials include, for example, (semi-)saturated cementitous materials (the conductivity of which depends on the level of saturation and the tortuosity of the pore space [141]) and silicon semiconductors (due to strain affecting bandgap properties of the material [142]).

6.2 AC Piezoresistivity

The second part of this thesis concerned AC-based self-sensing in piezoresistive materials. The goal of this part of the thesis was to establish a framework by which macroscale AC piezoresistivity can be modeled. This goal was motivated by the relative advantages of AC-based self-sensing compared to DC methods and the dearth of work to-date in this area. For this, Jonscher's power law was postulated as a framework by which AC piezoresistivity can be characterized by expressing the fitting parameters of this relation as a function of strain. This was demonstrated on CNF/epoxy. It was observed that changes in fitting parameters expressed as a function of strain show relatively good specimen-to-specimen consistency. This suggests that the UDR may be a viable method of modeling macroscale AC piezoresistivity. During AC piezoresistivity testing, a frequency-dependent piezoresistive switching behavior was also observed. That is, the material exhibited positive piezoresistivity at low frequencies and negative piezoresistivity at high frequencies. Through a combination of macroscale EIS testing and microscale modeling, it was found that parallel resistor-capacitor connections at CNF-to-CNF junctions with strain-dependent resistance are the underlying physical mechanism for this switching behavior. Thus, this part of the thesis work resulted in two scholarly contributions: i) the UDR was exper-

imentally shown to be a viable approach to modeling macroscale AC piezoresistivity and ii) frequency-controllable piezoresistive behavior was discovered and its physical origins were elucidated.

This work on AC piezoresistivity likewise has potential to result in important broader impacts. First, the preceding discussion on the benefits of self-sensing materials in biomedical, structural, and robotic applications still applies to AC-based self-sensing. Recalling that AC methods have important advantages of DC methods, developing new basic knowledge on AC piezoresistivity and tools by which this effect can be modeled is an important for proliferating this approach. Second, frequency-dependent switching behavior provides new means by which the properties of these materials can be actively controlled. This can potentially be of immense consequence by allowing piezoresistivity to be reversed or even turned off (i.e. by interrogating at a frequency of zero piezoresistivity) depending on the application. Beyond self-sensing, this may even have important broader impacts in fields such as flexible nanocomposite-based electronics [143] by allowing conductivity changes to be turned off as the flexible electronic component deforms.

7. RECOMMENDATIONS FOR FUTURE WORK

Despite the contributions of this work, it is important to acknowledge aspects that would benefit from further study. Therefore, recommendations for future work are provided below.

7.1 General Higher-Order Piezoresistive Tensorial Relations

The work presented in this thesis considered the simplest class of piezoresistive materials. Namely, those which are limited to infinitesimal strains, exhibit isotropic resistivity changes, and which are mechanically isotropic. Despite these simplifying restrictions, it is important to note that this modeling approach is still directly applicable to a wide range of piezoresistive or self-sensing cementitious materials, ceramics, and hard polymers. Nonetheless, the results of this thesis work set the stage for future work in the following areas:

- *Validation on other material systems:* A key feature of the modeling framework presented in this work is its applicability to any piezoresistive material system. Herein, it was validated on a CNF-modified epoxy. Future work, however, should validate this approach on other piezoresistive material systems that satisfy the model assumptions such as conductive filler-modified cement.

- *Electro-mechanically anisotropic materials:* An important next step for this line of research will be extending the proposed higher-order formulation to materials that are both electrically and mechanically anisotropic. Prototypical materials fitting this description are fiber reinforced composites (e.g. nanofiller-modified glass fiber-reinforced composites and continuous carbon fiber-reinforced composites which also exhibit intrinsic piezoresistive properties even without filler

modification [144, 145]). In such a formulation, the resistivity change will have to be amended as a symmetric, second-order tensor, $\Delta\rho_{ij}$.

- *Large deformation/mechanically non-linear materials:* Soft polymeric composites (e.g. modified silicone) comprise a large portion of the interest in self-sensing materials, particularly for use in human-interfacing technology and robotic artificial skin [146]. In these materials, infinitesimal strains are obviously a poor assumption. Further, deformation-induced anisotropy is likely to occur. To clarify, non-spherical fillers tend to rotate and align with the direction of the algebraically largest principal strain during deformation. For very small strains, this effect is inconsequential. For large deformations such as those that can be sustained by soft elastomers, on the other hand, fillers rotating to such an extent that anisotropic conductivity is induced is possible. In such a case, the assumption that resistivity changes are isotropic would be violated, and the tensor relation would have to be reformulated as $\Delta\rho_{ij} = \Delta\rho_{ij}(E_{ij})$ where the resistivity change is again expressed as a symmetric, second-order tensor in order to account for the possibility of deformation-induced ansiotropy and E_{ij} is the Green-Lagrangian strain tensor as a representative large-strain metric.

7.2 Exploration of AC-Based Piezoresistivity

The second part of this thesis work concerned developing a framework for modeling the AC piezoresistive effect in self-sensing materials. Due to practical constraints associated with collecting AC measurements in-situ during deformation, results were presented in terms of the effective AC conductivity. Nonetheless, the use of the effective AC conductivity is justified because it shows the same frequency-dependent trends as true AC conductivity thereby allowing for the UDR and Jonscher's power-law to be fit to the data as a function strain. It was noted that changes in power-law fitting parameters may be a suitable macroscale metric for quantifying AC piezoresistivity. A frequency-dependent switching behavior from positive piezoresistivity to

negative piezoresistivity was also observed. In light of these results, directions for future work are recommend as below.

- *Recovery of true AC conductivity for the development of general tensor-based relations of AC piezoresistivity:* Although the work presented in this thesis demonstrated the potential of the UDR for modeling AC piezoresistivity, this work fell short of developing a general tensor-based AC conductivity-strain relation (like what was done for DC resistivity). This is a consequence of not being able to measure the real part of the permittivity, ϵ' of the material as a function of strain (recall that net AC transport is governed by the admittivity of the material, $\xi = (\sigma_{DC} + \omega\epsilon'') + j\omega\epsilon'$). Therefore, future work should seek to develop experimental methods that can measure the effect of deformation on the real part of permittivity of these materials. With this information, a model-fitting approach (like what was done for recovering DC resistivity from resistance changes) could be employed to recover the true AC conductivity of the material as a function of strain. Then, the UDR fitting parameters could be expressed as functions of a the infinitesimal strain tensor as $\sigma_{DC} = \sigma_{DC}(\varepsilon_{ij})$, $K = K(\varepsilon_{ij})$, and $n = n(\varepsilon_{ij})$.

- *Extension to electro-mechanically anisotropic materials and large deformations:* Much like the direction for future work outlined above regarding DC piezoresistivity modeling, AC piezoresistivity modeling should also be extended to materials that are electro-mechanically anisotropic and to materials sustaining large deformations.

REFERENCES

REFERENCES

[1] S. Guthrie, "Bam car park collapse agreement," *Construction europe*, 2019.

[2] T. J. Arsenault, A. Achuthan, P. Marzocca, C. Grappasonni, and G. Coppotelli, "Development of a fbg based distributed strain sensor system for wind turbine structural health monitoring," *Smart Mater. Struct.*, vol. 22, p. 075027, 2013.

[3] H. Ghednia, C. E. Owens, R. Ricard, T. N. Tallman, A. J. Hart, and K. M. Varadarajan, "Interfacial load monitoring and failure detection in total joint replacements via piezoresistive bone cement and electrical impedance tomography," *Smart Materials and Structures*, vol. 29, p. 085039, 2020.

[4] M. Kanerva, P. Antunes, E. Sarlin, O. Orell, J. Jokinen, M. Wallin, T. Brander, and J. Vuorinen, "Direct measurement of residual strains in cfrp-tungsten hybrids using embedded strain gauges," *Materials & Design*, vol. 127, pp. 352–363, 2017.

[5] D. Crescini, A. Flammini, D. Marioli, and A. Taroni, "Application of an fft-based algorithm to signal processing of lvdt position sensors," *IEEE Transactions on Instrumentation and Measurement*, vol. 47, p. 5, 1998.

[6] E. Ibraim and H. D. Benedetto, "New local system of measurement of axial strains for triaxial apparatus using lvdt," *Geotechnical Testing Journal*, vol. 28, pp. 436–444, 2005.

[7] E. Tutumluer, N. Garg, and M. R. Thompson, "Granular material radial deformation measurements with a circumferential extensometer in repeated load triaxial testing," *Transport. Res. Rec*, vol. 1614, pp. 61–69, 1998.

[8] S. Yimsiri, K. Soga, and S. Chandler, "Cantilever-type local deformation transducer for local axial strain measurement in triaxial test," *Geotechnical Testing Journal*, vol. 28, p. 11432, 2005.

[9] R. A. Sliva-Munoz and R. A. Lopez-Anido, "Structural health monitoring of marine composite structural jointsusing embedded fiber bragg grating strain sensors," *Composite Structures*, vol. 89, pp. 224–234, 2009.

[10] S. Uchida, E. Levenberg, and A. Klar, "On-specimen strain measurement with fiber optic distributed sensing," *Measurement*, vol. 60, pp. 104–113, 2015.

[11] S. M. Melle, K. Liu, and R. M. Meaures, "Practical fiber-optic bragg grating strain gauge system," *Applied Optics*, vol. 32, pp. 3601–3609, 1993.

[12] M. Tabib-Azar, B. Sutapun, R. Petrick, and A. Kazemi, "Highly sensitive hydrogen sensors using palladium coated fiber optics with exposed cores and evanescent field interaction," *Sensors and Actuators B*, vol. 56, pp. 158–163, 1999.

[13] H. Choi, S. Choi, and H. Cha, "Structural health monitoring system based on strain gauge enabled wireless sensor nodes," *IEEE*, 2008.

[14] I. Bayane and E. Bruhwiler, "Structural condition assessment of reinforced-concrete bridges based on acoustic emission and strain measurements," *Journal of Civil Structural Health Monitoring*, vol. 78, 2020.

[15] J. P. Liu, M. A. Vaz, R. Q. Chen, M. L. Duan, and I. Hernandez, "Axial mechanical experiments of unbonded fexible pipes," *Petroleum Science*, vol. 44, 2020.

[16] J. A. Hernandez, N. Kedir, B. H. Lim, W. Chen, and T. N. Tallman, "An experimental study on the piezoresistive and mechanical behavior of carbon nanocomposites subject to high-rate elastic loading," *Composites Science and Technology*, vol. 198, p. 108285, 2020.

[17] J. Choi and S. J. Dyke, "Crowdlim: Crowdsourcing to enable lifecycle infrastructuremanagement," *Computers in Industry*, vol. 115, pp. 103–185, 2020.

[18] J. Choi, C. M. Yeum, S. J. Dyke, and M. R. Jahanshahi, "Computer-aided approach for rapid post-event visual evaluation of a building façade," *Sensors*, vol. 18, p. 3017, 2018.

[19] X. Kong and J. Li, "Vision-based fatigue crack detection of steel structures using video feature tracking," *Comput-Aided Civ Infrastruct Eng.*, vol. 33, pp. 783–799, 2018.

[20] I. Abdel-Qader, O. Abudayyeh, and M. E. Kelly, "Analysis of edge-detection techniques for crack identification in bridges," *J. Comput. Civ. Eng.*, vol. 17, pp. 255–263, 2003.

[21] M. R. Jahanshahi, S. F. Masri, C. W. Padgett, and G. S. Sukhatme, "An innovative methodology for detection and quantification of cracks through incorporation of depth perception," *Machine Vision and Applications*, vol. 24, pp. 227–241, 2013.

[22] V. Hoskere, J. Park, H. Yoon, and F. Spencer, "Vision-based modal survey of civil infrastructure using unmanned aerial vehicles," *J. Struct. Eng.*, vol. 145, p. 04019062, 2019.

[23] Y. Yu, R. Han, X. Zhao, X. Mao, W. Hu, D. Jiao, M. Li, and J. Ou, "Initial validation of mobile-structural health monitoring method using smartphones," *International Journal of Distributed Sensor Networks*, vol. 11, p. 274391, 2015.

[24] N. McComick and J. Lord, "Digital image correlation," *Materialstoday*, vol. 13, pp. 52–54, 2010.

[25] D. Lecompte, A. Smits, S. Bossuyt, H. Sol, J. Vantomme, V. Hemelrijck, and A. M. Habraken, "Quality assessment of speckle patterns for digitalimage correlation," *Optics and Lasers in Engineering*, vol. 44, pp. 1132–1145, 2006.

[26] B. Pan, K. Qian, H. Xie, and A. Asundi, "Two-dimensional digital image correlation for in-plane displacement and strain measurement: a review," *Measurement Science and Technology*, vol. 20, p. 062001, 2009.

[27] G. Vendroux and W. G. Knauss, "Submicron deformation field measurements: Part 2. improved digital image correlation," *Experimental Mechanics*, vol. 38, pp. 86–92, 1998.

[28] H. A. Bruck, S. R. McNeill, M. A. Sutton, and W. H. Peters, "Digital image correlation using newton-raphson method of partial differential correction," *Experimental Mechanics*, vol. 29, pp. 261–267, 1989.

[29] Y. I. Ostrovsky, V. P. Shchepinov, and V. V. Yakovlev, "Holographic interferometry in experimental mechanics," *Springer Series in Optical Sciences*, vol. 60, pp. 24–87, 1991.

[30] M. Hytch, F. Houdellier, F. Hue, and E. Snoeck, "Nanoscale holographic interferometry for strain measurements in electronic devices," *Nature*, vol. 453, pp. 1086–1090, 2008.

[31] L. O. Heplinger, R. F. Wuerker, and R. E. Brooks, "Holographic interferometry," *Journal of Applied Physics*, vol. 37, p. 642, 1966.

[32] K. Takayama, "Application of holographic interferometry to shock wave research," *Proc. Spie 0398 Industrial Applications of Laser Technology*, 1983.

[33] Y. Y. Hung, "Shearography: A novel and practical approach for nondestructive inspection," *Journal of Nondestructive Evaluation*, vol. 8, pp. 55–67, 1989.

[34] Y. Y. Hung and H. P. Ho, "Shearography: An optical measurement technique and applications," *Materials Science and Engineering R*, vol. 49, pp. 61–87, 2005.

[35] D. Francis, R. P. Tatam, and R. M. Groves, "Shearography technology and applications: a review," *Measurement Science and Technology*, vol. 21, p. 102001, 2010.

[36] W. Steinchen, L. X. Yang, G. Kupfer, P. Mackel, and F. Vossing, "Strain analysis by means of digital shearography: potential, limitations and demonstration," *Journal of Strain Analysis*, vol. 33, pp. 171–182, 1998.

[37] S. P. Bao and S. C. Tjong, "Mechanical behaviors of polypropylene/carbon nanotube nanocomposites: The effects of loading rate and temperature," *Materials Science and Engineering: A*, vol. 485, pp. 508–516, 2008.

[38] S. C. Tjong, G. D. Liang, and S. P. Bao, "Electrical behavior of polypropylene/multiwalled carbon nanotube nanocomposites with low percolation threshold," *Scripta Materialia*, vol. 57, pp. 461–464, 2007.

[39] S. Gong, D. Wu, Y. Li, M. Jin, T. Xiao, Y. Wang, Z. Xiao, Z. Zhu, and Z. Li, "Temperature-independent piezoresistive sensors based on carbon nanotube/polymer nanocomposite," *Carbon*, vol. 137, pp. 188–195, 2018.

[40] C. Gau, H. S. Ko, and H. T. Chen, "Piezoresistive characteristics of mwnt nanocomposites and fabrication as a polymer pressure sensor," *Nanotechnology*, vol. 20, p. 185503, 2009.

[41] N. T. Selvan, S. B. Eshwaran, A. Das, K. W. Stockelhuber, S. Wiebner, P. Potschke, G. B. Nando, A. I. Chervanyov, and G. Heinrich, "Piezoresistive natural rubber-multiwall carbon nanotubenanocomposite for sensor applications," *Sensors and Actuators A: Physical*, vol. 239, pp. 102–113, 2016.

[42] L. Lin, S. Liu, Q. Zhang, X. Li, M. Ji, H. Deng, and Q. Fu, "Towards tunable sensitivity of electrical property to strain for conductive polymer composites based on thermoplastic elastomer," *Applied Materials Interfaces*, vol. 5, pp. 5815–5824, 2013.

[43] C. Lozano-Perez, J. V. Cauich-Rodriguez, and F. Aviles, "Influence of rigid segment and carbon nanotube concentration on thecyclic piezoresistive and hysteretic behavior of multiwall carbonnanotube/segmented polyurethane composites," *Composites Science and Technology*, vol. 128, pp. 25–32, 2016.

[44] T. Shi, Z. Li, J. Guo, H. Gong, and C. GU, "Research progress on cnts/cnfs-modified cement-based composites – a review," *Construction and Building Materials*, vol. 202, pp. 290–307, 2019.

[45] H. Gong, Y. Zhang, J. Quan, and S. Che, "Preparation and properties of cement based piezoelectric composites modified by cnts," *Current Applied Physics*, vol. 11, pp. 653–656, 2011.

[46] Y. Wang, X. Zhao, and Y. Zhao, "Piezoresistivity of cement matrix composites incorporating multiwalled carbon nanotubes due to moisture variation," *Advances in Civil Engineering*, vol. 2020, p. 5476092, 2020.

[47] A. Meoni, A. D'Alessandro, A. Downey, E. Garcia-Macias, M. Rallini, A. L. Materazzi, L. Torre, S. Laflamme, R. Castro-Triguero, and F. Ubertini, "An experimental study on static and dynamic strain sensitivity of embeddable smart concrete sensors doped with carbon nanotubes for shm of large structures," *Sensors*, vol. 18, p. 831, 2018.

[48] L. Gao, L. Jiang, and J. Sun, "Carbon nanotube-ceramic composites," *J Electroceram*, vol. 17, pp. 51–55, 2006.

[49] J. Cho, A. R. Boccaccini, and M. S. P. Shaffer, "Ceramic matrix composites containing carbon nanotubes," *Journal of Materials Science*, vol. 44, pp. 1934–1951, 2009.

[50] V. T. Rathod, J. S. Kumar, and A. Jain, "Polymer and ceramic nanocomposites for aerospace applications," *Appl. Nanosci.*, vol. 7, pp. 519–548, 2017.

[51] R. Rashetnia, D. Smyl, M. Hallaji, A. Seppanen, and M. Pour-Ghaz, "Structural health monitoring using electrical resistance tomography based sensing skin: Detecting damage, corrosive elements, and temperature change." *9th International Conference on Inverse Problems in Engineering (ICIPE)*, 2017.

[52] M. Hallaji and M. Pour-Ghaz, "A new sensing skin for qualitative damage detection in concrete elements: Rapid difference imaging with electrical resistance tomography," *NDTE International*, vol. 68, pp. 13–21, 2014.

[53] M. Hallaji, A. Seppanen, and M. Pour-Ghaz, "Electrical impedance tomography-based sensing skin for quantitative imaging of damage in concrete," *Smart Materials and Structures*, vol. 23, p. 085001, 2014.

[54] J. H. Kang, C. Park, J. A. Scholl, A. H. Brazin, N. M. Holloway, J. W. High, S. E. Lowther, and J. S. Harrison, "Piezoresistive characteristics of single wall carbonnanotube/polyimide nanocomposites," *Journal of Polymer Science: Part B: Polymer Physics*, vol. 47, pp. 994–1003, 2009.

[55] A. Sanli, A. Benchirouf, C. Muller, and O. Kanoun, "Piezoresistive performance characterization of strain sensitive multi-walled carbon nanotube-epoxy nanocomposites," *Sensors and Actuators A: Physical*, vol. 254, pp. 61–68, 2017.

[56] Z. Zhang, L. Zhang, S. Wang, W. Chen, and L. Yong, "A convenient route to polyacrylonitrile/silver nanoparticle composite bysimultaneous polymerizationreduction approac," *Polymer*, vol. 42, pp. 8315–8318, 2001.

[57] K. Takei, K, Z. Yu, M. Zheng, H. Ota, T. Kakahashi, and A. Javey, "Highly sensitive electronic whiskers based on patterned carbon nanotube and silver nanoparticle composite films," *PNAS*, vol. 111, pp. 1703–1707, 2014.

[58] H. Jiang, K. Moon, and C. P. Wong, "Surface functionalized silver nanoparticles for ultrahigh conductive polymer composites," *Chem. Mater.*, vol. 18, pp. 2969–2973, 2006.

[59] Y. Lv, H. Liu, Z. Wang, S. Liu, L. Hao, Y. Sang, D. Liu, J. Wang, and R. I. Boughton, "Silver nanoparticle-decorated porous ceramic composite for water treatment," *Journal of Membrane Science*, vol. 331, pp. 50–56, 2009.

[60] K. H. Wu, T. H. Ting, G. P. Wang, W. D. Ho, and C. C. Shih, "Effect of carbon black content on electrical and microwave absorbing properties of polyaniline/carbon black nanocomposites," *Polymer Degradation and Stability*, vol. 93, pp. 483–488, 2008.

[61] M. Knite, V. Teteris, A. Kiploka, and J. Kaupuzs, "Polyisoprene-carbon black nanocomposites as tensile strain and pressure sensor materials," *Sensors and Actuators A: Physical*, vol. 110, pp. 142–149, 2004.

[62] M. Z. Ansari, M. Bisen, and C. Cho, "Modelling and analysis of diaphragm integrated su8/cb nanocomposite piezoresistive polymer microcantilever biosensor," *Microsystem Technology*, vol. 24, pp. 3061–3068, 2018.

[63] M. H. G. Wichmann, S. T. Buschhorn, J. Gehrmann, and K. Schulte, "Piezoresistive response of epoxy composites with carbon nanoparticles under tensile load," *Physical Review B*, vol. 80, p. 245437, 2009.

[64] M. A. Rafiee, J. Rafiee, I. Srivastave, Z. Wang, H. Song, Z. Yu, and N. Koratkar, "Fracture and fatigue in graphene nanocomposites," *Small*, vol. 6, pp. 179–183, 2010.

[65] K. M. F. Shahil and A. A. Baladin, "Graphene–multilayer graphene nanocomposites as highly efficient thermal interface materials," *Nano Lett*, vol. 12, pp. 861–867, 2012.

[66] B. V. S. Ke, Kai, D. Yuan, and I. Manas-Zloczower, "Piezoresistive thermoplastic polyurethane nanocomposites with carbon nanostructures," *Carbon*, vol. 139, pp. 52–58, 2018.

[67] L. M. Chiacchiarelli, M. Rallini, M. Monti, D. Puglia, J. M. Kenny, and L. Torre, "The role of irreversible and reversible phenomena in the piezoresistive behavior of graphene epoxy nanocomposites applied to structural health monitoring," *Composites Science and Technology*, vol. 80, pp. 73–79, 2013.

[68] S. Mondal, L. Nayak, M. Rahaman, A. Aldalbahi, T. K. Chaki, D. Khastgir, and N. C. Das, "An effective strategy to enhance mechanical, electrical, and electromagnetic shielding effectiveness of chlorinated polyethylene-carbon nanofiber nanocomposites," *Composite Part B: Engineering*, vol. 109, pp. 155–169, 2017.

[69] J. Zhu, S. Wei, J. Ryu, M. Budhathoki, G. Liang, and Z. Guo, "In situ stabilized carbon nanofiber (cnf) reinforced epoxy nanocomposites," *Royal Society of Chemistry*, vol. 20, pp. 4937–4948, 2010.

[70] S. Sasmal, N. Ravivarman, B. S. Sindu, and K. Vignesh, "Electrical conductivity and piezo-resistive characteristics of cnt and cnf incorporated cementitious nanocomposites under static and dynamic loading," *Composites: Part A*, vol. 100, pp. 227–243, 2017.

[71] M. Charara, W. Luo, M. C. Saha, and Y. Liu, "Investigation of lightweight and flexible carbon nanofiber/poly dimethylsiloxane nanocomposite sponge for piezoresistive sensor application," *Advanced Engineering Materials*, vol. 21, p. 1801068, 2017.

[72] L. Deng, Y. Ma, J. Hu, S. Yin, X. Ouyang, J. Fu, A. Liu, and Z. Zhang, "Preparation and piezoresistive properties of carbon fiber-reinforced alkali-activated fly ash/slag mortar," *Construction and Building Materials*, vol. 222, pp. 738–749, 2019.

[73] Y. Ma, W. Liu, J. Hu, J. Fu, Z. Zhang, and H. Wang, "Optimization on the piezoresistivity of alkali-activated fly ash/slag mortar by using conductive aggregates and carbon fibers," *Cement and Concrete Composites*, vol. 114, p. 103735, 2020.

[74] S. Nayak and S. Das, "Spatial damage sensing ability of metallic particulate-reinforced cementitious composites: Insights from electrical resistance tomography," *Materials and Design*, vol. 175, p. 107817, 2019.

[75] Alamusi, N. Hu, H. Fukunaga, S. Atobe, Y. Liu, and J. Li, "Piezoresistive strain sensors made from carbon nanotubes based polymer nanocomposites," *Sensors*, vol. 11, pp. 10 691–10 723, 2011.

[76] X. Sun, J. Sun, T. Li, S. Zheng, C. Wang, W. Tan, J. Zhang, C. Liu, T. Ma, Z. Qi, C. Liu, and N. Xue, "Flexible tactile electronic skin snesor with 3d force detection based on porous cnts/pdms nanocomposites," *Nano-Micro Letters*, vol. 11, p. 57, 2019.

[77] K. J. Loh, T. C. Hou, J. P. Lynch, and N. A. Kotov, "Carbon nanotube sensing skins for spatial strain and impact damage identification," *Journal of Nondestructive Evaluation*, vol. 28, pp. 9–25, 2009.

[78] X. Gao, T. Wei, H. Dong, and Y. Song, "Damage detection in 2.5d c/sic composites using electrical resistance tomography," *Journal of the European Ceramic Society*, vol. 39, pp. 3583–3593, 2019.

[79] S. Gupta, J. G. Gonzalez, and K. J. Loh, "Self-sensing concrete enabled by nano-engineered cement-aggregate interfaces," *Structural Health Monitoring*, vol. 16, pp. 309–323, 2017.

[80] S. Gong and Z. H. Zhu, "On the mechanism of piezoresistivity of carbon nanotube polymer composites," *Polymer*, vol. 55, pp. 4136–4149, 2014.

[81] S. Gong, Z. H. Zhu, and E. I. Haddad, "Modeling electrical conductivity of nanocomposites by considering carbon nanotube deformation at nanotube junctions," *Journal of Applied Physics*, vol. 114, p. 074303, 2013.

[82] S. Gong, Z. H. Zhu, and A. Meguid, "Carbon nanotube agglomeration effect on piezoresistivity of polymer nanocomposites," *Polymer*, vol. 55, pp. 5488–5499, 2014.

[83] N. Hu, Z. Masuda, G. Yamamoto, H. Fukunaga, T. Hashida, and J. Qui, "Effect of fabrication process on electrical properties of polymer/multi-wall carbon nanotube nanocomposites," *Composites Part A*, vol. 39, pp. 893–903, 2008.

[84] N. Hu, Y. Krube, C. Yan, Z. Masuda, and H. Fukunaga, "Tunneling effect in a polymer/carbon nanotube nanocomposite strain sensor," *Acta Materialia*, vol. 56, pp. 2929–2936, 2008.

[85] B. M. Li and K. J. Loh, "A 2d percolation-based model for characterizing the piezoresistivity of carbon nanotube-based films," *Journal of Material Science*, vol. 50, pp. 2973–2983, 2015.

[86] R. Rhaman and P. Servati, "Effects of inter-tube distance and alignment on tunnelling resistance and strain sensitivity of nanotube/polymer composite films," *Nanotechnology*, vol. 23, p. 055703, 2012.

[87] S. Gong, Z. H. Zhu, and S. A. Meguid, "Anisotropic electrical conductivity of polymer composites with aligned carbon nanotubes," *Polymer*, vol. 56, pp. 498–506, 2015.

[88] M. Taya, W. J. Kim, and K. Ono, "Piezoresistivity of a short fiber/elastomer matrix composite," *Mechanics of Materials*, vol. 28, pp. 53–59, 1998.

[89] N. Hu, Y. Krube, M. Arai, C. Watanabe, C. Yan, Y. Li, Y. Liu, and H. Fukunaga, "Investigation on sensitivity of a polymer/carbon nanotube composite strain sensor," *Carbon*, vol. 48, pp. 680–687, 2010.

[90] H. Yu, D. Heider, and S. Advani, "A 3d microstructure based resistor network model for the electrical resistivity of unidirectional carbon composites," *Composite Structures*, vol. 134, pp. 740–749, 2015.

[91] F. Dalmas, R. Dendievel, L. Chazeau, J. Caville, and C. Gauthier, "Carbon nanotube-filled polymer composites. numerical simulation of electrical conductivity in three-dimensional entangled fibrous networks," *Acta Materialia*, vol. 54, pp. 2923–2931, 2006.

[92] N. Hu, Y. Karube, M. Arai, T. Watanabe, C. Yan, Y. Li, Y. Liu, and H. Fukunaga, "Investigation on sensitivity of a polymer/carbon nanotubecomposite strain sensor," *Carbon*, vol. 48, pp. 680–687, 2010.

[93] T. N. Tallman and K. W. Wang, "The influence of nanofiller alignment on transverse percolation and conductivity," *Nanotechnology*, vol. 26, p. 025501, 2014.

[94] S. S. Prabhu, R. Bhavani, G. K. Thonnuthodi, and R. Thiruvengadathan, "A computational approach to determine shielding effectiveness of carbon nanotube-based nanocomposites for emc application," *Computational Materials Science*, vol. 126, pp. 400–406, 2017.

[95] A. K. Chaurasia and G. D. Seidel, "Computational micromechanics analysis of electron-hopping-induced conductive paths and associated macroscale piezoresistive response in carbon nanotube-polymer nanocomposites," *Journal of Intelligent Material Systems and Structures*, vol. 25, pp. 2141–2164, 2014.

[96] A. K. Chaurasia, X. Ren, and G. D. Seidel, "Computational micromechanics analysis of electron hopping and interfacial damage induced piezoresistive response in carbon nanotube-polymer nanocomposites," *Smart Materials and Structures*, vol. 23, p. 075023, 2014.

[97] A. Oliva-Aviles, F. Aviles, G. Seidel, and V. Sosa, "On the contribution of carbon nanotube defomration to piezoresistivity of carbon nanotube/polymer composites," *Composites Part B*, vol. 47, pp. 200–206, 2013.

[98] X. Ren and G. D. Seidel, "Computational micromechanics modeling of inherent piezoresistivity in carbon nanotube-polymer nanocomposites," *Journal of Intelligent Material Systems and Structures*, vol. 24, pp. 1459–1483, 2013.

[99] X. Ren, A. K. Chaurasia, A. I. Oliva-Aviles, J. J. Ku-Herrera, G. D. Seidel, and F. Aviles, "Modeling of mesoscale dispersion effect on the piezoresistivity of carbon nanotube-polymer nanocomposites via 3d computational multiscale micromechanics methods," *Smart Materials and Structures*, vol. 24, p. 060531, 2015.

[100] C. Cattin and P. Hubert, "Piezoresistance in polymer nanocomposites with high aspect ratio particles," *ACS Applied Materials Interfaces*, vol. 6, pp. 1804–1811, 2014.

[101] T. N. Tallman and K. W. Wang, "An arbitrary strains cabon nanotube composite piezoresistivity model for finite element integration," *Applied Physics Letters*, vol. 102, p. 011909, 2013.

[102] F. Deng and Q. Zheng, "An analytical model of effective electrical conductivity of carbon nanotube composites," *Applied Physics Letters*, vol. 92, p. 071902, 2008.

[103] M. A. S. Matos, S. T. Pinho, and V. L. Tagarielli, "Application of machine learning to predict the multiaxial strain-sensing response of cnt-polymer composites," *Carbon*, vol. 146, pp. 265–275, 2019.

[104] E. Garcia-Macias, R. Castro-Triguero, A. Saez, and F. Ubertini, "3d mixed micromechanics-fem modeling of piezoresistive carbon nanotube smart concrete," *Computer Methods in Applied Mechanics and Engineering*, vol. 340, pp. 396–423, 2018.

[105] T. Takeda, Y. Shindo, Y. Kuronuma, and F. Narita, "Modeling and characterization of the electrical conductivity of carbonnanotube-based polymer composites," *Polymer*, vol. 52, pp. 3852–3856, 2011.

[106] T. N. Tallman, "Damage detection in nanofiller-modified composites with external circuitry via resonant frequency shifts," *Smart Materials, Adaptive Structures and Intelligent Systems, San Antonio, TX*, 2018.

[107] X. Lu, A. Zhang, O. Dubrunfaut, D. He, L. Pichon, and J. Bai, "Numerical modeling and experimental characterization of the ac conductivity and dielectric properties of cnf/polymer nanocomposites," *Composites Science and Technology*, vol. 194, p. 108150, 2020.

[108] A. Vavouliotis, E. Fiamegou, P. Karapappas, C. Psarras, and V. Kostopoulos, "Dc and ac conductivity in epoxy resin/multiwall carbon nanotubes percolative system," *Polymer Composites*, vol. 31, pp. 1874–1880, 2010.

[109] G. T. Mohanraj, T. K. Chaki, A. Chakraborty, and D. Khastgir, "Measurement of ac conductivity and dielectric properties of flexible conductive styrene-butadiene rubber-carbon black composites," *Journal of Applied Polymer Science*, vol. 104, pp. 986–995, 2007.

[110] S. Wang, P. Wang, and T. Ding, "Piezoresistivity of silicone-rubber/carbon black composites excited by ac electrical field," *Jounal of Applied Polymer Science*, vol. 113, pp. 337–341, 2009.

[111] K. J. Loh, J. P. Lynch, B. S. Shim, and N. A. Kotov, "Tailoring piezoresistive sensitivity of multilayer carbon nanotube composite strain sensors," *Journal of Intelligent Material Systems and Structures*, vol. 19, pp. 747–764, 2008.

[112] L. E. Helseth, "Electrical impedance spectroscopy of multiwall carbon nanotube-pdms composites under compression," *Mater. Res. Express*, vol. 5, p. 105002, 2018.

[113] I. Kang, M. J. Schulz, J. H. Kim, V. Shanov, and D. Shi, "A carbon nanotube strain sensor for structural health monitoring," *Smart Materials and Structures*, vol. 15, pp. 737–748, 2006.

[114] J. Druyvesteyn, "The variation of the resistivity of some metals with elastic deformation," *Physica*, vol. 16, 1951.

[115] C. S. Smith, "Piezoresistance effect in germanium and silicon," *Physical Review*, vol. 94, 1954.

[116] P. Gruener, Y. Zhao, and M. Schagerl, "Charaterization of the spatial elastoresistivity of inkjet-printed carbon nanotube thin film for strain-state sensing," *Proc. Of SPIE*, vol. 10169, 2017.

[117] Y. Zhao, S. Gschossmann, M. Schagerl, P. Gruener, and C. Kralovec, "Characterization of the spatial elastoresistivity of inkjet-printed carbon nanotube thin film," *Smart Materials and Structures*, vol. 27, p. 105009, 2018.

[118] X. Ren, A. K. Chaurasia, A. I. Oliva-Aviles, J. J. Ku-Herrera, G. D. Seidel, and F. Aviles, "Modeling of mesoscale dispersion effect on the piezoresistivity of carbon nanotube-polymer nanocomposites via 3d computational multiscale micromechanics methods," *Smart Materials and Structures*, vol. 24, p. 065031, 2015.

[119] J. F. P. J. Abascal, S. R. Arridge, D. Atkinson, R. Horesh, L. Fabrizi, M. De Lucia, L. Horesh, R. H. Bayford, and D. S. Holder, "Use of anisotropic modelling in electrical impedance tomography; description of method and preliminary assessment of utility in imaging brain function in the adult human head," *NuroImage*, vol. 43, pp. 258–268, 2008.

[120] M. J. Jiang, Z. M. Dang, M. Bozlar, F. Miomandre, and J. Bai, "Broad-frequency dielectric behaviors in multiwalled carbon nanotube/rubber nanocomposites," *Journal of Applied Physics*, vol. 106, p. 084902, 2009.

[121] A. K. Jonscher, "The 'universal' dielectric response," *Nature*, vol. 267, pp. 673–679, 1977.

[122] T. N. Tallman and H. Hassan, "A network-centric perspective on the microscale mechanisms of complex impedance in carbon nanofiber-modified epoxy," *Composites Science and Technology*, vol. 181, p. 107669, 2019.

[123] "Pyrograp product inc," *Available: http://pyrografproducts.com/nanofiber.html*.

[124] "Standard test method for tensile properties of plastics," *ASTM Standard*, 2015.

[125] "Standard test method for shear properties of composite materials by v-notched rail shear method," *ASTM Standard*, 2020.

[126] T. N. Tallman and K. W. Wang, "An inverse methodology for calculating strains from conductivity changes in piezoresistive nanocomposites," *Smart Materials and Structures*, vol. 25, p. 115046, 2016.

[127] T. N. Tallman and H. Hassan, "A computational exploration of the effect of alignment and aspect ratio on alternating current conductivity in carbon-nanofiller-modified epoxy," *Journal of Intellignet Material Systems and Structures*, vol. 3, pp. 756–770, 2020.

[128] H. Hassan and T. N. Tallman, "Failure prediction in self-sensing nanocomposites via genetic algorithm-enabled piezoresistive inversion," *Structural Health Monitoring*, 2019.

[129] D. Smyl, S. Bossuyt, W. Ahmad, A. Vavilov, and D. Liu, "An overview of 38 least squares-based frameworks for structural damage tomography," *Structural Health Monitoring*, pp. 1–25, 2019.

[130] T. N. Tallman and J. A. Hernandez, "The effect of error and regularization norms on strain and damage identification via electrical impedance tomography in piezoresistive nanocomposites," *Nondestructive Testing Evaluation International*, vol. 91, pp. 156–163, 2017.

[131] D. S. Holder, *Electrical impedance tomography: methods, history and applications*. CRC Press, 2004.

[132] T. N. Tallman and D. J. Smyl, "Structural health and condition monitoring via electrical impedance tomography in self-sensing materials: a review," *Smart Materials and Structures*, 2020.

[133] H. A. Toprakci, S. K. Kalanadhabhatla, R. J. Spontak, and T. K. Ghosh, "Polymer nanocomposites containing carbon nanofibers as soft printable sensors exhibiting strain-reversible piezoresistivity," *Advanced Functional Materials*, vol. 23, no. 44, pp. 5536–5542, 2013.

[134] X. Liu, G. Su, Q. Guo, C. Lu, T. Zhou, C. Zhou, and X. Zhang, "Hierarchically structured self-healing sensors with tunable positive/negative piezoresistivity," *Advanced Functional Materials*, vol. 28, no. 15, p. 1706658, 2018.

[135] Z. Qian, A. E. Bowden, D. Zhang, J. Wan, W. Liu, X. Li, D. Baradoy, and D. T. Fullwood, "Inverse piezoresistive nanocomposite sensors for identifying human sitting posture," *Sensors*, vol. 18, no. 6, p. 1745, 2018.

[136] E. Garcia-Macias, A. Downey, A. D'Alessandro, R. Castro-Triguero, S. Laflamme, and F. Ubertini, "Enhanced lumped circuit model for smart nanocomposite cement-based sensors under dynamic compressive loading conditions," *Sensors and Actuators A: Physical*, vol. 260, pp. 45–57, 2017.

[137] C. Zhao, W. Yuan, H. Liu, B. Gu, N. Hu, N. Y. Alamusi, and F. Jia, "Equivalent circuit model for the strain sensing characteristics of multi-walled carbon nanotube/polyvinylidene fluoride films in alternating current circuit," *Carbon*, vol. 2018, pp. 585–591, 2018.

[138] C. Zhao, W. Yuan, Y. Zhao, N. Hu, B. Gu, H. Liu, and N. Y. Alamusi, "Unified equivalent circuit model for carbon nanotube-based nanocomposites," *Nanotechnology*, vol. 29, p. 305503, 2018.

[139] P. J. Burke, "An rf circuit model for carbon nanotubes," *IEEE Transactions on Nanotechnology*, vol. 2, no. 1, pp. 55–58, 2003.

[140] J. G. Simmons, "Generalized formula for the electric tunnel effect between similar electrodes separated by a thin insulating film," *Journal of Applied Physics*, vol. 34, pp. 1793–1803, 1963.

[141] D. Smyl, "Electrical tomography for characterizing transport properties in cement-based materials: A review," *Construction and Building Materials*, vol. 244, p. 118299, 2020.

[142] V. Mosser, J. Suski, J. Goss, and E. Obermeier, "Piezoresistive pressure sensors based on polycrystalline silicon," *Sensors and Actuators A: Physical*, vol. 28, no. 2, pp. 113–132, 1991.

[143] S. Khan and L. Lorenzelli, "Recent advances of conductive nanocomposites in printed and flexible electronics," *Smart Materials and Structures*, vol. 26, no. 8, p. 083001, 2017.

[144] S. Wang and D. Chung, "Piezoresistivity in continuous carbon fiber polymer-matrix composite," *Polymer Composites*, vol. 21, no. 1, pp. 13–19, 2000.

[145] S. Wen and D. Chung, "Piezoresistivity in continuous carbon fiber cement-matrix composite," *Cement and Concrete Research*, vol. 29, no. 3, pp. 445–449, 1999.

[146] S. Stassi, V. Cauda, G. Canavese, and C. F. Pirri, "Flexible tactile sensing based on piezoresistive composites: A review," *Sensors*, vol. 14, no. 3, pp. 5296–5332, 2014.

APPENDICES

A. DETAILED FORMULATION OF THE COMPLETE ELECTRODE MODEL BOUNDARY CONDITIONS

A.1 Introduction

In this appendix, the background of the finite element method (FEM) code for steady-state diffusion and the formulation of complete electrode model (CEM) boundary conditions in three dimensions are described. For the development of FEM code, conductivity is assumed to be a symmetric second-order tensor. Linear tetrahedral elements were used. Repeated indices in the subscripts indicate summation over the dimension of the problem unless accompanied by an explicit summation operator. And, superscripts are generally reserved for nodal or element numbers. As stated in Chapter 4, CEM boundary conditions add an additional degree of freedom for the voltage of each electrode, treat electrodes as being perfectly conducting (and hence at a constant voltage), and take into account domain-to-electrode contact impedance.

A.2 Formulation of Steady-State Diffusion Finite Element Simulation

Steady-state diffusion is governed by Laplace's equation as shown below.

$$-\frac{\partial j_i}{\partial x_i} = \frac{\partial}{\partial x_i}\sigma_{ij}\frac{\partial \phi}{\partial x_j} = f \tag{A.1}$$

Above, j_i is the current density distribution, σ_{ij} is the conductivity tensor (related to resistivity as $\sigma_{ij} = \rho_{ij}^{-1}$), ϕ is the domain potential, and f is an internal current source. Current is also only allowed to flow through the electrodes (i.e. no current flows through the boundaries) as described in the following equations.

$$\int_{E_l} \sigma_{ij} \frac{\partial \phi}{\partial x_i} n_j \, \mathrm{d}S_l = I_l \tag{A.2}$$

$$\sigma_{ij} \frac{\partial \phi}{\partial x_i} n_j = 0 \text{ off } \cup_{l=1}^{L} E_l \tag{A.3}$$

Above, E_l is the area of the lth electrode, n_j is an outward pointing normal vector, I is the current through the electrode, and L is the total number of electrodes. Conservation of charge requires that the following condition holds.

$$\sum_{l=1}^{L} I_l = 0 \tag{A.4}$$

Next, the weak form shown of equation (A.1) is formed by multiplying with a weighting function, ψ that satisfies the Dirichlet boundary conditions on both side of the equation and integrating over the domain, Ω, as shown in equation (A.5).

$$\int_{\Omega} \psi \frac{\partial}{\partial x_i} \sigma_{ij} \frac{\partial \phi}{\partial x_j} \, \mathrm{d}\Omega = \int_{\Omega} \psi f \, \mathrm{d}\Omega \tag{A.5}$$

Assuming that the internal source is zero ($f = 0$), equation (A.5) can be rearranged as equation (A.6) with vector identity $\nabla(hg) = (\nabla h)g + h(\nabla g)$.

$$\int_{\Omega} \frac{\partial}{\partial x_i} \psi \sigma_{ij} \frac{\partial \phi}{\partial x_j} \, \mathrm{d}\Omega - \int_{\Omega} \frac{\partial \psi}{\partial x_i} \sigma_{ij} \frac{\partial \phi}{\partial x_j} \, \mathrm{d}\Omega = 0 \tag{A.6}$$

And equation (A.6) becomes equation (A.7) with the divergence theorem.

$$\int_{\Omega} \frac{\partial \psi}{\partial x_i} \sigma_{ij} \frac{\partial \phi}{\partial x_j} \, \mathrm{d}\Omega = \int_{\partial\Omega} \psi \sigma_{ij} \frac{\partial \phi}{\partial x_i} n_j \, \mathrm{d}S = \int_{\Gamma} \sigma_{ij} \frac{\partial \phi}{\partial x_i} n_j \psi \, \mathrm{d}S \tag{A.7}$$

Above, Γ is the union of the electrode areas. Next, substitute the CEM boundary conditions shown in equation (4.3) into equation (A.7). After doing this, the following equation can be obtained.

$$\int_{\Omega} \frac{\partial \psi}{\partial x_i} \sigma_{ij} \frac{\partial \phi}{\partial x_j} \, \mathrm{d}\Omega = \sum_{l=1}^{L} \int_{E_l} \frac{1}{z_l} (V_l - \phi) \psi \, \mathrm{d}S_l \tag{A.8}$$

After discretizing the entire domain with elements, equation (A.8) can be rewritten as equation (A.9), where e is the element number, and ϕ_e and ψ_e are defined element-wised as shown in equation (A.10) and (A.11). Here, A is the nodal number, d_e^A is the potential solution on the Ath node of the eth element and c_e^A is the variation of the Ath node of the eth element. $\sum_e$ implies assembly over all of the elements in the discretization. w^A is the Ath of total N interpolation functions.

$$\sum_e \int_{\Omega_e} \frac{\partial \psi_e}{\partial x_i} \sigma_{ij} \frac{\partial \phi_e}{\partial x_j} \, \mathrm{d}\Omega_e = \sum_e \sum_{l=1}^{L} \int_{\partial \Omega_e} \frac{1}{z_l} (V_l - \phi_e) \psi_e \, \mathrm{d}S_e \tag{A.9}$$

$$\phi_e = \sum_{A=1}^{N} w^A d_e^A \tag{A.10}$$

$$\psi_e = \sum_{A=1}^{N} w^A c_e^A \tag{A.11}$$

A.3 Formulation of Complete Electrode Model Boundary Conditions

Regarding the left hand side of equation (A.9) for the eth element, equation (A.12) can be obtained by applying equation (A.10) and (A.11) to equation (A.9).

$$\int_{\Omega_e} \frac{\partial \psi_e}{\partial x_i} \sigma_{ij} \frac{\partial \phi_e}{\partial x_j} \, \mathrm{d}\Omega_e = \sum_{A=1}^{N} \sum_{B=1}^{N} c_e^A \int_{\Omega_e} \frac{\partial w^A}{\partial x_i} \sigma_{ij} \frac{\partial w^B}{\partial x_j} \, \mathrm{d}\Omega_e \, d_e^B \tag{A.12}$$

Here, d_e^A and c_e^A are taken out of the integral since they are constant with respect to Ω_e. In order to effectively solve equation (A.12), interpolation functions can be defined on an isoparametric domain where x_i^A is the ith coordinate for the Ath node and ζ is defined on the range of 0 to 1.

$$x_i = \sum_{A=1}^{N} w^A(\zeta) x_i^A \tag{A.13}$$

Next, using the chain rule, $\frac{\partial w^A}{\partial x_i} = \frac{\partial w^A}{\partial \zeta_j} \frac{\partial \zeta_j}{\partial x_i}$, equation (A.12) can be rewritten as the following equation.

$$\int_{\Omega_e} \frac{\partial \psi_e}{\partial x_i} \sigma_{ij} \frac{\partial \phi_e}{\partial x_j} \, \mathrm{d}\Omega_e = \sum_{A=1}^{N} \sum_{B=1}^{N} c_e^A \int_{\Omega_{e_\zeta}} \frac{\partial w^A}{\partial \zeta_k} \frac{\partial \zeta_k}{\partial x_i} \sigma_{ij} \frac{\partial w^B}{\partial \zeta_l} \frac{\partial \zeta_l}{\partial x_j} \, \mathrm{d}\Omega_e \, d_e^B \tag{A.14}$$

Note that numerical quadrature can be used with Lagrange polynomials to evaluate this integral because an isoparametric domain is selected for this simulation. Herein, four-node linear tetrahedral elements were used with $w^1 = \zeta_1$, $w^2 = \zeta_2$, $w^3 = \zeta_3$, and $w^4 = 1 - \zeta_1 - \zeta_2 - \zeta_3$. $\det \left| \frac{\partial x_i}{\partial \zeta_j} \right|$ is also included in the integrand in the isoparametric mapping as shown in equation (A.14) as the following equation.

$$\int_{\Omega_e} \frac{\partial \psi_e}{\partial x_i} \sigma_{ij} \frac{\partial \phi_e}{\partial x_j} \, \mathrm{d}\Omega_e = \sum_{A=1}^{N} \sum_{B=1}^{N} c_e^A \int_{\Omega_{e_\zeta}} \frac{\partial w^A}{\partial \zeta_k} \frac{\partial \zeta_k}{\partial x_i} \sigma_{ij} \frac{\partial w^B}{\partial \zeta_l} \frac{\partial \zeta_l}{\partial x_j} \det \left| \frac{\partial x_m}{\partial \zeta_n} \right| \, \mathrm{d}\Omega_{e_\zeta} \, d_e^B \tag{A.15}$$

Above, Ω_{e_ζ} is the isoparametric domain of the eth element. The integration shown above can be evaluated by summing weighted polynomials obtained by quadrature points as $\int_{\Omega_{e_\zeta}} f(\zeta_i) \, \mathrm{d}\Omega_{e_\zeta} = \sum_i^I p_i f(\zeta_i)$, where I is the total number of quadrature points (i.e. integrand evaluations), p_i is the corresponding quadrature weight, and ζ_i is again the location of the ith quadrature point in the domain. Since interpolation functions are already given above, equation (A.15) can be rewritten as the following equation.

$$\int_{\Omega_e} \frac{\partial \psi_e}{\partial x_i} \sigma_{ij} \frac{\partial \phi_e}{\partial x_j} \, \mathrm{d}\Omega_e = \sum_{A=1}^{N} \sum_{B=1}^{N} c_e^A k_e^{AB} d_e^B = \begin{bmatrix} c_e^1 & c_e^2 & \cdots & c_e^N \end{bmatrix} \boldsymbol{k}_e \begin{bmatrix} d_e^1 \\ d_e^2 \\ \vdots \\ d_e^N \end{bmatrix} \tag{A.16}$$

Above, k_e^{AB} is called as the local steady-state diffusion stiffness matrix of the eth element. This can be used to form $\boldsymbol{A}_M$ shown in equation (4.5) by assembling all of the local stiffness matrices which comprise the domain. Explicitly, evaluating the preceding integral equations yields the following local diffusion stiffness matrix for the eth element.

$$\boldsymbol{k}_e = \frac{1}{6}\begin{bmatrix} 1 & 0 & 0 \\ 0 & 1 & 0 \\ 0 & 0 & 1 \\ -1 & -1 & -1 \end{bmatrix} \begin{bmatrix} x_1^e - x_4^e & x_2^e - x_4^e & x_3^e - x_4^e \\ y_1^e - y_4^e & y_2^e - y_4^e & y_3^e - y_4^e \\ z_1^e - z_4^e & z_2^e - z_4^e & z_3^e - z_4^e \end{bmatrix}^{-1} \quad ... \\ ... \begin{bmatrix} \sigma_{11} & \sigma_{12} & \sigma_{13} \\ \sigma_{21} & \sigma_{22} & \sigma_{23} \\ \sigma_{31} & \sigma_{32} & \sigma_{33} \end{bmatrix} \begin{bmatrix} x_1^e - x_4^e & x_2^e - x_4^e & x_3^e - x_4^e \\ y_1^e - y_4^e & y_2^e - y_4^e & y_3^e - y_4^e \\ z_1^e - z_4^e & z_2^e - z_4^e & z_3^e - z_4^e \end{bmatrix}^{-T} \quad ... \\ ... \begin{bmatrix} 1 & 0 & 0 \\ 0 & 1 & 0 \\ 0 & 0 & 1 \\ -1 & -1 & -1 \end{bmatrix}^T \det \left| \begin{bmatrix} x_1^e - x_4^e & x_2^e - x_4^e & x_3^e - x_4^e \\ y_1^e - y_4^e & y_2^e - y_4^e & y_3^e - y_4^e \\ z_1^e - z_4^e & z_2^e - z_4^e & z_3^e - z_4^e \end{bmatrix} \right| \tag{A.17}$$

Here, x_i^e, y_i^e, and z_i^e are the x-, y-, and z-direction nodal coordinates of the ith node of the eth element. Next, $\boldsymbol{A}_Z$ and $\boldsymbol{A}_W$ in equation (4.5) can also be determined by separating the rest of the integrals in equation (A.9) as the follows.

$$\sum_e \int_{\partial\Omega_e} \frac{1}{z_l}(V_l - \phi_e)\psi_e \, \mathrm{d}S_e = \sum_e \left(- \int_{\partial\Omega_e} \frac{1}{z_l}\phi_e\psi_e \, \mathrm{d}S_e + \int_{\partial\Omega_e} \frac{1}{z_l} V_l \psi_e \, \mathrm{d}S_e \right) \tag{A.18}$$

The first term of the right hand side of equation (A.18) is again expressed by summing weighted polynomials as shown in equation (A.19). As previously done for the steady-state diffusion stiffness matrix, the variation and potential solution are taken out from the integrals, and equation (A.10) and (A.11) are plugged back into ϕ_e and ψ_e of the first term of the right hand side of equation (A.18). However, it is important to note that the dimension of the interpolation functions for CEM matrices of $\boldsymbol{A}_Z$ are one degree lower than the degree of interpolation function of $\boldsymbol{A}_M$ because they are related to the electrodes. That is, $\boldsymbol{A}_M$ uses three-dimensional interpolation because the domain is three-dimensional, but the other CEM matrices use two-dimensional functions because the electrodes are two-dimensional. Hence,

the CEM interpolation functions are $w_1 = \zeta_1$, $w_2 = \zeta_2$, and $w_3 = 1 - \zeta_1 - \zeta_2$. In order to generate $\boldsymbol{A}_Z$, matrix multiplication is again used for the easiness as shown equation (A.20). Here, $\boldsymbol{A}_Z^{e\,l}$ represents $\boldsymbol{A}_Z$ matrix of the eth element in the lth electrode, and A^e is the the triangular area of eth element in the electrodes. This can be solved as shown in equation (A.21). Like $\boldsymbol{A}_M$, $\boldsymbol{A}_Z^{el}$ is also assembled to global $\boldsymbol{A}_Z$ later in section **??**.

$$\begin{aligned}\int_{\Omega_e} \frac{1}{z_l}\phi_e\psi_e \,\mathrm{d}S_e &= \sum_{A=1}^{N}\sum_{B=1}^{N} c_e^A \int_{\Omega_e} \frac{1}{z_l} w^A w^B \,\mathrm{d}S_e \, d_e^B \\ &= \begin{bmatrix} c_e^1 & c_e^2 & \cdots & c_e^N \end{bmatrix} \boldsymbol{A}_Z^{e\,l} \begin{bmatrix} d_e^1 \\ d_e^2 \\ \vdots \\ d_e^N \end{bmatrix}\end{aligned} \tag{A.19}$$

$$\begin{aligned}\boldsymbol{A}_Z^{e\,l} &= \int_0^1 \int_0^{1-\zeta_1} \frac{2A^e}{z_l} \begin{bmatrix} \zeta_1^2 & \zeta_1\zeta_2 & \zeta_1(1-\zeta_1-\zeta_2) \\ \zeta_1\zeta_2 & \zeta_2^2 & \zeta_2(1-\zeta_1-\zeta_2) \\ \zeta_1(1-\zeta_1-\zeta_2) & \zeta_2(1-\zeta_1-\zeta_2) & (1-\zeta_1-\zeta_2)^2 \end{bmatrix} \mathrm{d}\zeta_2 \,\mathrm{d}\zeta_1 \\ &= \frac{A^e}{12 z_l} \begin{bmatrix} 2 & 1 & 1 \\ 1 & 2 & 1 \\ 1 & 1 & 2 \end{bmatrix}\end{aligned} \tag{A.20}$$

$$A^e = \frac{1}{2} \det \left| \begin{bmatrix} x_1^e - x_3^e & x_2^e - x_3^e \\ y_1^e - y_3^e & y_2^e - y_3^e \end{bmatrix} \right| \tag{A.21}$$

Next, to determine $\boldsymbol{A}_W^{e\,l}$, the second term of the right hand side of equation (A.18) is calculated as previously done for $\boldsymbol{A}_Z^{e\,l}$. The steps are the same as the procedure of determining $\boldsymbol{A}_Z^{e\,l}$ as shown in equations (A.22) and (A.23). As done for $\boldsymbol{A}_M$ and $\boldsymbol{A}_Z$, the local $\boldsymbol{A}_W^{e\,l}$ is assembled to the global $\boldsymbol{A}_W$ later in section **??**. Again, note that A^e is the area of the eth element in the electrode as shown in equation (A.21).

$$
\begin{aligned}
-\int_{\Omega_e} \frac{1}{z_l}\psi_e V_l \, \mathrm{d}S_e &= \sum_{A=1}^{N} c_e^A \int_{\Omega_e} \frac{1}{z_l} w^A \, \mathrm{d}S_e \; V_l d_e^B \\
&= \begin{bmatrix} c_e^1 & c_e^2 & \cdots c_e^N \end{bmatrix} \boldsymbol{A}_W^{e\,l} V_l
\end{aligned}
\tag{A.22}
$$

$$
\begin{aligned}
\boldsymbol{A}_W^{e\,l} &= -\int_0^1 \int_0^{1-\zeta_1} \frac{2A^e}{z_l} \begin{bmatrix} \zeta_1 \\ \zeta_2 \\ 1-\zeta_1-\zeta_2 \end{bmatrix} \mathrm{d}\zeta_2 \, \mathrm{d}\zeta_1 \\
&= -\frac{A^e}{3z_l} \begin{bmatrix} 1 \\ 1 \\ 1 \end{bmatrix}
\end{aligned}
\tag{A.23}
$$

Lastly, $\boldsymbol{A}_D$ can be simply determined by placing E_l/z_l in the diagonal components of $\boldsymbol{A}_D$ and zeros in the off-diagonal components in $\boldsymbol{A}_D$ matrix, where the size of $\boldsymbol{A}_D$ is the number of elements in electrodes $\times$ the number of elements in electrodes as shown in equation (4.9). However, for the derivation of $\boldsymbol{A}_D$, the total current should be considered and conservation of charges shown in equation (A.4) needs to be applied. The current through the lth electrode is shown below.

$$
I_l = \int_{E_l} \frac{1}{z_l}(V_l - \phi) \, \mathrm{d}S = \frac{1}{z_l} E_l V_l - \int_{E_l} \frac{1}{z_l} \phi \, \mathrm{d}S \tag{A.24}
$$

Above, it is assumed that contact impedance between the domain and the electrode and voltage on the electrode are constant. It can be recognized that the first term of the right hand side of equation (A.24) relates the electrode current and the electrode voltage by E_l/z_l as shown in the diagonal components of $\boldsymbol{A}_D$. The second term of the right hand side of equation (A.24) seems to be similar to the equation (A.22). Unlike equation (A.22), this part makes use of the potential solution, ϕ. This is because $\boldsymbol{A}_D$ accounts for the relation between the domain and the electrode voltage via $\boldsymbol{A}_W$

A.4 Matrix Assembly

The global $\boldsymbol{A}_M$, $\boldsymbol{A}_Z$, and $\boldsymbol{A}_W$ matrices can be obtained by assembling the local $\boldsymbol{k}_e$, $\boldsymbol{A}_Z^{e\,l}$, and $\boldsymbol{A}_W^{e\,l}$ matrices. The following steps only show the matrix assembly for $\boldsymbol{A}_M$ because the assembly procedure is much the same for the others. For this, the local variation and potential solution are first described as the global variation and potential solution such as $\boldsymbol{c} = [c^1\ c^2\ c^3\ \cdots\ c^i\ \cdots\ c^I]$ and $\boldsymbol{d} = [d^1\ d^2\ d^3\ \cdots\ d^i\ \cdots\ d^I]$, where c^i and d^i represent the variation and potential solution of the ith node among total I nodes, respectively. Then, assembly of the local stiffness matrix over the entire elements can be calculated as the following.

$$\sum_e \int_{\Omega_e} \frac{\partial \psi_e}{\partial x_i} \sigma_{ij} \frac{\partial \phi_e}{\partial x_j}\, \mathrm{d}\Omega_e = \boldsymbol{c}^T \boldsymbol{A}_M \boldsymbol{d} \tag{A.25}$$

In order to appropriately assemble the local stiffness matrix, the entries of the local stiffness matrix must be located in the right place according the location of the global variation and potential solution. However, some components may be located in the same entry since some elements share edges. In such cases, the entries from different elements are summed up. In order to conveniently visualize the assembly procedure, the following example is provided. Consider the local stiffness matrix of an arbitrary element such as the eth element as shown in equation (A.26). Next, consider the local stiffness matrix of the $(e+1)$th element as shown in equation (A.27). Assume that these elements share the nodal points. Specifically, the eth element and the $(e+1)$th element share one edge such as the side between the second and the third nodal points of the eth and the side between the first and the second nodal points of the $(e+1)$th element.

$$\boldsymbol{c}_e^T \boldsymbol{A}_M^e \boldsymbol{d}_e = \begin{bmatrix} c_e^1 & c_e^2 & c_e^3 \end{bmatrix} \begin{bmatrix} k_e^{11} & k_e^{12} & k_e^{13} \\ k_e^{21} & k_e^{22} & k_e^{23} \\ k_e^{31} & k_e^{32} & k_e^{33} \end{bmatrix} \begin{bmatrix} d_e^1 \\ d_e^2 \\ d_e^3 \end{bmatrix} \tag{A.26}$$

$$\boldsymbol{c}_{e+1}^{T}\boldsymbol{A}_{M}^{e+1}\boldsymbol{d}_{e}=\begin{bmatrix}c_{e+1}^{1} & c_{e+1}^{2} & c_{e+1}^{3}\end{bmatrix}\begin{bmatrix}k_{e+1}^{11} & k_{e+1}^{12} & k_{e+1}^{13}\\ k_{e+1}^{21} & k_{e+1}^{22} & k_{e+1}^{23}\\ k_{e+1}^{31} & k_{e+1}^{32} & k_{e+1}^{33}\end{bmatrix}\begin{bmatrix}d_{e+1}^{1}\\ d_{e+1}^{2}\\ d_{e+1}^{3}\end{bmatrix} \tag{A.27}$$

Next, assume that the local variation and potential solution of the eth element corresponds to the global system as follows.

$$\begin{bmatrix}c_{e}^{1} & c_{e}^{2} & c_{e}^{3}\end{bmatrix}\mapsto\begin{bmatrix}c^{i-1} & c^{i} & c^{i+1}\end{bmatrix}$$

$$\begin{bmatrix}d_{e}^{1} & d_{e}^{2} & d_{e}^{3}\end{bmatrix}\mapsto\begin{bmatrix}d^{i-1} & d^{i} & d^{i+1}\end{bmatrix}$$

And, assume that the local variation and potential solution of the $(e+1)$th element corresponds to the global system as the following.

$$\begin{bmatrix}c_{e+1}^{1} & c_{e+1}^{2} & c_{e+1}^{3}\end{bmatrix}\mapsto\begin{bmatrix}c^{i} & c^{i+1} & c^{i+2}\end{bmatrix}$$

$$\begin{bmatrix}d_{e+1}^{1} & d_{e+1}^{2} & d_{e+1}^{3}\end{bmatrix}\mapsto\begin{bmatrix}d^{i} & d^{i+1} & d^{i+2}\end{bmatrix}$$

In such cases, the components of the local stiffness matrix will be combined as equation (A.28). That is, the components sharing the ith and the $(i+1)$th nodes in the global stiffness matrix will be summed up as shown in the (i,i), $(i,i+1)$, $(i+1,i)$, and $(i+1,i+1)$ entries in the global stiffness matrix in equation (A.28). As shown here, once the connectivity of the element is known, the global stiffness matrix can be simply assembled from the local stiffness matrix according to the algorithm herein provided. The fundamental algorithm for assembling $\boldsymbol{A}_Z$ and $\boldsymbol{A}_W$ is much the same. However, as described previously, the degree of freedom for $\boldsymbol{A}_Z$ and $\boldsymbol{A}_W$ is one degree lower than that for $\boldsymbol{A}_M$. Furthermore, the total number of assembly for $\boldsymbol{A}_Z$ and $\boldsymbol{A}_W$ is corresponding to the number of elements in the electrodes unlike that for $\boldsymbol{A}_M$ corresponding to the number of elements in the domain.

$$\boldsymbol{c}^T \boldsymbol{A}_M \boldsymbol{d} = \begin{bmatrix} \vdots \\ c_{i-1} \\ c_i \\ c_{i+1} \\ c_{i+2} \\ \vdots \end{bmatrix}^T \begin{bmatrix} \ddots & & & & & \\ & k_e^{11} & k_e^{12} & k_e^{13} & & \\ & k_e^{21} & k_e^{22}+k_{e+1}^{11} & k_e^{23}+k_{e+1}^{22} & k_{e+1}^{13} & \\ & k_e^{31} & k_e^{32}+k_{e+1}^{21} & k_e^{33}+k_{e+1}^{22} & k_{e+1}^{23} & \\ & & k_{e+1}^{31} & k_{e+1}^{32} & k_{e+1}^{33} & \\ & & & & & \ddots \end{bmatrix} \begin{bmatrix} \vdots \\ d_e^{i-1} \\ d_e^{i} \\ d_e^{i+1} \\ d_e^{i+2} \\ \vdots \end{bmatrix} \tag{A.28}$$

B. RAW IMPEDANCE DATA

This appendix provides the raw impedance data which are not included in Chapter 5 due to the redundancy of the plots. Again, the raw impedance magnitude and phase angle are plotted in terms of normal and shear strains. As the color goes from blue to red, both normal and shear strain increase. For each test and weight fraction, the raw impedance data plots exhibit similar trends and magnitudes. This appendix is provided in order to show the consistency of the experimental results. Note that significant noise is present in 0.5 wt.% CNF/epoxy specimens at low frequencies. On the contrary, clear trends can be seen in 1.0 and 1.5 wt.% CNF/epoxy specimens.

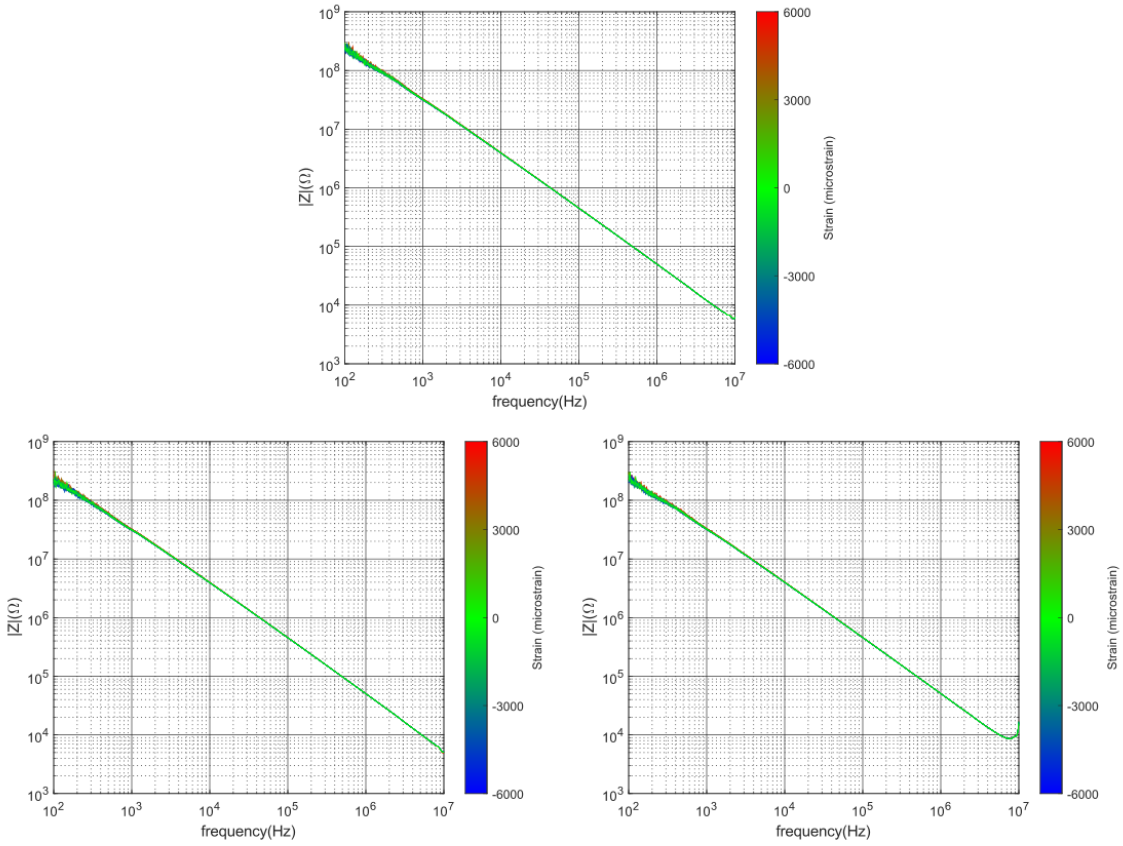

Fig. B.1. Raw impedance magnitude data for 0.5 wt.% CNF/epoxy dog-bone specimens (Top: Sample 1, Left: Sample 2, and Right: Sample 3.)

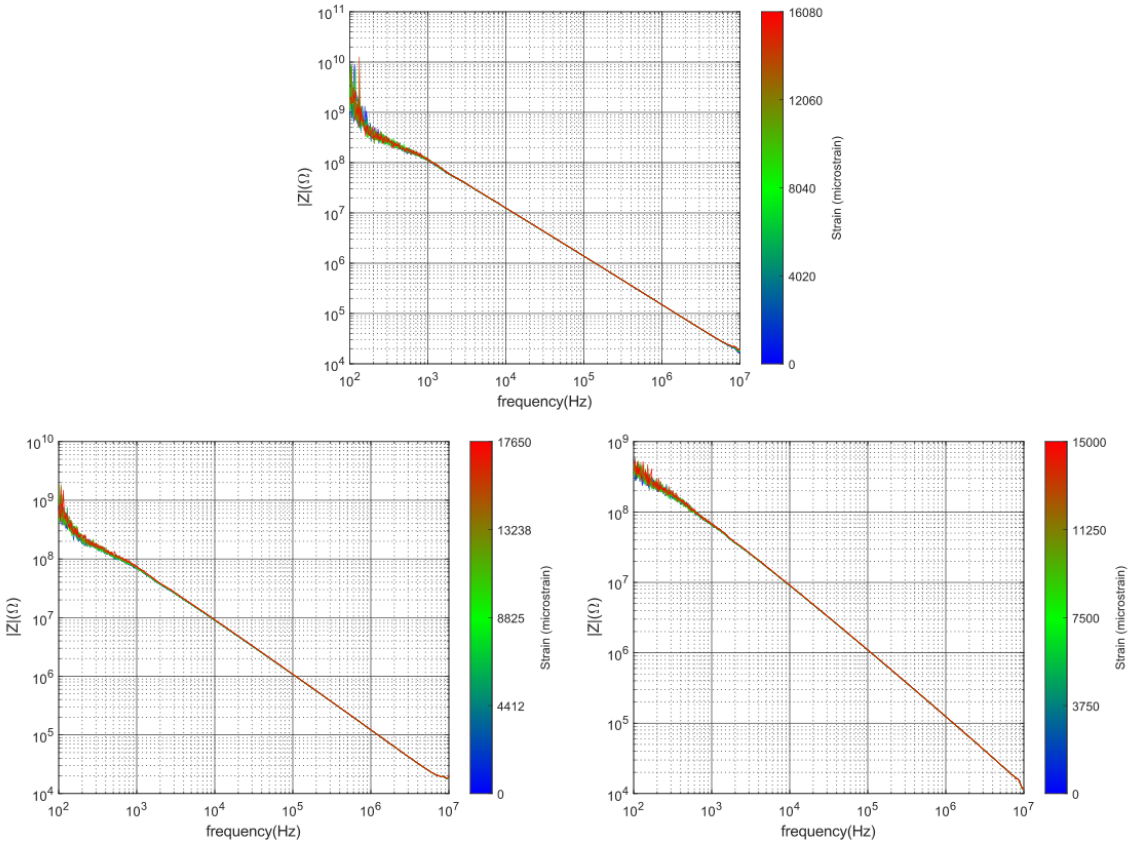

Fig. B.2. Raw impedance magnitude data for 0.5 wt.% CNF/epoxy v-notched specimens (Top: Sample 1, Left: Sample 2, and Right: Sample 3.)

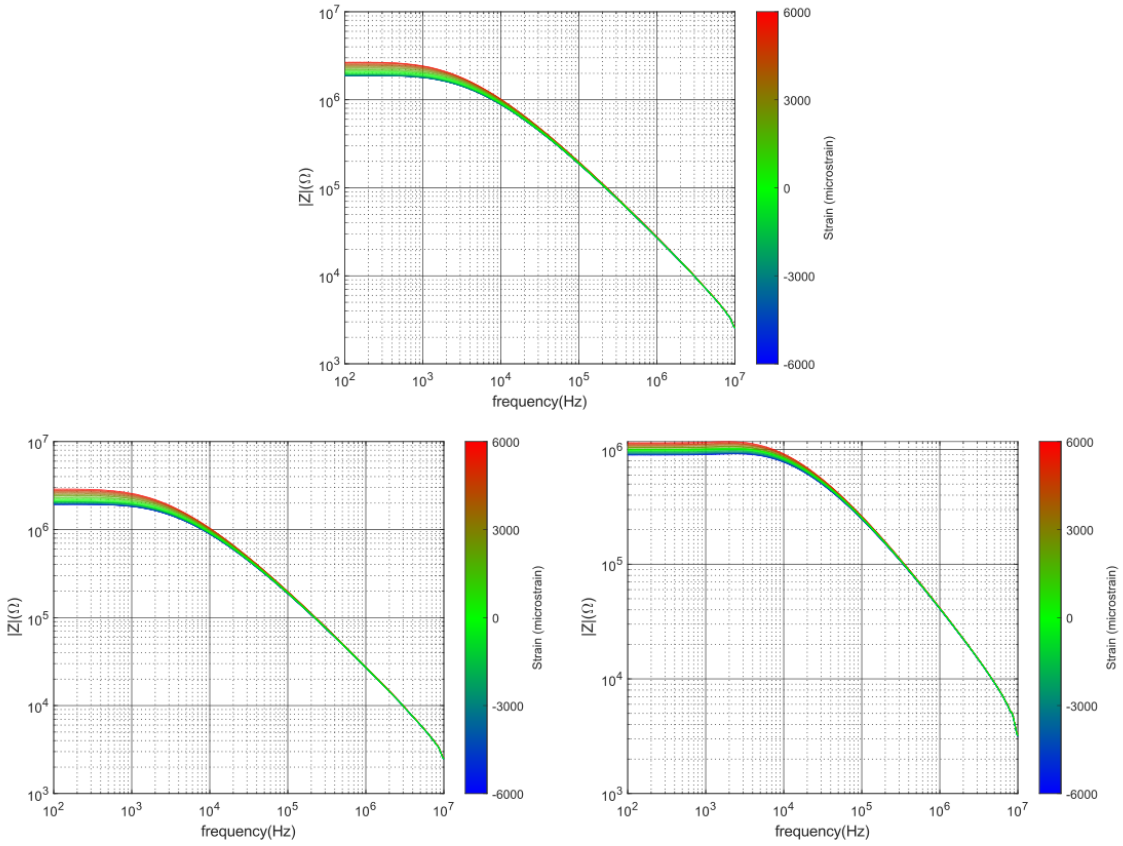

Fig. B.3. Raw impedance magnitude data for 1.0 wt.% CNF/epoxy dog-bone specimens (Top: Sample 1, Left: Sample 2, and Right: Sample 3.)

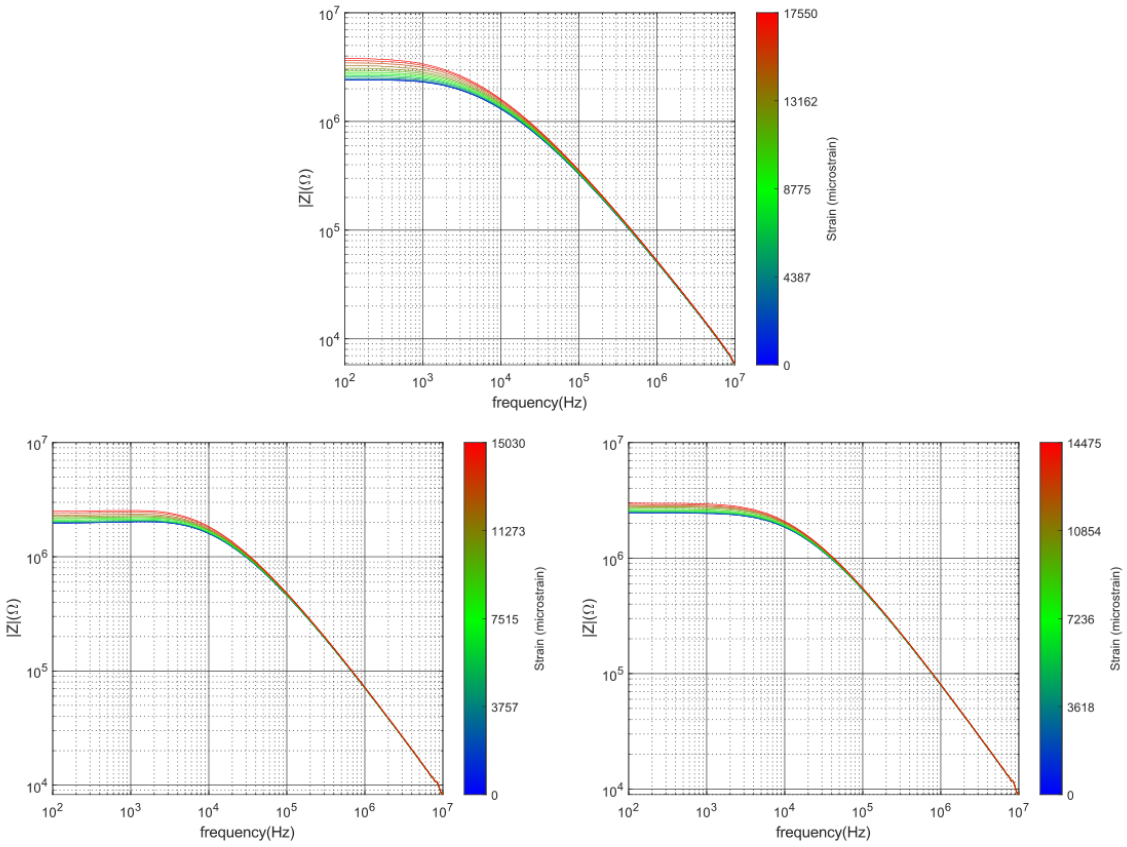

Fig. B.4. Raw impedance magnitude data for 1.0 wt.% CNF/epoxy v-notched specimens (Top: Sample 1, Left: Sample 2, and Right: Sample 3.)

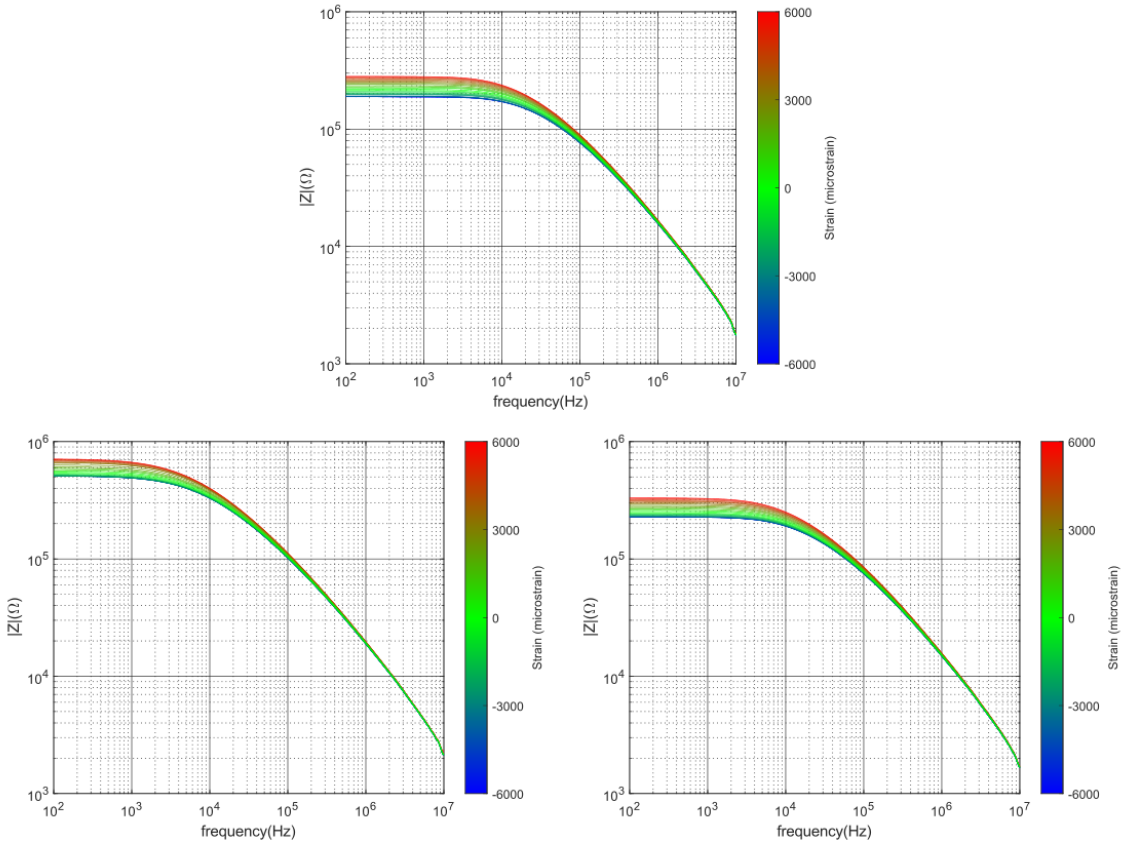

Fig. B.5. Raw impedance magnitude data for 1.5 wt.% CNF/epoxy dog-bone specimens (Top: Sample 1, Left: Sample 2, and Right: Sample 3.)

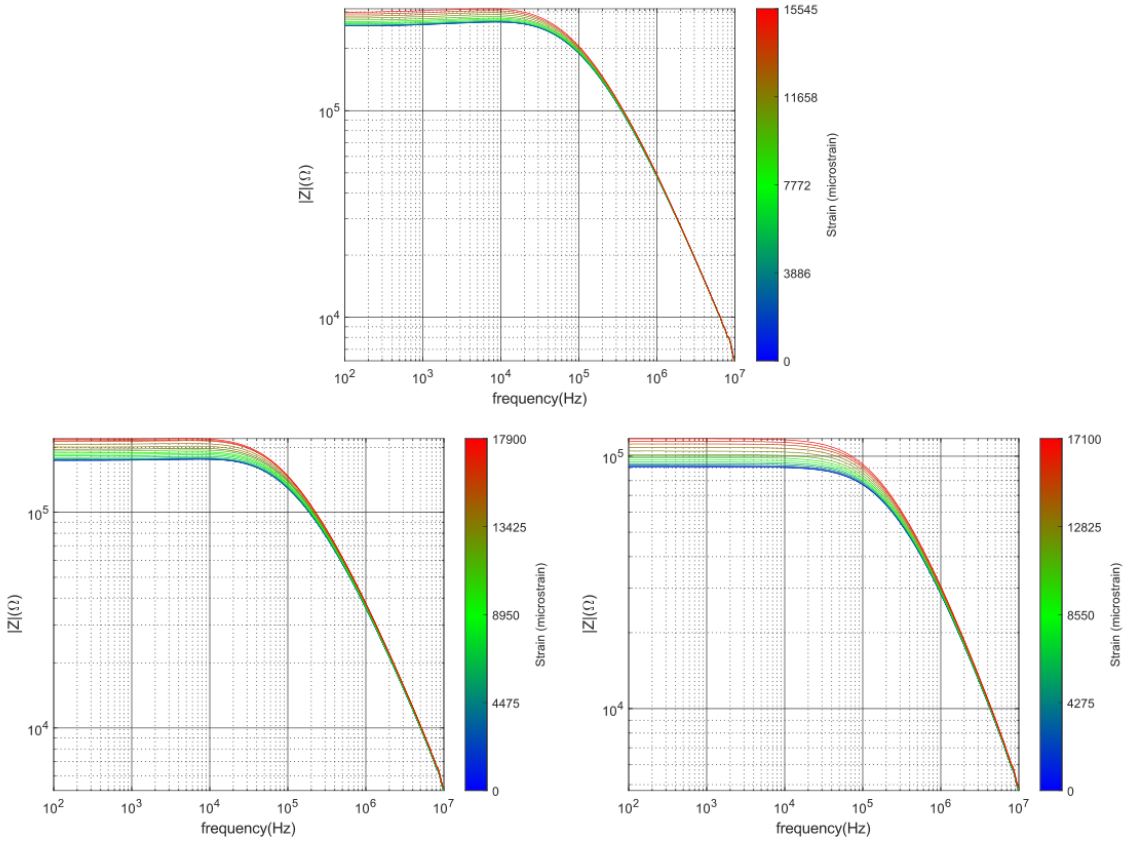

Fig. B.6. Raw impedance magnitude data for 1.5 wt.% CNF/epoxy v-notched specimens (Top: Sample 1, Left: Sample 2, and Right: Sample 3.)

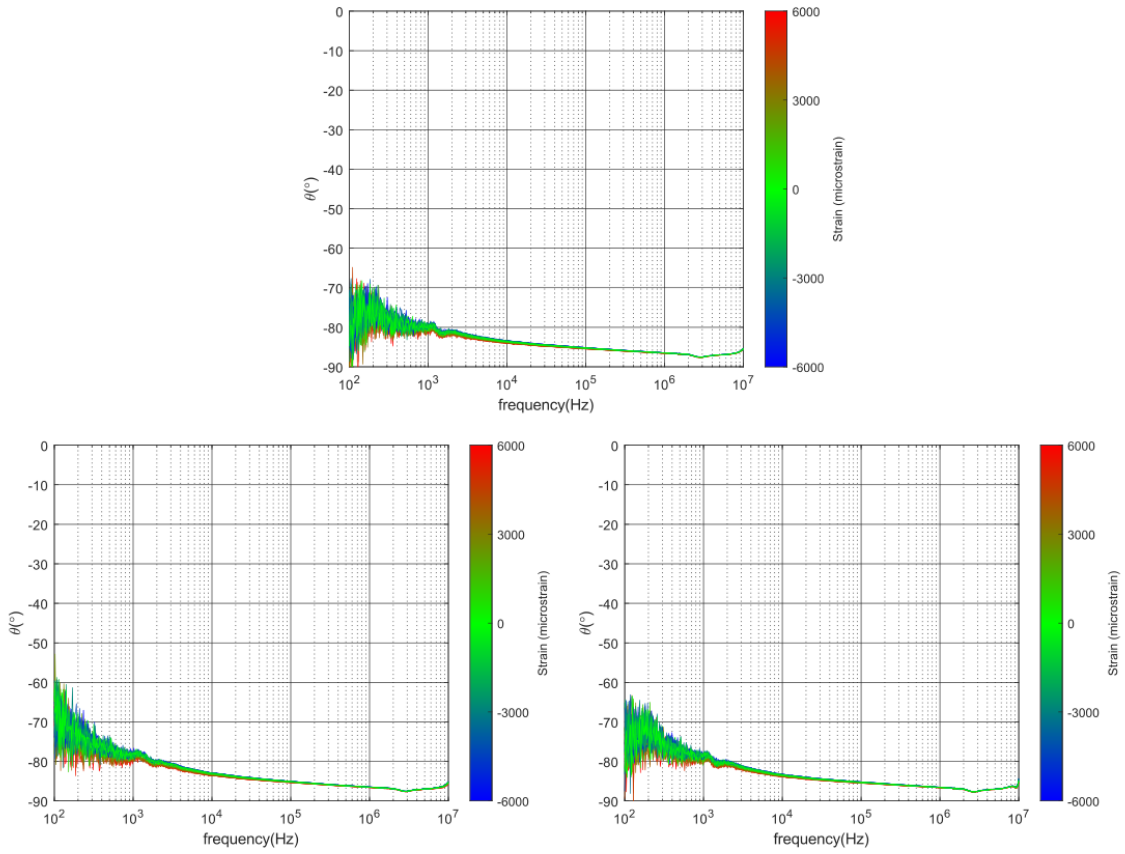

Fig. B.7. Raw phase angle data for 0.5 wt.% CNF/epoxy dog-bone specimens (Top: Sample 1, Left: Sample 2, and Right: Sample 3.)

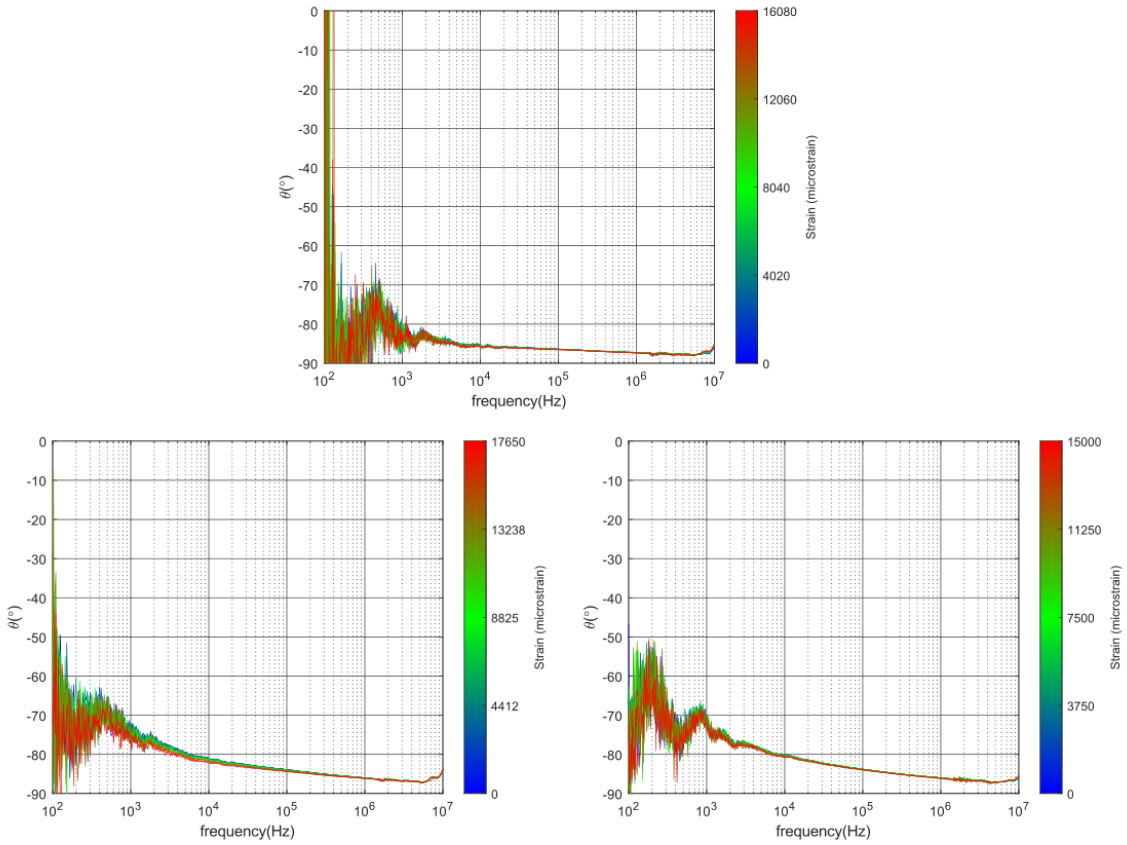

Fig. B.8. Raw phase angle data for 0.5 wt.% CNF/epoxy v-notched specimens (Top: Sample 1, Left: Sample 2, and Right: Sample 3.)

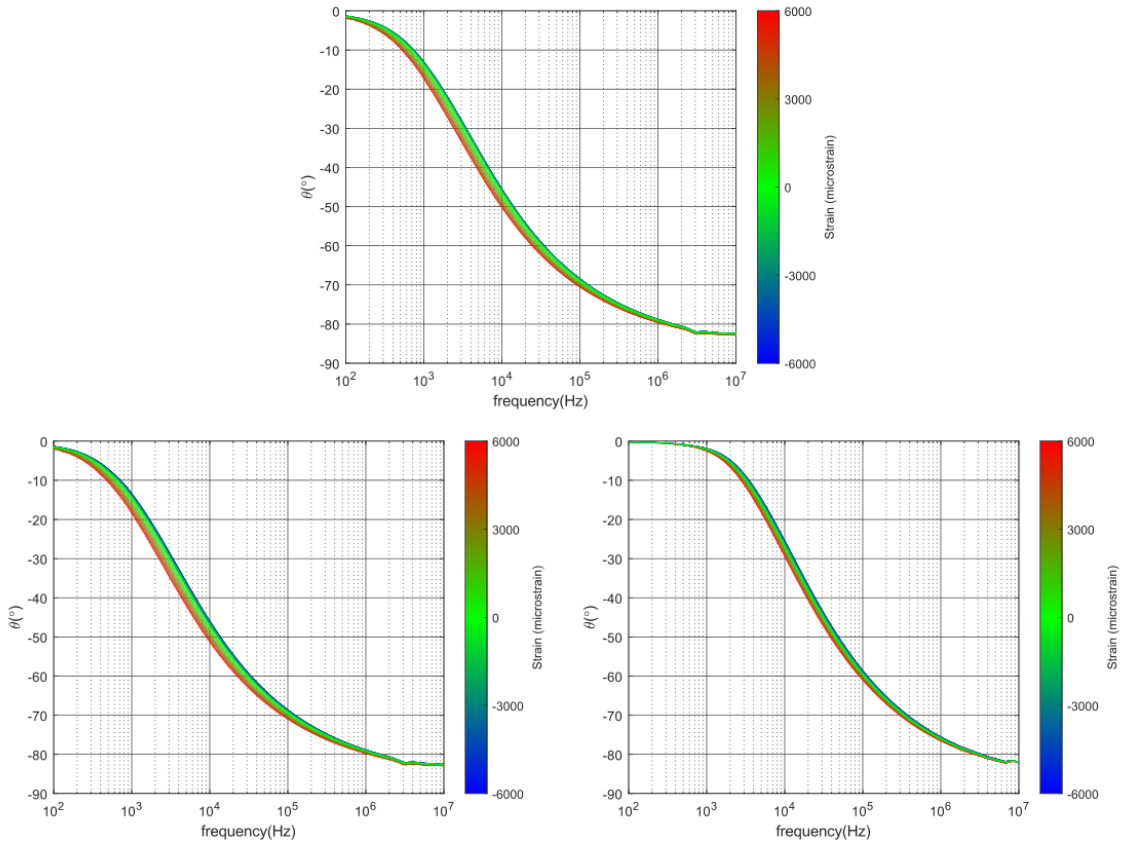

Fig. B.9. Raw phase angle data for 1.0 wt.% CNF/epoxy dog-bone specimens (Top: Sample 1, Left: Sample 2, and Right: Sample 3.)

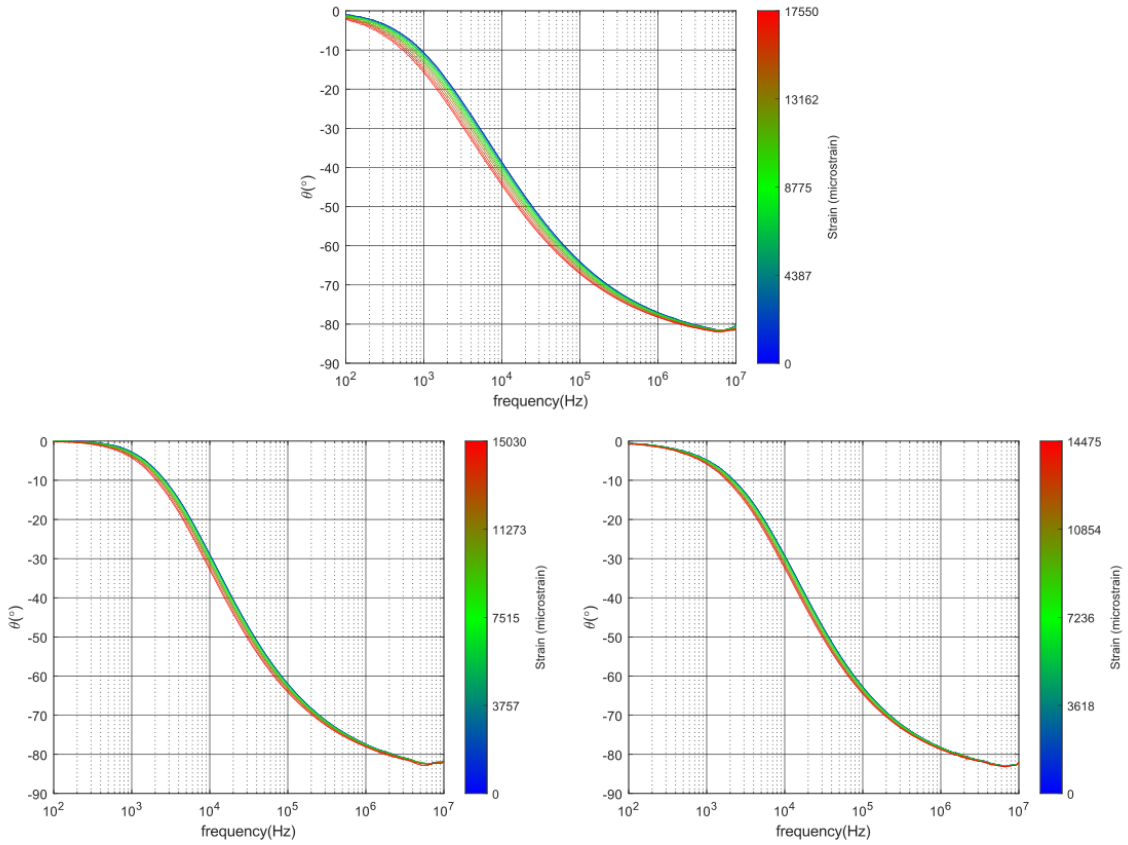

Fig. B.10. Raw phase angle data for 1.0 wt.% CNF/epoxy v-notched specimens (Top: Sample 1, Left: Sample 2, and Right: Sample 3.)

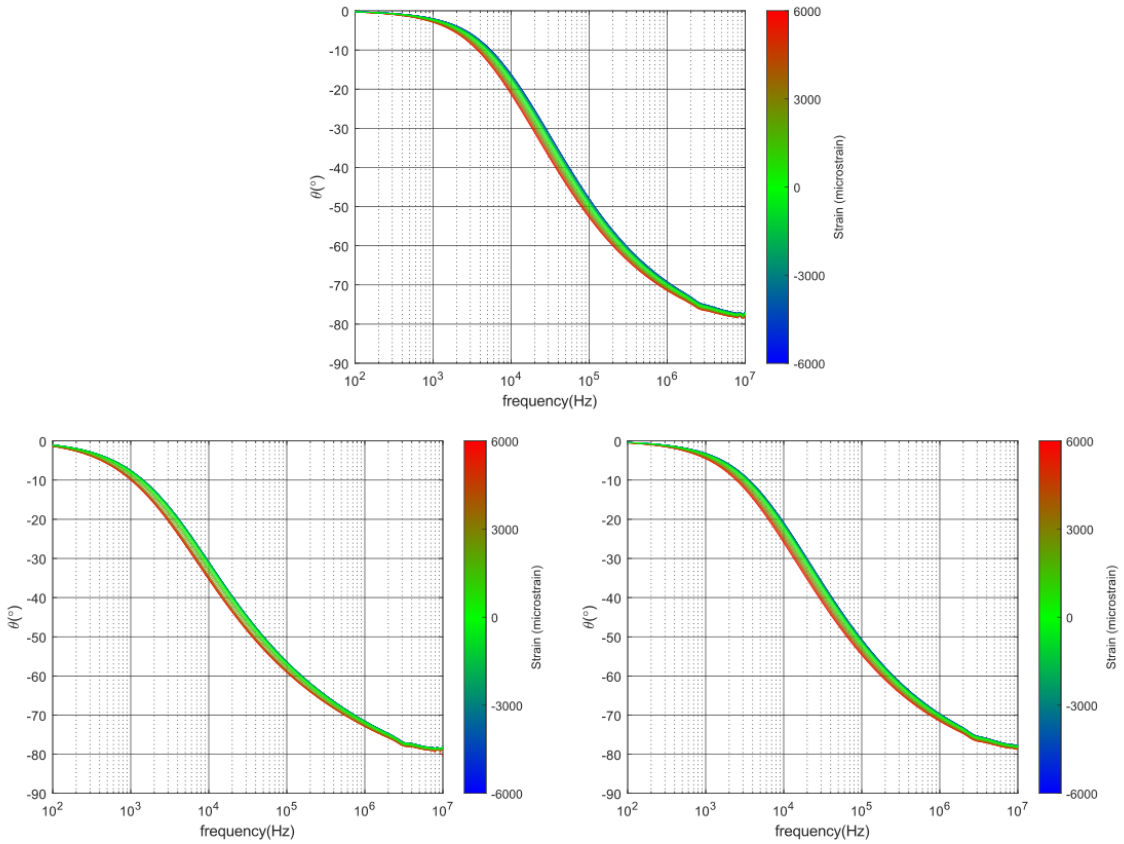

Fig. B.11. Raw phase angle data for 1.5 wt.% CNF/epoxy dog-bone specimens (Top: Sample 1, Left: Sample 2, and Right: Sample 3.)

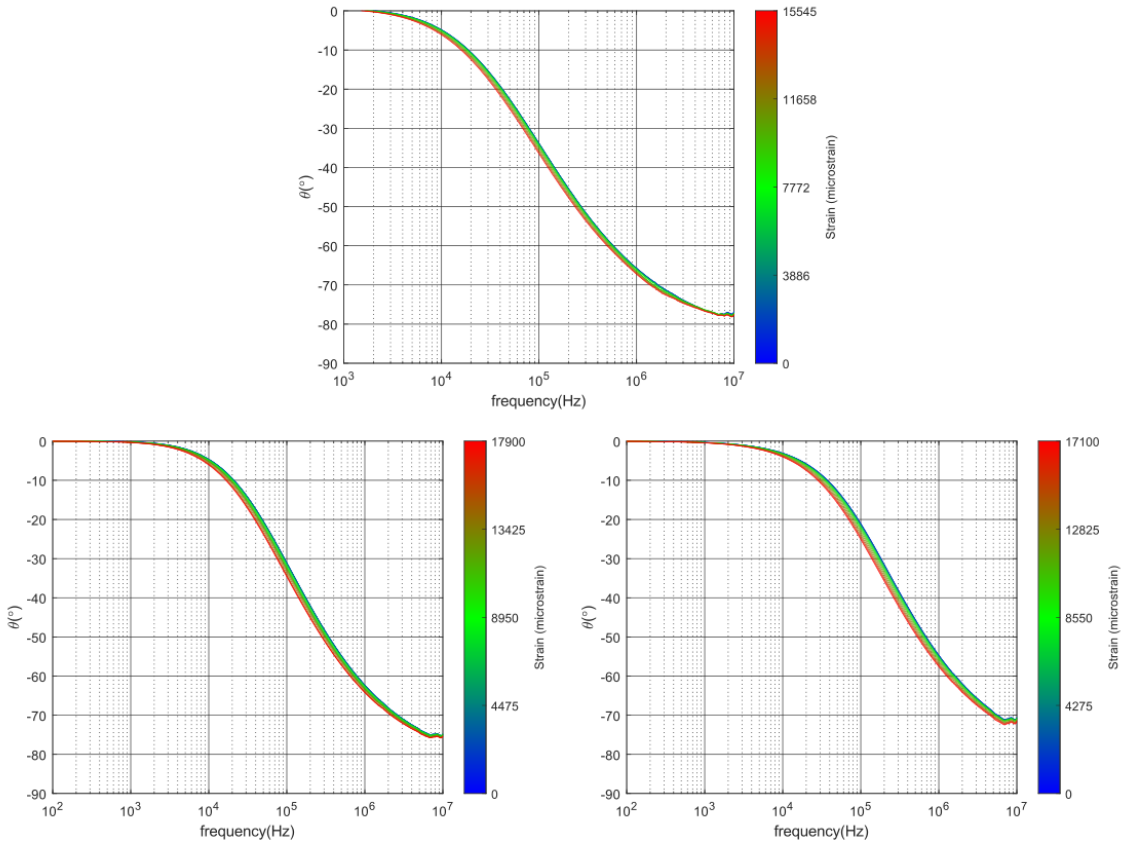

Fig. B.12. Raw phase angle data for 1.5 wt.% CNF/epoxy v-notched specimens (Top: Sample 1, Left: Sample 2, and Right: Sample 3.)

C. EFFECTIVE AC CONDUCTIVITY

This appendix provides all plots of the effective AC conductivity which are not inserted in Chapter 5. Again, the effective AC conductivity with respect to normal and shear strain are plotted. As the color moves from blue to red, the normal and shear strains increase. For the same amount of CNFs in the epoxy matrix, the effective AC conductivity have same trend and range of magnitude per test (i.e. uniaxial and v-notched rail shear test).

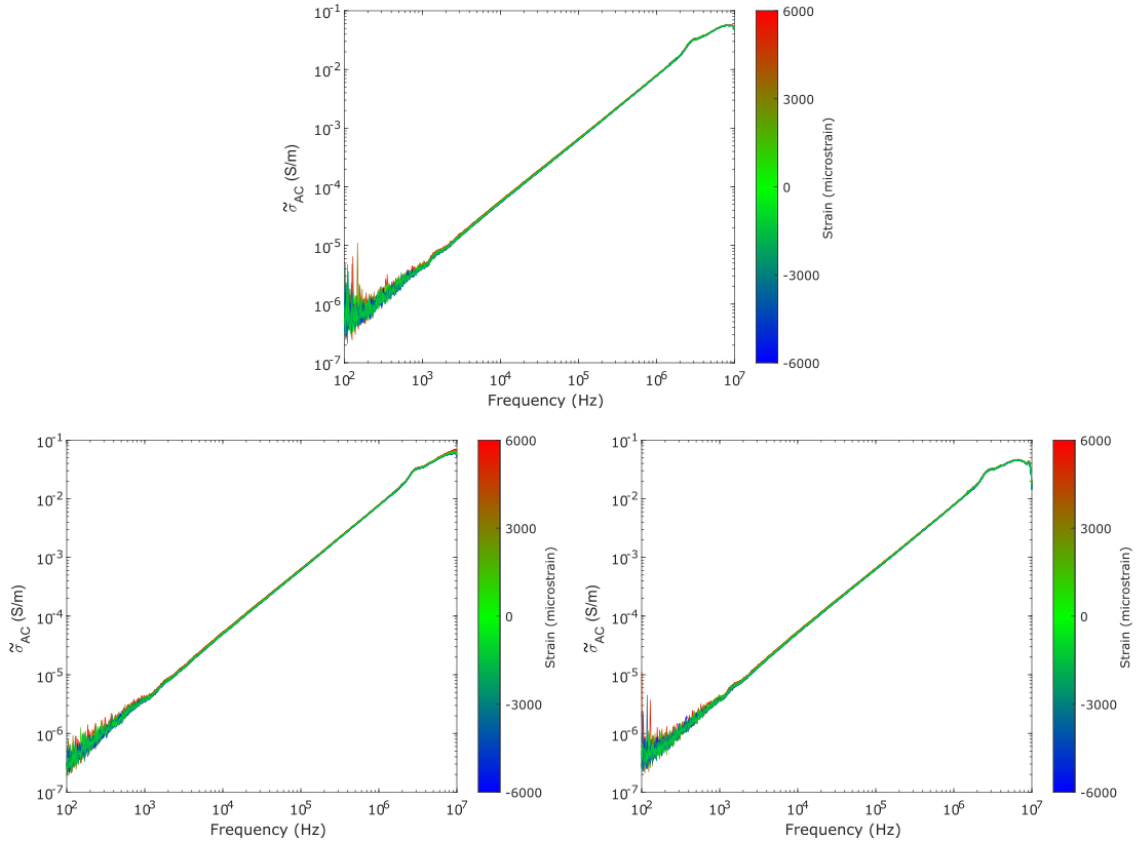

Fig. C.1. The effective AC conductivity with respect to applied axial strain for 0.5 wt.% CNF/epoxy dog-bone specimens (Top: Sample 1, Left: Sample 2, and Right: Sample 3.)

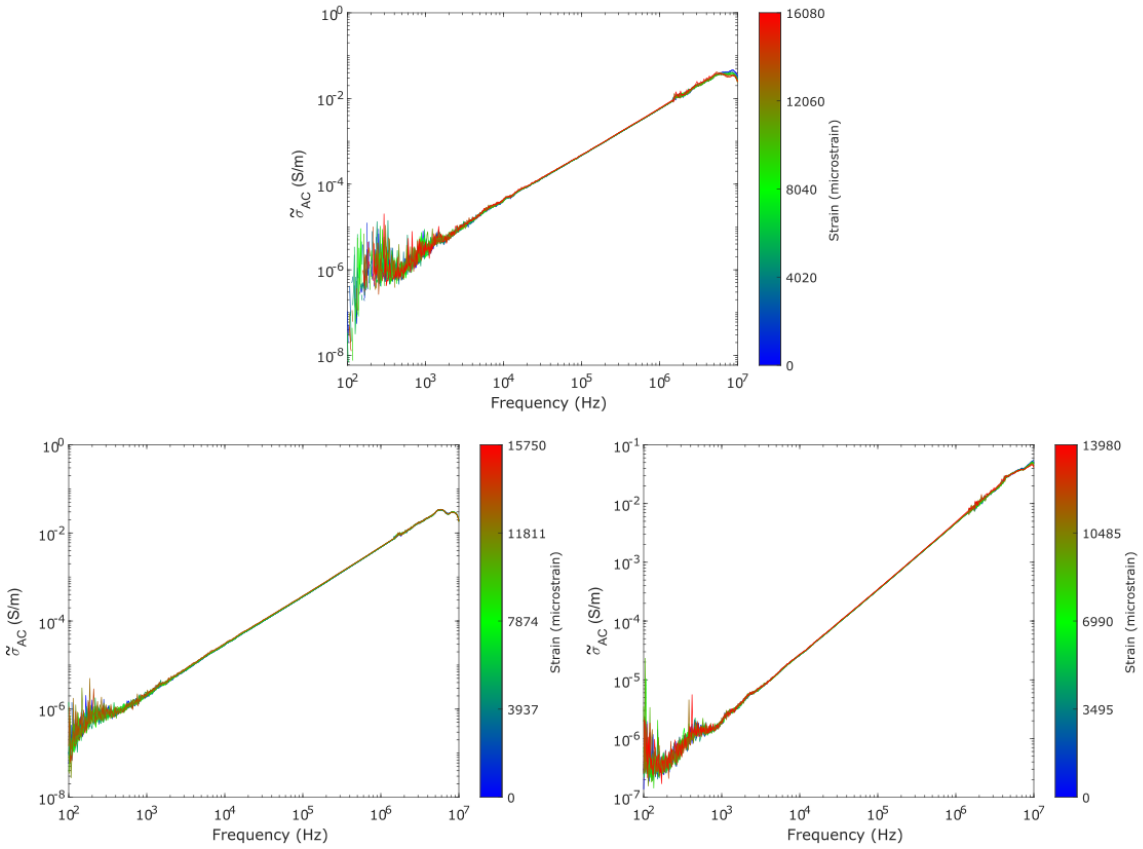

Fig. C.2. The effective AC conductivity with respect to applied shear strain for 0.5 wt.% CNF/epoxy dog-bone specimens (Top: Sample 1, Left: Sample 2, and Right: Sample 3.)

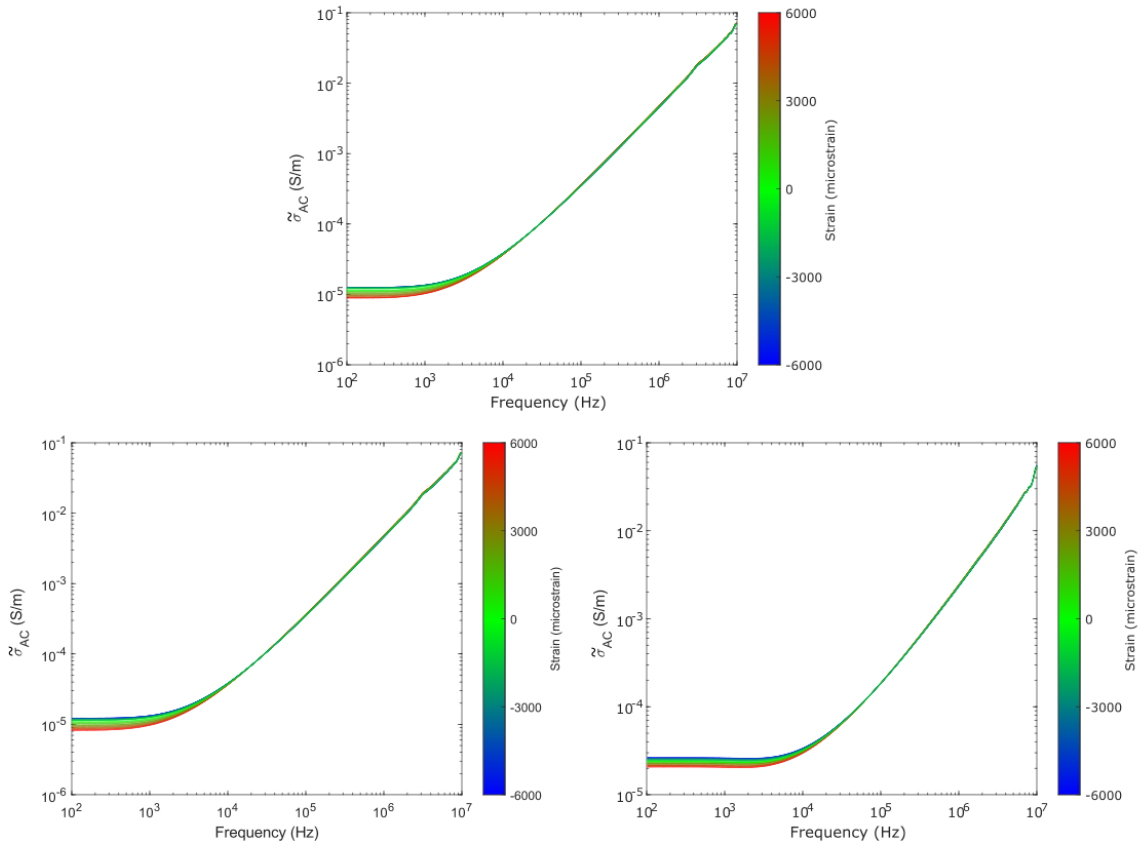

Fig. C.3. The effective AC conductivity with respect to applied axial strain for 1.0 wt.% CNF/epoxy dog-bone specimens (Top: Sample 1, Left: Sample 2, and Right: Sample 3.))

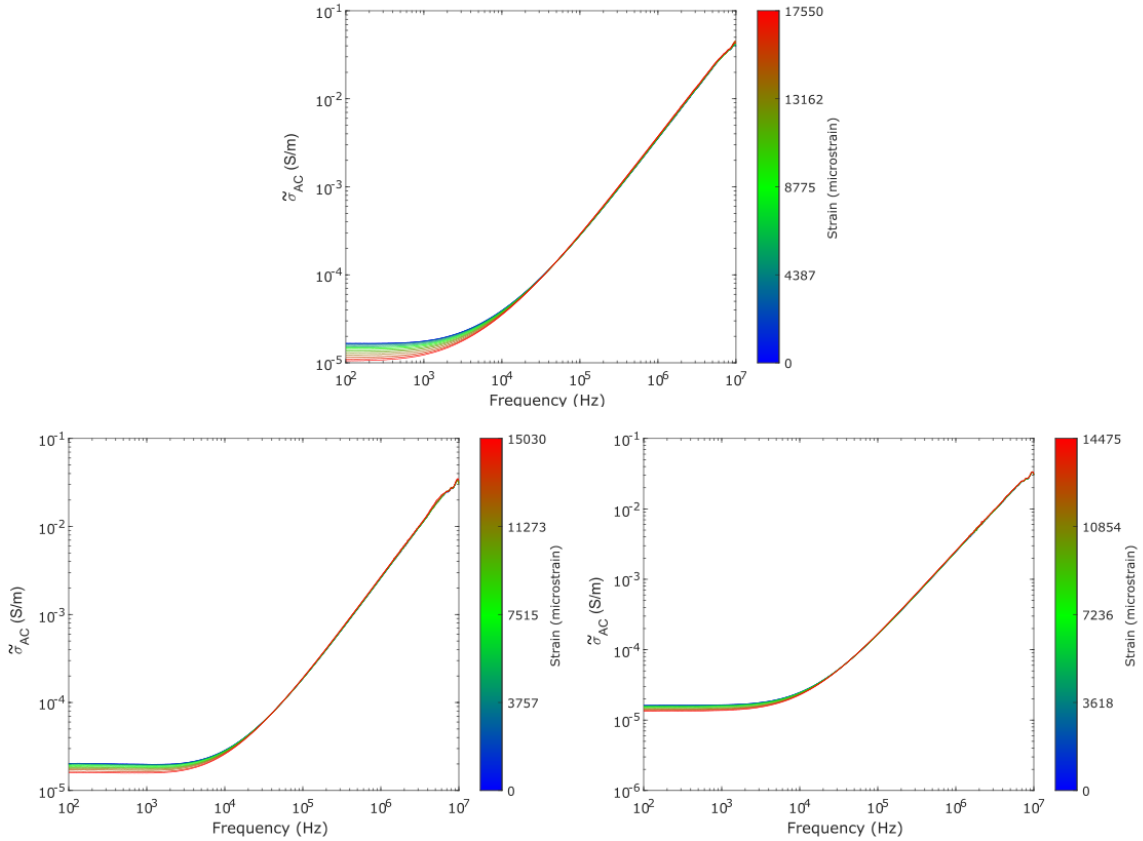

Fig. C.4. The effective AC conductivity with respect to applied shear strain for 1.0 wt.% CNF/epoxy dog-bone specimens (Top: Sample 1, Left: Sample 2, and Right: Sample 3.)

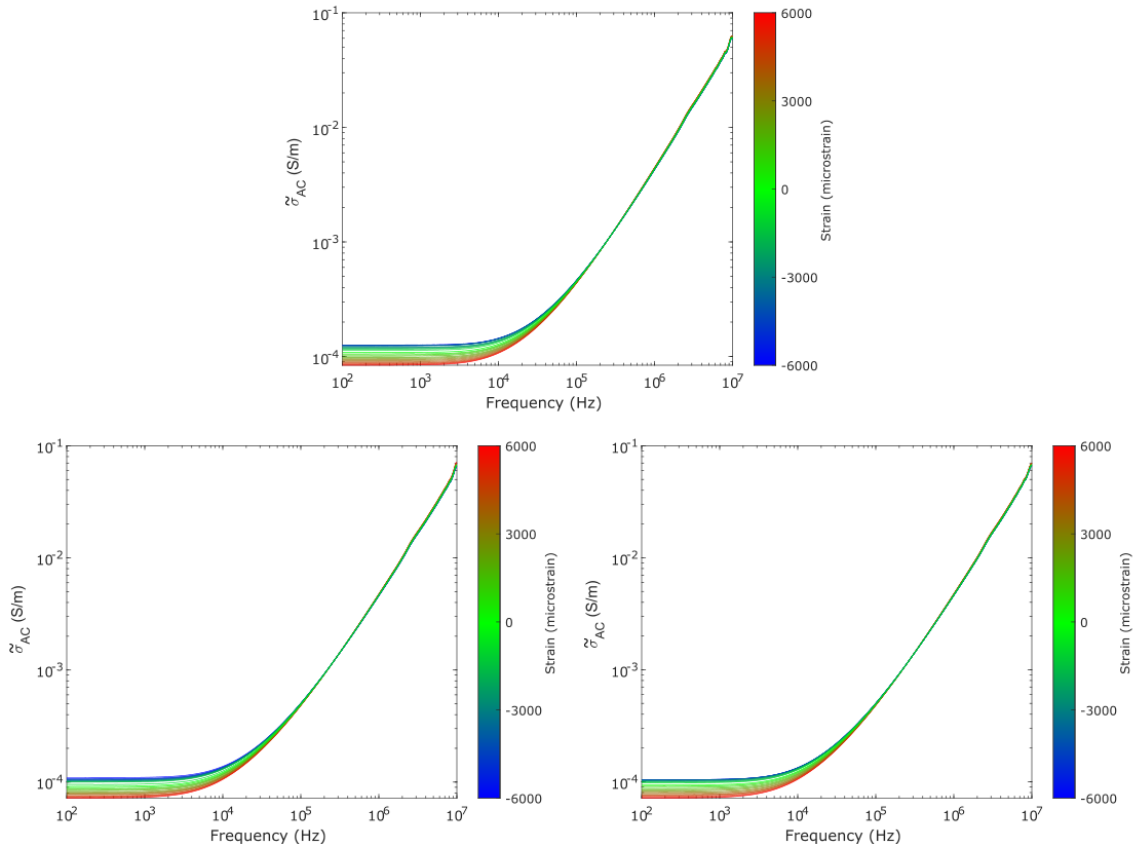

Fig. C.5. The effective AC conductivity with respect to applied axial strain for 1.5 wt.% CNF/epoxy dog-bone specimens (Top: Sample 1, Left: Sample 2, and Right: Sample 3.)

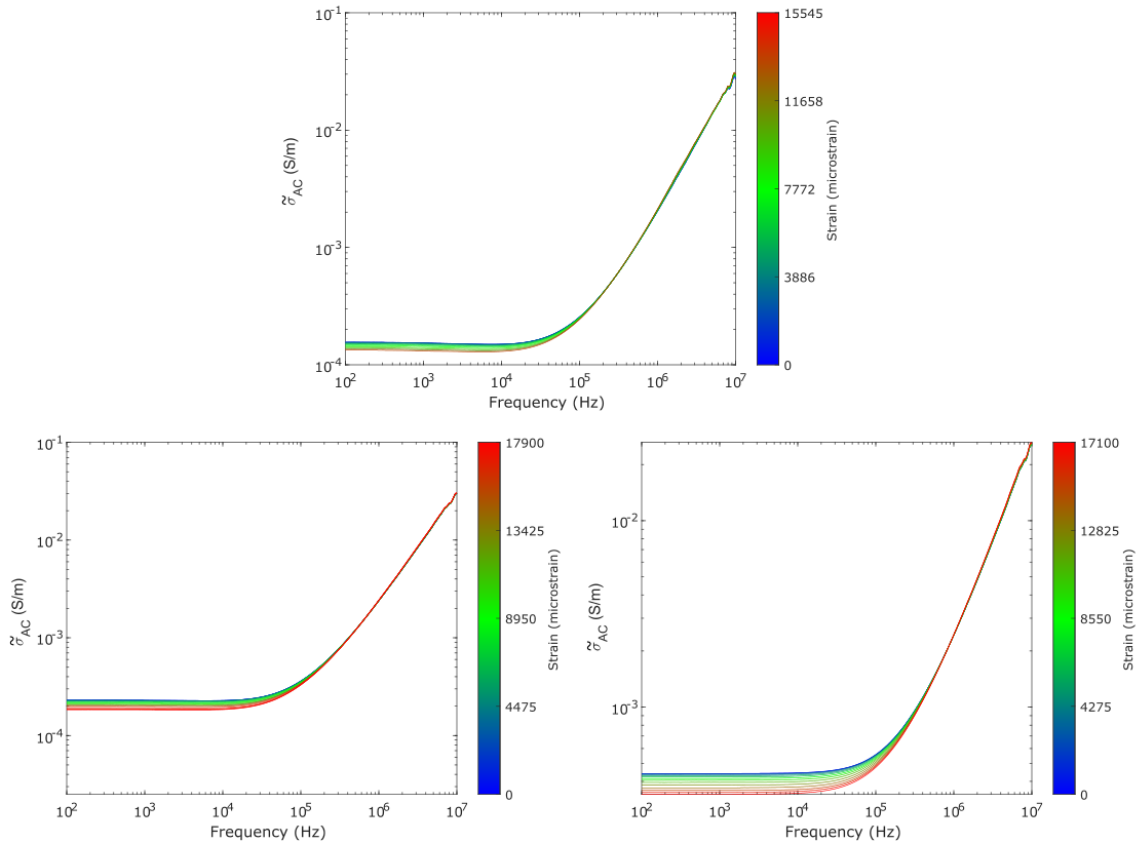

Fig. C.6. The effective AC conductivity with respect to applied shear strain for 1.5 wt.% CNF/epoxy dog-bone specimens (Top: Sample 1, Left: Sample 2, and Right: Sample 3.)

D. EIS PLOTS

This appendix provides all EIS plots which were not included in Chapter 5 due to repetition of similar plots. Again, EIS plots are presented as a function of applied normal and shear deformation. As the color goes from blue to red, the normal and shear strains again increase. Here, EIS plots per each weight fraction and test type show same trend and same magnitude range. Lastly, note that considerable noise exists for 0.5 wt.% CNF/epoxy specimens.

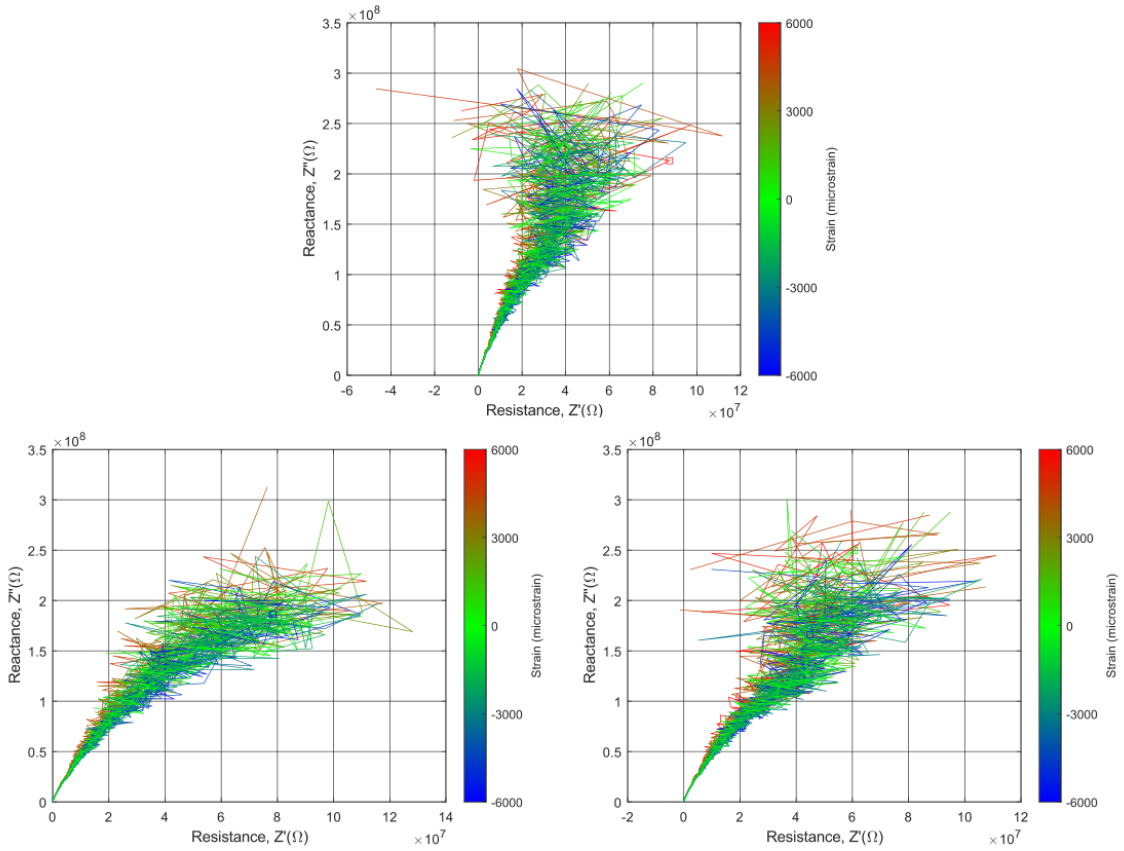

Fig. D.1. EIS data for 0.5 wt.% CNF/epoxy dog-bone specimens (Top: Sample 1, Left: Sample 2, and Right: Sample 3.)

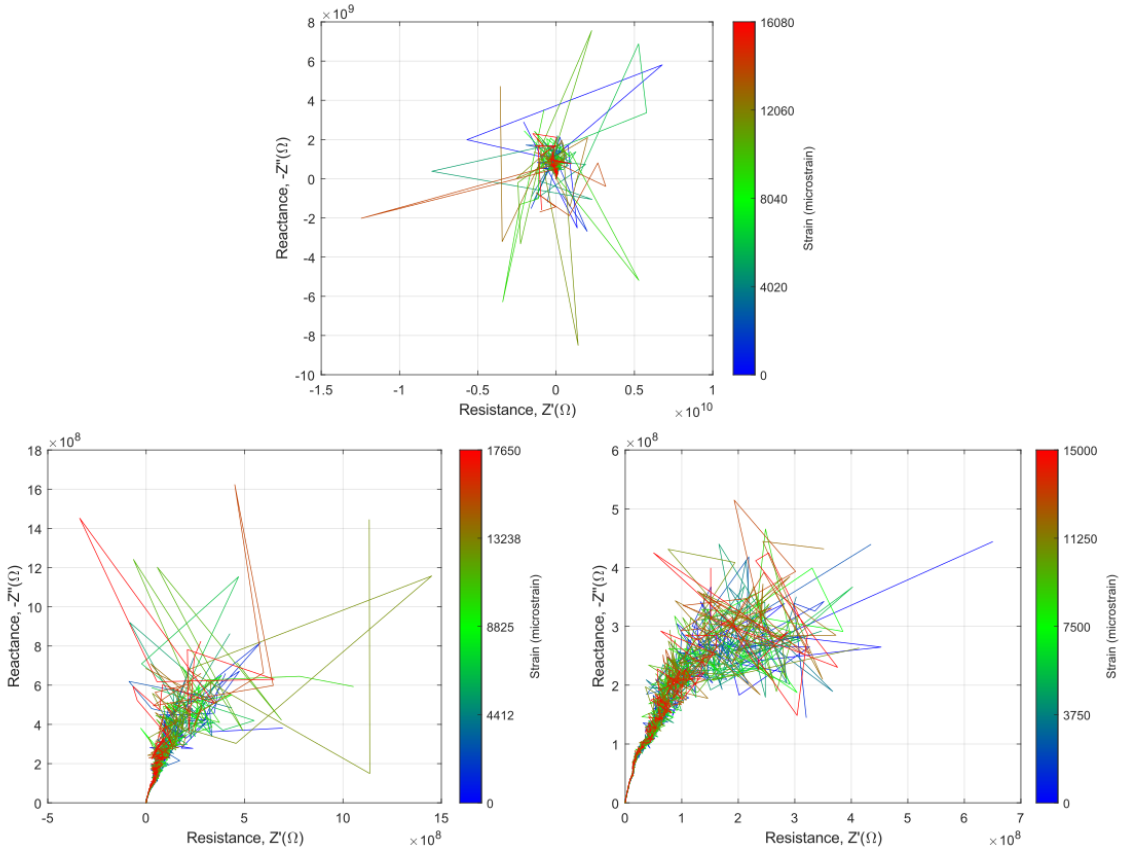

Fig. D.2. EIS data for 0.5 wt.% CNF/epoxy v-notched specimens (Top: Sample 1, Left: Sample 2, and Right: Sample 3.)

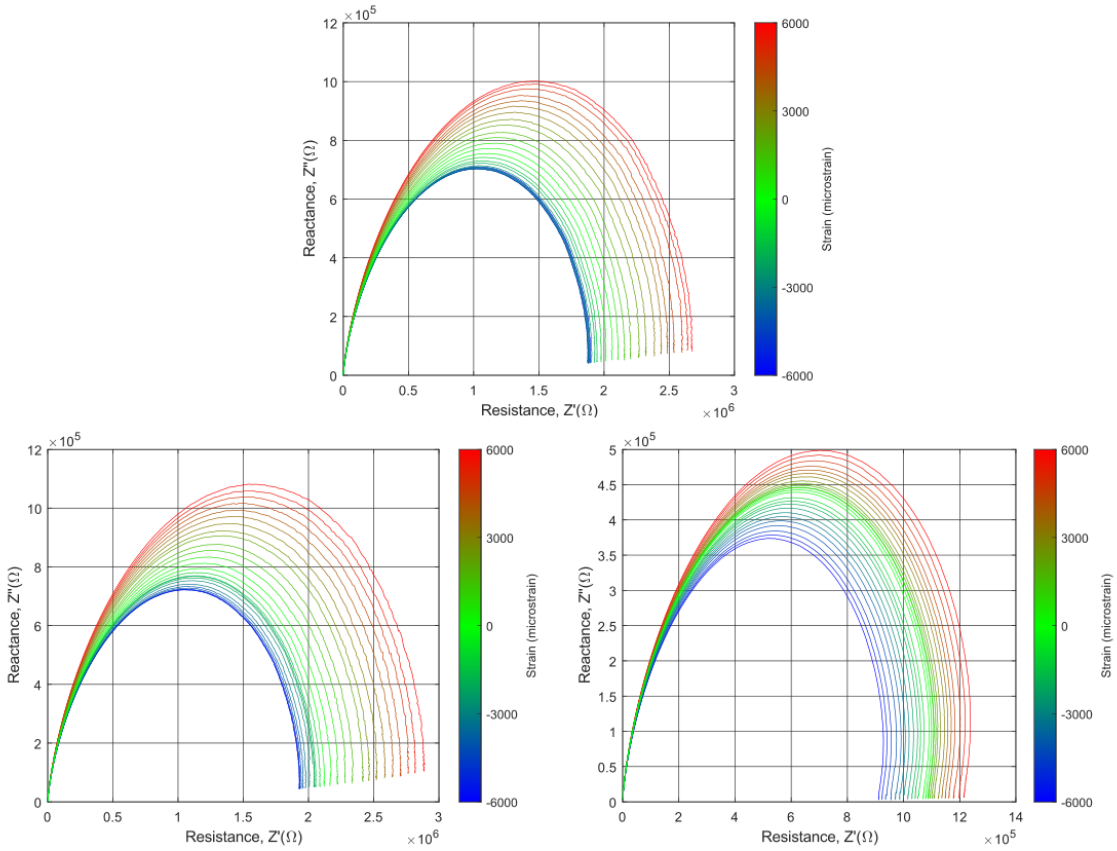

Fig. D.3. EIS data for 1.0 wt.% CNF/epoxy dog-bone specimens (Top: Sample 1, Left: Sample 2, and Right: Sample 3.)

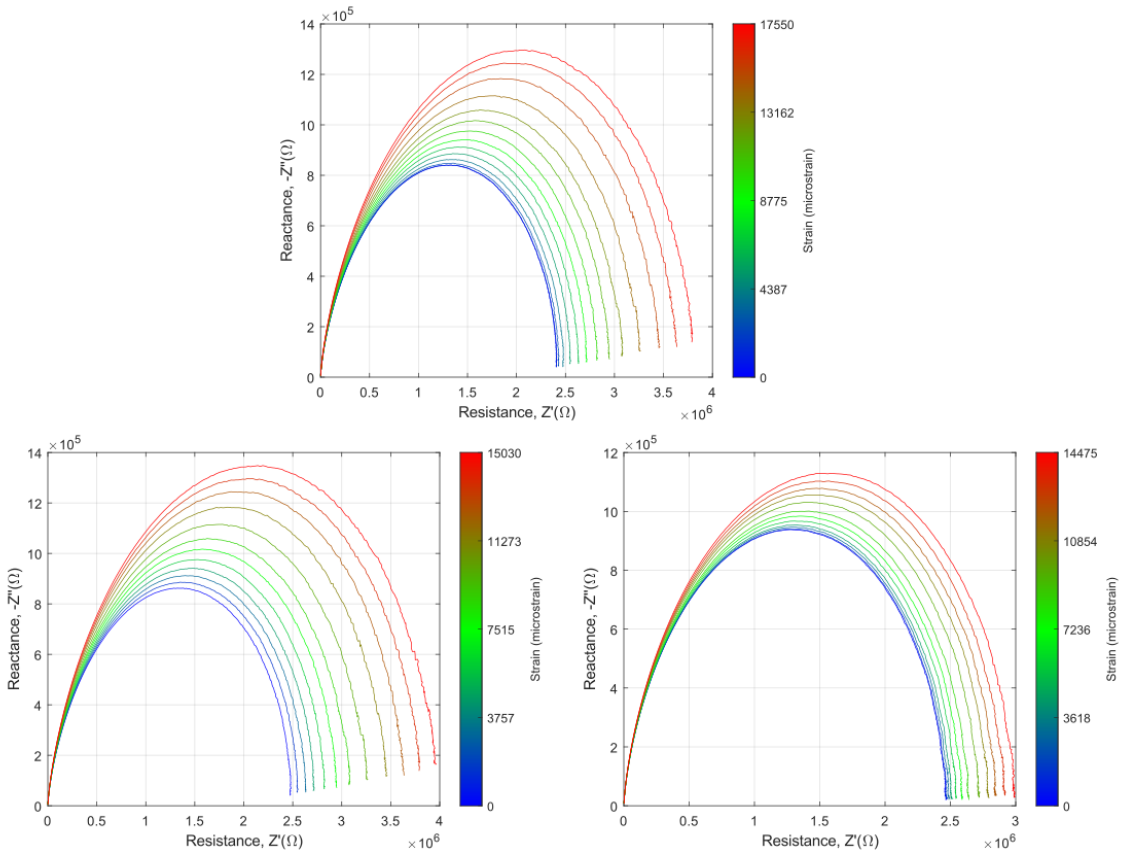

Fig. D.4. EIS data for 1.0 wt.% CNF/epoxy v-notched specimens (Top: Sample 1, Left: Sample 2, and Right: Sample 3.)

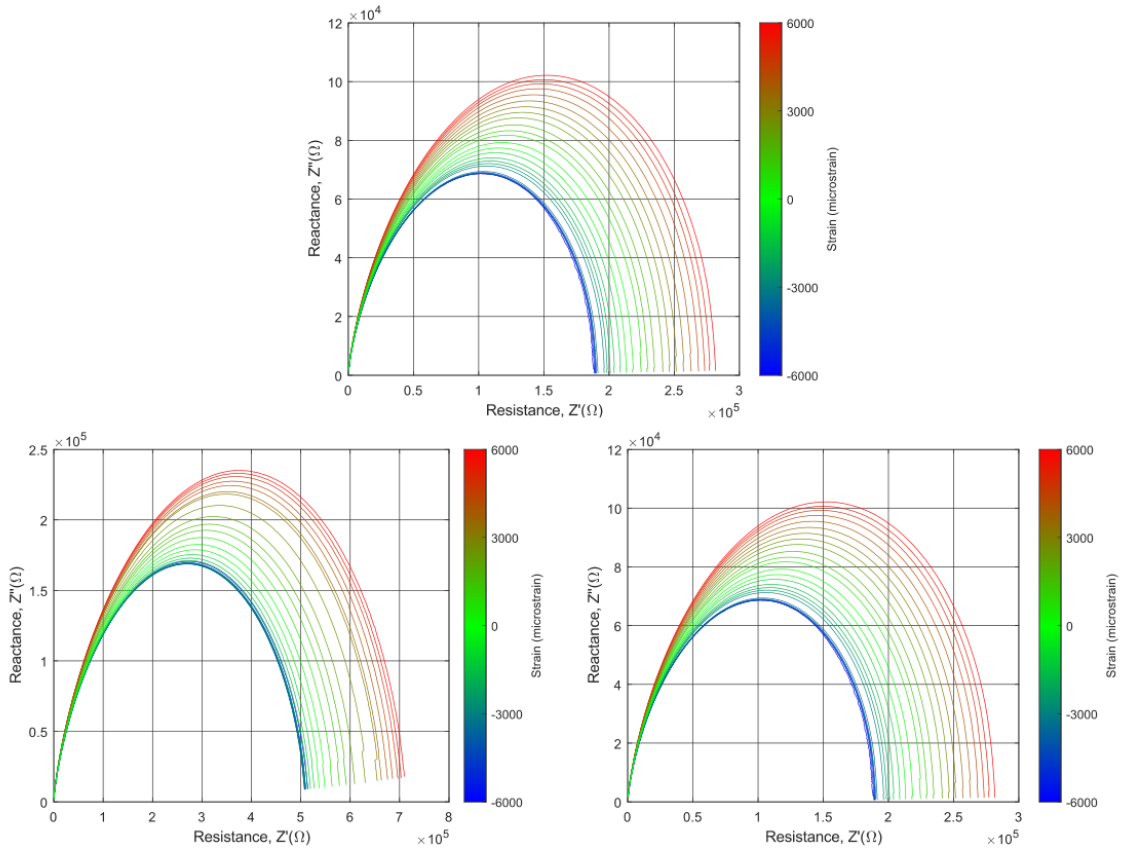

Fig. D.5. EIS data for 1.5 wt.% CNF/epoxy dog-bone specimens (Top: Sample 1, Left: Sample 2, and Right: Sample 3.)

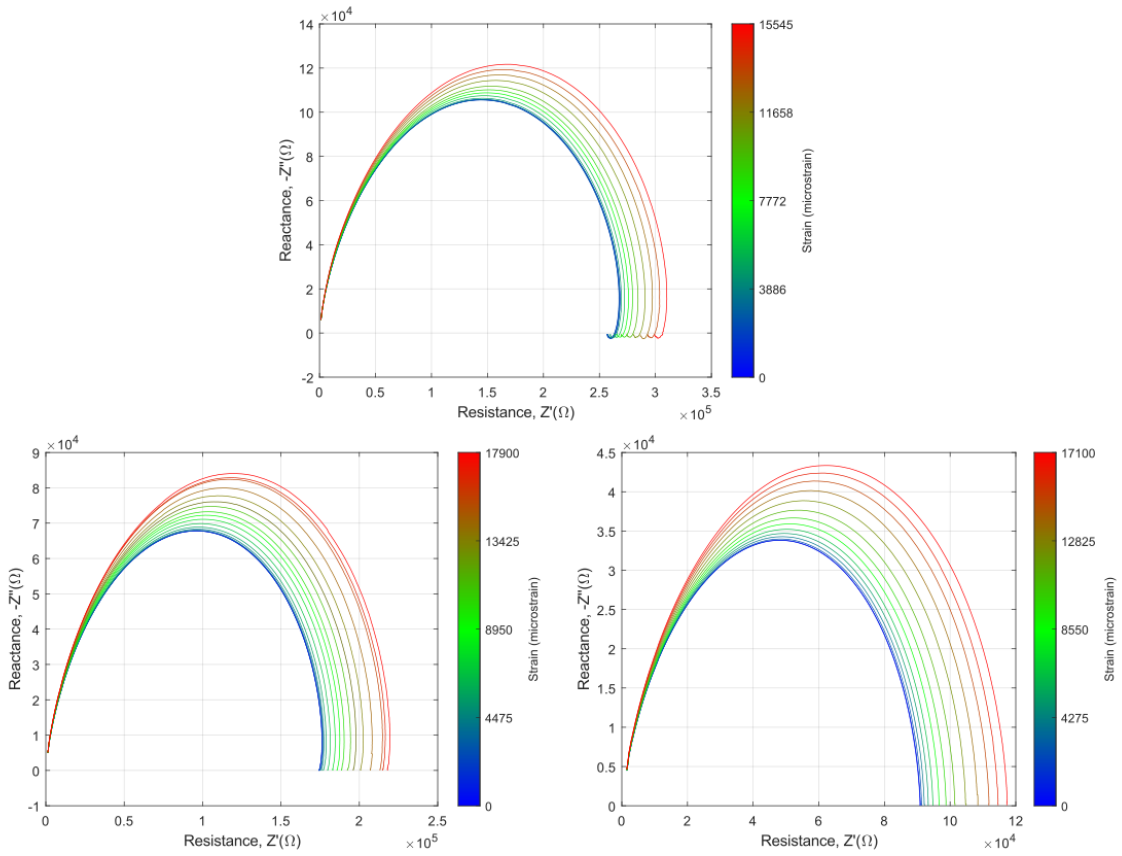

Fig. D.6. EIS data for 1.5 wt.% CNF/epoxy v-notched specimens (Top: Sample 1, Left: Sample 2, and Right: Sample 3.)

VITA

VITA

EDUCATION

- Master of Science in Aeronautics and Astronautics at Purdue University, Aug 2015 – May 2017.
- Bachelor of Science in Aerospace Engineering at University of Maryland College Park, Sep 2008 – May 2013.

ACADEMIC EMPLOYMENT

- Graduate Research Assistant, School of Aeronautics and Astronautics, Purdue University, Sep 2016 – present.
- Teaching Assistant, School of Aeronautics and Astronautics, Purdue University, Aug 2018 – May 2020.

PUBLICATIONS

- G. M. Koo and T. N. Tallman, "Frequency-Dependent Alternating Current Piezoresistive Switching Behavior in Self-Sensing Carbon Nanofiber Composites," under review by *Carbon* (2020)
- G. M. Koo and T. N. Tallman, "An Experimental Exploration of Deformation-Dependent AC Conductivity in Carbon Nanofiber-Modified Epoxy," in the proceedings of *SPIE Smart Structures/NDE* (2020)
- G. M. Koo and T. N. Tallman, "Higher-Order Resistivity-Strain Relations for Self-Sensing Nanocomposites Subject to General Deformations," *Composites Part B: Engineering*, 190, 107907 (2020)
- G. M. Koo, T. N. Tallman, "On the Development of Tensorial Deformation-Resistivity Constitutive Relations in Conductive Nanofiller-Modified Composites," in the proceedings of *ASME 2018 SMASIS* (2018)

- T. N. Tallman, S. Gungor, G. M. Koo, and C. E. Bakis, "On the Inverse Determination of Displacements, Strains, and Stresses in a Carbon Nanofiber/Polyurethane Nanocomposite from Conductivity Data Obtained via Electrical Impedance Tomography," *Journal of Intelligent Material Systems and Structures*, 28, 2617-2629 (2017) **ASME ASMS Mechanics and Materials Best Paper Award**
- K. Lee, T. Taira, G. M. Koo, J. Lee, J. Yoh, "Ignition Characteristics of Laser-Ablated Aluminum at Shock Pressures up to 2GPa," *Journal of Applied Physics*, Volume 115, Issue 1 (2014)
- K. Lee, T. Taira, G. M. Koo, J. Lee, J.S Park, J. Yoh, "Aluminum Particle Ignition Characteristics at High Pressure Condition up to 2 GPa," *Kosco Symposium* (2013)
- K. Lee, T. Taira, G. M. Koo, J. Lee, J.S Park, J. Yoh, "High Pressure Study of Aluminum Particle Ignition Using Lasers," *ICDERS* (2013)
- K. Lee, T. Taira, G. M. Koo, J. Lee, J.S Park, J. Yoh, "Aluminum Ignition in Laser-Generated Aluminum Particles in High Temperature and High Pressure Environment," *Kosco Symposium* (2012)